

# Bayesian inferencing and deterministic anisotropy for the retrieval of the molecular geometry $|\Psi(\mathbf{r})|^2$ in gas-phase diffraction experiments

Kareem Hegazy<sup>1,2,\*</sup>, Varun Makhija<sup>3</sup>, Phil Bucksbaum<sup>1,2,4</sup>, Jeff Corbett<sup>5</sup>, James Cryan<sup>2</sup>, Nick Hartmann<sup>6</sup>, Markus Ilchen<sup>2,7,8</sup>, Keith Jobe<sup>5</sup>, Renkai Li<sup>9</sup>, Igor Makasyuk<sup>5</sup>, Xiaozhe Shen<sup>5</sup>, Xijie Wang<sup>5</sup>, Stephen Weathersby<sup>5</sup>, Jie Yang<sup>9</sup>, and Ryan Coffee<sup>2,6,\*</sup>

<sup>1</sup>*Department of Physics, Stanford University, Stanford, California 94305, USA*

<sup>2</sup>*Stanford PULSE Institute, SLAC National Accelerator Laboratory, 2575 Sand Hill Road, Menlo Park, California 94025, USA*

<sup>3</sup>*Department of Chemistry and Physics, University of Mary Washington, Fredericksburg, Virginia 22401, USA*

<sup>4</sup>*Department of Applied Physics, Stanford University, Stanford, California 94305, USA*

<sup>5</sup>*SLAC National Accelerator Laboratory, 2575 Sand Hill Road, Menlo Park, California 94025, USA*

<sup>6</sup>*Linac Coherent Light Source, SLAC National Accelerator Laboratory, Menlo Park, California 94025, USA*

<sup>7</sup>*European XFEL, Holzkoppel 4, 22869 Schenefeld, Germany*

<sup>8</sup>*Universität Kassel, Heinrich-Plett-Str. 40, 34132 Kassel, Germany and*

<sup>9</sup>*Department of Engineering Physics, Tsinghua University, Beijing 100084, China*

(Dated: September 19, 2022)

Currently, our general approach to retrieve the molecular geometry from ultrafast gas-phase diffraction heavily relies on complex geometric simulations to make conclusive interpretations. In this manuscript, we develop a broadly applicable ultrafast gas-phase diffraction method that approximates the molecular frame geometry  $|\Psi(\mathbf{r}, t)|^2$  distribution using Bayesian Inferencing. This method does not require complex molecular dynamics simulation and can identify the unique molecular structure. We demonstrate this method's viability by retrieving the ground state geometry distribution  $|\Psi(\mathbf{r})|^2$  for both simulated stretched NO<sub>2</sub> and measured ground state N<sub>2</sub>O. Due to our statistical interpretation, we retrieve a coordinate-space resolution on the order of 100 fm, depending on signal quality, an improvement of order 100 compared to commonly used Fourier transform based methods. By directly measuring the width of  $|\Psi(\mathbf{r})|^2$ , we open ultrafast gas-phase diffraction capabilities to measurements beyond current analysis approaches since this width is generally only accessible through simulation. Our method also leverages deterministic ensemble anisotropy; this provides an explicit dependence on the molecular frame angles. This method's ability to retrieve the unique molecular structure with high resolution, and without complex simulations, provides the potential to effectively turn gas-phase ultrafast diffraction into a discovery-oriented technique, one that probes systems that are prohibitively difficult to simulate.

## I. INTRODUCTION

Ultrafast molecular gas-phase diffraction [1–6] is a vital tool for retrieving time dependent molecular structure. We aim to expand this tool to perform high precision reconstructions of molecular geometry  $|\Psi(\mathbf{r}, t)|^2$ , where  $\mathbf{r}$  is the molecular frame nuclear coordinates, without relying on molecular dynamics simulations. Since elastic diffraction is a many-to-one process, directly inverting diffraction patterns for the molecular geometry is intractable. Typically, we require complex excited state simulations to provide the molecular geometries which we then validate through comparisons with measured diffraction patterns or pair-distribution functions (PDFs – a weighted histogram of pair-wise distances). Consequently, ultrafast gas-phase diffraction is generally constrained by the limitations of complex excited state simulations.

A variety of studies sought to reduce reliance on complex simulations. Fourier transforming the time dependence exposes dissociative and vibronic signals [7–9] but it is insensitive to classes of isomerizations. Methods employing ensemble anisotropy have garnered much interest [10–18] yet they struggle to get sub-Angstrom resolution for generic molecular structures. Optimization methods, while capable of exposing large-scale motion, are sus-

ceptible to local minima [17]. Pattern matching measured data against sampled isomers [19–21] becomes intractable for moderately large geometries due to the curse of dimensionality. For example, a molecule with  $N_{\text{atoms}}$  atoms has  $3N_{\text{atoms}} - 6$  degrees of freedom. To independently sample each degree of freedom 10 times would require  $10^{3N_{\text{atoms}} - 6}$  geometries, becoming intractable for molecules with 7 or more atoms. Simulations reduce the geometry-space of isomers to select, but this trade-off requires previous knowledge [19] that potentially imparts biases.

We employ insights from molecular ensemble anisotropy methods, applied statistics, and machine learning principles to approximate the molecular geometry probability density ( $|\Psi(\mathbf{r}, t)|^2$ ). We access the molecular frame by decomposing measured data onto anisotropic components. Then, we iteratively approximate  $|\Psi(\mathbf{r}, t)|^2$  with a statistical approach uniquely suited for high repetition-rate diffraction facilities where the resolution strongly improves with signal to noise much faster than increasing the  $q$  range beyond moderate values. Unlike the PDF approach, it retrieves the molecular distances and angles required to define a unique molecular geometry. An important new feature of our method is its ability to quantitatively measure

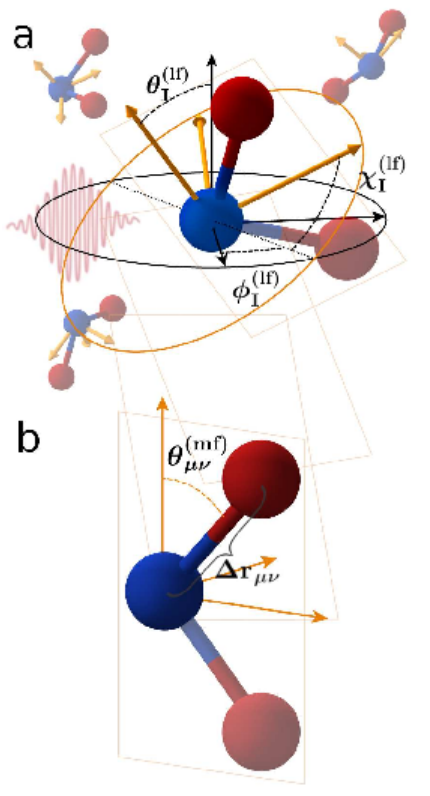


FIG. 1. Ensemble anisotropy reveals the pair-wise angles ( $\theta_{\mu\nu}^{(mf)}$  and  $\phi_{\mu\nu}^{(mf)}$ ) and is measured with respect to the lab frame Euler angles  $\theta_I^{(lf)}$ ,  $\phi_I^{(lf)}$ , and  $\chi_I^{(lf)}$ . We illustrate the correspondence between the lab frame (a) and molecular frame (b) for a single pair-wise distance (the highlighted NO bond). The origin is defined by the nitrogen atom. The lab frame is defined by the laser polarization and propagation direction, while the molecular frame is defined by the molecule's ground state principal moments of inertia.

additional parameters, such as the width of  $|\Psi(\mathbf{r}, t)|^2$ . We report order 100 fm resolution without complex excited state molecular dynamics simulations and require only the ground state geometry and its transition dipole moment. This method has the potential to expand ultrafast gas-phase diffraction into a discovery oriented technique, one that is free of complex excited state simulation limitations and is applicable to novel molecular systems.

Time dependent ensemble anisotropy accesses the molecular frame through angular constraints [22–28]. We define anisotropy with the Euler angles  $\theta_I^{(lf)}$  (polar),  $\phi_I^{(lf)}$  (azimuthal), and  $\chi_I^{(lf)}$  between the lab frame and the molecular frame (Fig. 1a). An induced rotational wavepacket creates ensemble anisotropy given by  $|\Psi(\theta^{(lf)}, \phi^{(lf)}, t)|^2$ . Axis Distribution Moments (ADMs) [24, 29, 30] are the coefficients in the Wigner D matrix

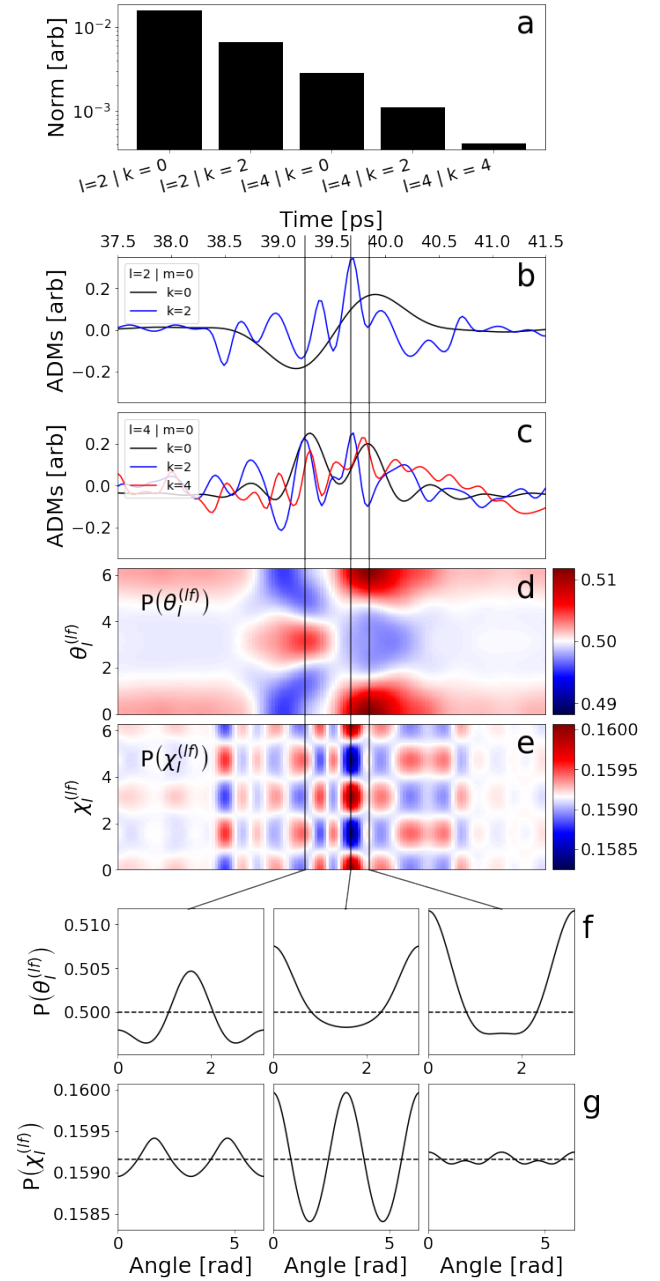


FIG. 2. The Axis Distribution Moments (ADMs) encapsulate the ensemble anisotropy which provides various constraints on the molecular frame as a function of time. Panel a shows the square norms of the ADMs, while panels b and c show their time dependence. Panels d and e show the time dependent ensemble anisotropy probability distribution for  $\theta_I^{(lf)}$  and  $\chi_I^{(lf)}$ , respectively. Panels f and g show illustrative line-outs of these Euler angle distributions for  $\theta_I^{(lf)}$  and  $\chi_I^{(lf)}$ , respectively, with isotropy indicated by the dashed lines.

expansion of  $|\Psi(\theta^{(lf)}, \phi^{(lf)}, t)|^2$

$$\mathcal{A}_{mk}^l(t) = \frac{2l+1}{8\pi^2} \left\langle \Psi(t) \left| D_{mk}^l \left( \phi_I^{(lf)}, \theta_I^{(lf)}, \chi_I^{(lf)} \right) \right| \Psi(t) \right\rangle. \quad (1)$$

These ADMs describe the ensemble of molecular frame orientations with respect to the lab frame. When calculating the ADMs the  $l$ ,  $m$ , and  $k$  are difference and sum of quantum numbers between rotational eigenstates, respectively for the total angular momentum, the projection onto the lab frame  $z$  axis, and the projection onto the molecular frame  $z$  axis. The ADMs access the molecular frame by decomposing the measurement into  $C_{lmk}(q)$  coefficients, dependent on pair-wise distances and angles ( $\theta_{\mu\nu}^{(mf)}$  and  $\phi_{\mu\nu}^{(mf)}$ ) shown in Fig. 1b. The PDF is not directly sensitive to these angles. Figure 2 illustrates how transient anisotropy (panels b and c) provides constraints on these Euler angles and consequently the molecular frame (panels d-g). For example, at 39.25 ps the anisotropy provides simultaneous constraints on  $\theta_1^{(lf)}$  and  $\chi_1^{(lf)}$ . At 39.68 ps,  $\chi_1^{(lf)}$  (the molecular frame azimuthal plane) is highly constrained. At 39.85 ps the ensemble is well localized in  $\theta_1^{(lf)}$ , resolving measurements along the molecular frame  $\hat{z}$ . Here,  $P(\phi_1^{(lf)})$  is uniform due to cylindrical symmetry imparted by a linearly polarized pulse.

To approximate  $|\Psi(\mathbf{r}, t)|^2$ , we use Bayesian Inferencing with markov-chain monte carlo (MCMC) techniques to tackle the curse of dimensionality. Bayesian Inferencing describes a class of statistical inferencing techniques using Bayes's Theorem to update one's model based on observed data [31], allowing us to ultimately approximate  $|\Psi(\mathbf{r}, t)|^2$  as the probability distribution  $P(\mathbf{r}, t | \Theta, C)$ . The  $P(\mathbf{r}, t | \Theta, C)$  distribution is parameterized by  $\Theta$ , which includes the molecular geometry degrees of freedom and is retrieved using MCMC techniques. This Bayesian Inferencing and MCMC approach efficiently samples pertinent geometries consistent with the measured  $C_{lmk}(q)$  in an unbiased fashion. It naturally avoids regions in our sampling space that are inconsistent with the  $C_{lmk}(q)$ . Importantly, since  $P(\mathbf{r}, t | \Theta, C)$  is conditioned on the measured  $C_{lmk}(q)$  coefficients and we analytically relate molecular frame pair-wise distances and angles to the  $C_{lmk}(q)$ , we actually retrieve  $P(\mathbf{r}, t | \Theta, C)$  with neither the PDF nor complex molecular dynamics simulations.

In this manuscript, we validate these principles by retrieving  $|\Psi(\mathbf{r})|^2$  for the ground states of both simulated  $\text{NO}_2$  and measured  $\text{N}_2\text{O}$ . Here  $\text{NO}_2$ , an asymmetric top, serves as a test case to show our method's broad capabilities and behavior under various experimental conditions, while the  $\text{N}_2\text{O}$  experiment validates such capabilities on measured results. We chose these molecules to be amenable to conventional methods to benchmark. We discuss how  $P(\mathbf{r} | \Theta, C)$  improves upon the Fourier limited PDF resolution by a factor of 100, and how this procedure depends more strongly on signal to noise than

the measured  $q$  range beyond modest thresholds.

## II. METHOD

Our method can be subdivided into three principal concepts. Firstly, we use ensemble anisotropy, described by the ADMs, to access the molecular frame by projecting the data onto anisotropic components. Secondly, we select a model,  $P(\mathbf{r} | \Theta, C)$ , to approximate  $|\Psi(\mathbf{r})|^2$  and develop our statistical approach to solve for  $\Theta$  using Bayesian Inferencing. Lastly, we take our statistical description and use MCMC techniques to solve for  $P(\Theta | C)$  to retrieve the optimal  $\Theta$  parameters ( $\Theta^*$ ). The code used for this analysis can be found in Ref. [32], which can be run to reproduce the following results or adapted for other molecules.

### A. Extracting Molecular Frame Information

We describe our analysis procedure for a system given an induced deterministic ensemble anisotropy under experimental conditions at the SLAC MeV Ultrafast Electron Diffraction facility (UED) [4]. Our generic pump-probe setup is similar to most ultrafast diffraction setups, consisting of an 800 nm Ti:Sapphire pump laser and a 120 fs FWHM electron bunch probe. For the simulated  $\text{NO}_2$  results, we consider using a single 10 TW/cm<sup>2</sup> 800 nm pump pulse to impulsively induce a coherent rotational wave packet and probing it within a window of high anisotropy variation: [37.5, 41.5] ps. For the measured  $\text{N}_2\text{O}$  sample, a train of 8 identical 800 nm pulses (40 fs duration and  $5 \times 10^{12}$  W/cm<sup>2</sup> irradiance) separated by full quantum revivals induced such rotational wavepacket. We measured the first field free full quantum revival over a window of  $\sim 3$  ps. We masked  $q$  regions [0, 3.5]  $\text{\AA}^{-1}$  and above 7.25  $\text{\AA}^{-1}$  due to ellipticity in the imaging of the diffraction pattern and poor signal to noise, respectively. Linearly polarized pump pulses induce azimuthal symmetry, which sets  $m = 0$  in Eq. 1 ( $P(\phi_1^{(lf)}, t) = 1/2\pi$ ), while the Raman excitation of the wavepacket requires  $l$  being even in Eq. 1.

We define anisotropy in two equivalent ways and quantify it through the ADMs. Firstly, anisotropy is defined by a non-zero projection of the measured diffraction pattern onto any  $Y_l^m$  with even  $l > 0$  for a given  $\Delta q$  range. Secondly, anisotropy exists when there is a non-zero  $\mathcal{A}_{mk}^l(t)$  for  $l > 0$ . We note other methodologies in Refs. [29, 30, 33]. Supplementary Section VIII describes our calculation of the ADMs.

We access the molecular pair-wise distances and angles in the molecular frame. Using the ADMs and the Independent Atom Approximation, we relate measured lab frame anisotropy in diffraction patterns,  $\langle I(\mathbf{q}) \rangle(t)$ , to the molecular geometry

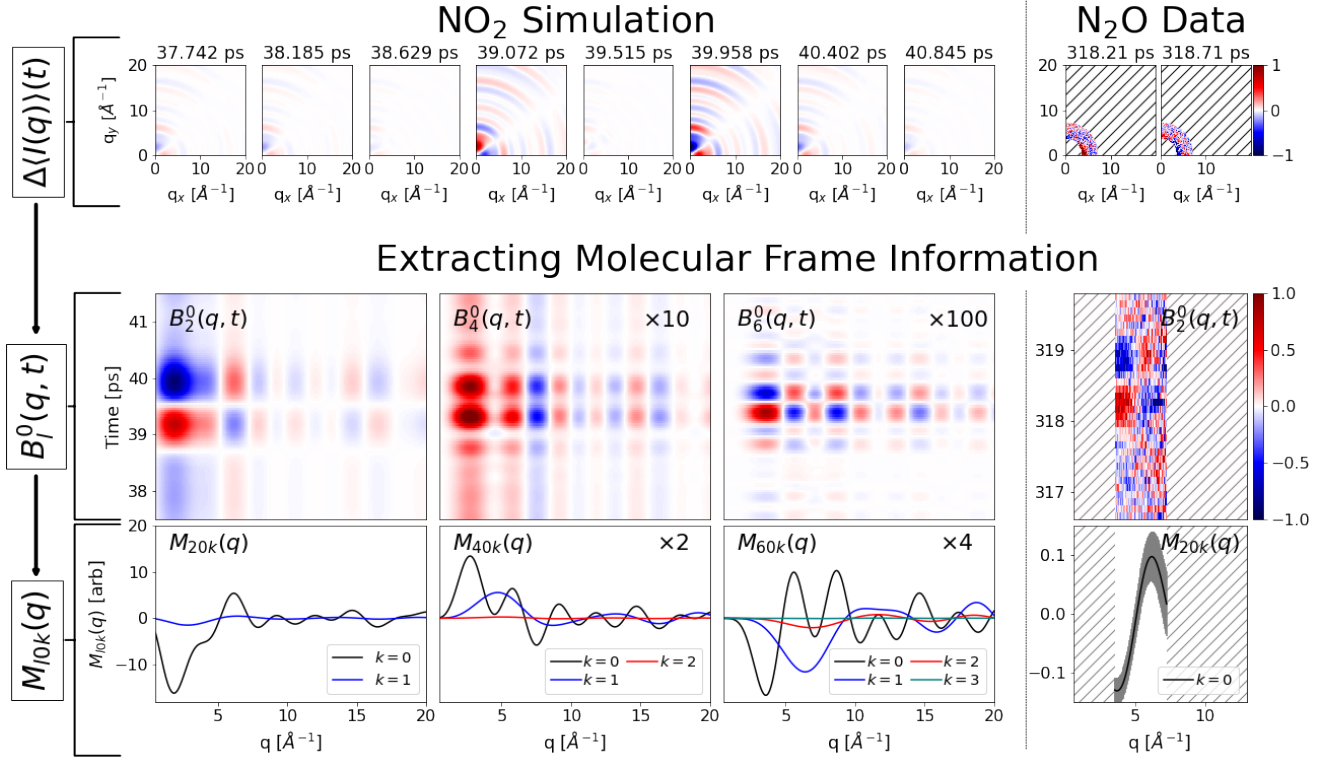


FIG. 3. To access the molecular geometry term, in the molecular frame, one must remove the lab frame anisotropy dependence and fit onto the ADMs. For the  $\text{NO}_2$  simulation (left) and  $\text{N}_2\text{O}$  data (right), we illustrate the analysis steps. One first measures  $\Delta\langle I(\mathbf{q})\rangle(t)$ , the difference diffraction pattern, given by Eq. 3 (top row). Removing the detector angular dependence, one retrieves  $B_l^m(q, t)$  of Eq. 4 (middle row). Which in turn yields  $M_{lmk}(q)$  coefficients Eq. 5 (bottom row) after removing the time dependent ensemble anisotropy (ADM). All as described in the text. We note that in the  $\text{N}_2\text{O}$  data (right) we have limited visibility of data due to experimental limitations illustrated by the hashes.

$$\begin{aligned}
 \langle I(\mathbf{q})\rangle(t) = & \mathcal{I} \left( \sum_{\mu} |f_{\mu}^*(q)|^2 + \sum_{\mu, \nu: \mu \neq \nu} \text{Re} \left\{ f_{\mu}(q) f_{\nu}^*(q) \sum_l i^l 8\pi^2 \sqrt{4\pi(2l+1)} \right. \right. \\
 & \times \sum_{m, k} (-1)^{k-m} Y_l^{-m} \left( \theta_q^{(\text{lf})}, \phi_q^{(\text{lf})} \right) \langle \Psi(t) | D_{mk}^l \left( \theta_{\text{I}}^{(\text{lf})}, \theta_{\text{I}}^{(\text{lf})}, \chi_{\text{I}}^{(\text{lf})} \right) j_l(q\Delta r_{\mu\nu}) Y_l^{-k} \left( \theta_{\mu\nu}^{(\text{mf})}, \phi_{\mu\nu}^{(\text{mf})} \right) | \Psi(t) \rangle \left. \right\} \Bigg). \quad (2)
 \end{aligned}$$

Lab Frame
Ensemble Anisotropy
Molecular Frame Geometry

In Eq. 2, derived in Supplementary Section IX,  $f_{\mu}(q)$  is the scattering amplitude of the  $\mu^{\text{th}}$  atom,  $j_l(qr)$  are the spherical Bessel functions of the first kind, and the momentum transfer vector is given by  $\mathbf{q} = [q, \theta_q^{(\text{lf})}, \phi_q^{(\text{lf})}]$ . The difference vector  $\Delta\mathbf{r}_{\mu\nu} = \mathbf{r}_{\mu} - \mathbf{r}_{\nu} = [\Delta r_{\mu\nu}, \theta_{\mu\nu}^{(\text{mf})}, \phi_{\mu\nu}^{(\text{mf})}]$  are the molecular frame pair-wise distances and angles between the  $\mu^{\text{th}}$  and  $\nu^{\text{th}}$  atoms. Figure 1b illustrates the molecular frame pair-wise distances and angles. This equation concisely shows how the ensemble anisotropy connects the lab frame to the molecular frame geometry. We note that directly accessing the molecular frame pair-wise angles  $(\theta_{\mu\nu}^{(\text{mf})}, \phi_{\mu\nu}^{(\text{mf})})$  requires anisotropy and is otherwise inaccessible through the PDF and isotropic contributions alone. This is evident by isolating the isotropic component ( $l = 0, m = 0, k = 0$ )

which sets  $Y_0^0(\theta_{\mu\nu}^{(\text{mf})}, \phi_{\mu\nu}^{(\text{mf})}) = 1/(2\sqrt{\pi})$ .

For our method, we describe optimal representations of the lab and molecular frames used in Eq. 2. The molecular frame is defined by the molecule's principal moments of inertia before laser excitation with the  $\hat{\mathbf{z}}^{(\text{mf})}$ ,  $\hat{\mathbf{x}}^{(\text{mf})}$ , and  $\hat{\mathbf{y}}^{(\text{mf})}$  corresponding to the principle moments of inertia in decreasing order: A, B, and C respectively. When looking at the  $\Delta\mathbf{r}_{\mu\nu}$  contribution, we isolate the  $\mu^{\text{th}}$  and  $\nu^{\text{th}}$  atoms while ignoring other atoms and translate the atom pair such that  $\mathbf{r}_{\nu}$  defines the origin. This is highlighted in Fig. 1b where the nitrogen is translated to the origin. This translation allows us to define the pair-wise angles and derive Eq. 2. Since we are concerned with a difference in locations  $\Delta\mathbf{r}_{\mu\nu}$ , Eq. 2 is invariant under such molecular frame translations. In the lab frame, the laser

polarization defines  $\hat{\mathbf{z}}^{(\text{lf})}$  and the propagation direction of the probe pulse defines  $\hat{\mathbf{y}}^{(\text{lf})}$ . The measured signals in the lab frame, on a 2D detector, are defined by detector parameters  $q = |\mathbf{q}|$  and the azimuthal angle  $\theta^{(\text{d})}$  defined by  $\hat{\mathbf{z}}^{(\text{lf})}$ . Supplementary Section IX describes how to rewrite  $\mathbf{q}$  in terms of the detector coordinates, in particular for small angle scattering at UED  $\theta_q^{(\text{lf})} \approx \theta^{(\text{d})}$  and  $\phi_q^{(\text{lf})} \approx 0$  as will be used below.

The primary difficulty of working with Eq. 2 comes from the expectation value including both the ensemble anisotropy and molecular frame geometry. We want to separate the ensemble anisotropy into the ADMs. This

isolates the time dependent molecular geometry term that we would like to retrieve. By doing this, we only require more tractable molecular rotation simulations with respect to the known ground state geometry in order to retrieve the time dependent molecular geometry. Otherwise, as Eq. 2 is written, it requires *a priori* knowledge of exactly the unknown time dependent geometries for which we are solving. In this work, we describe various ways to do this under common experimental conditions.

Focusing on the ground state of  $\text{NO}_2$ , we can separate the ADMs and molecular geometry contribution in Eq. 2 by applying a rigid rotor approximation:

$$\begin{aligned} \langle I(\mathbf{q}) \rangle_{\text{rigid}}(t) = & \mathcal{I} \left( \sum_{\mu} |f_{\mu}(q)|^2 + \sum_{\mu, \nu: \mu \neq \nu} \text{Re} \left\{ f_{\mu}(q) f_{\nu}^*(q) \sum_l i^l 8\pi^2 \sqrt{\frac{4\pi}{(2l+1)}} \right. \right. \\ & \times \sum_{m,k} (-1)^{k-m} \underbrace{Y_l^{-m} \left( \theta_q^{(\text{lf})}, \phi_q^{(\text{lf})} \right)}_{\text{Lab Frame}} \underbrace{\langle \Psi(0) | j_l(q\Delta r_{\mu\nu}) Y_l^{-k} \left( \theta_{\mu\nu}^{(\text{mf})}, \phi_{\mu\nu}^{(\text{mf})} \right) | \Psi(0) \rangle}_{\text{Molecular Frame Geometry}} \left. \underbrace{\mathcal{A}_{mk}^l(t) |_{\text{rigid}}}_{\text{Anisotropy}} \right\}. \end{aligned} \quad (3)$$

Equation 3 is the general form, which we adapt to our specific case by setting  $m = 0$  and replacing  $\theta_q^{(\text{lf})} \approx \theta^{(\text{d})}$  and  $\phi_q^{(\text{lf})} \approx 0$ . The resulting lab frame measurements are shown in Fig. 3 (top row).

To retrieve  $P(\mathbf{r} | \Theta, C)$ , we first isolate the molecular

frame geometry terms from Eq. 3 with a series of fits. The first projects out the measured lab frame anisotropy  $\left( Y_l^{-m} \left( \theta_q^{(\text{lf})}, \phi_q^{(\text{lf})} \right) \right)$  from Eq. 3 by fitting the angular dependence of the measured diffraction.

$$\begin{aligned} B_l^m(q, t) = & \int_0^{\pi} \langle I(\mathbf{q}(q, \theta^{(\text{d})}), t) \rangle_{\text{rigid}} Y_l^m \left( \theta_q^{(\text{lf})} \left( q, \theta^{(\text{d})} \right), \phi_q^{(\text{lf})} \left( q, \theta^{(\text{d})} \right) \right) \sin \left( \theta_q^{(\text{lf})} \left( q, \theta^{(\text{d})} \right) \right) d\theta^{(\text{d})} \\ = & \mathcal{I} \sum_{\mu, \nu: \mu \neq \nu} \text{Re} \left\{ f_{\mu}(q) f_{\nu}^*(q) i^l 8\pi^2 \sqrt{\frac{4\pi}{(2l+1)}} \right. \\ & \times \sum_k (-1)^{k-m} \underbrace{\langle \Psi(0) | j_l(q\Delta r_{\mu\nu}) Y_l^{-k} \left( \theta_{\mu\nu}^{(\text{mf})}, \phi_{\mu\nu}^{(\text{mf})} \right) | \Psi(0) \rangle}_{\text{Molecular Frame Geometry}} \left. \underbrace{\mathcal{A}_{mk}^l(t) |_{\text{rigid}}}_{\text{Anisotropy}} \right\} \end{aligned} \quad (4)$$

This yields the time ( $t$ ) and  $q$  dependent  $B_l^m(q, t)$  coefficients shown in Fig. 3 (middle row). The second fit isolates the molecular frame information through by fitting out the time dependence of  $B_l^m(q, t)$  with the simulated ADMs,  $\mathcal{A}_{mk}^l(t)$ . The resulting coefficients,  $C_{lmk}(q)$ , concisely relate measured data to the molecular frame pair-

wise geometry.

$$\begin{aligned} C_{lmk}(q) = & \mathcal{I} \sum_{\mu, \nu: \mu \neq \nu} \text{Re} \left\{ f_{\mu}(q) f_{\nu}^*(q) (-1)^{k-m} i^l 8\pi^2 \right. \\ & \times \left. \sqrt{\frac{4\pi}{(2l+1)}} \underbrace{\langle \Psi(0) | j_l(q\Delta r_{\mu\nu}) Y_l^{-k} \left( \theta_{\mu\nu}^{(\text{mf})}, \phi_{\mu\nu}^{(\text{mf})} \right) | \Psi(0) \rangle}_{\text{Molecular Frame Geometry}} \right\} \end{aligned} \quad (5)$$

$$M_{lmk}(q) = \frac{C_{lmk}(q)}{\sum_{\mu} |f_{\mu}(q)|^2}. \quad (6)$$

Here,  $M_{lmk}(q)$  are the modified  $C_{lmk}(q)$  coefficients that

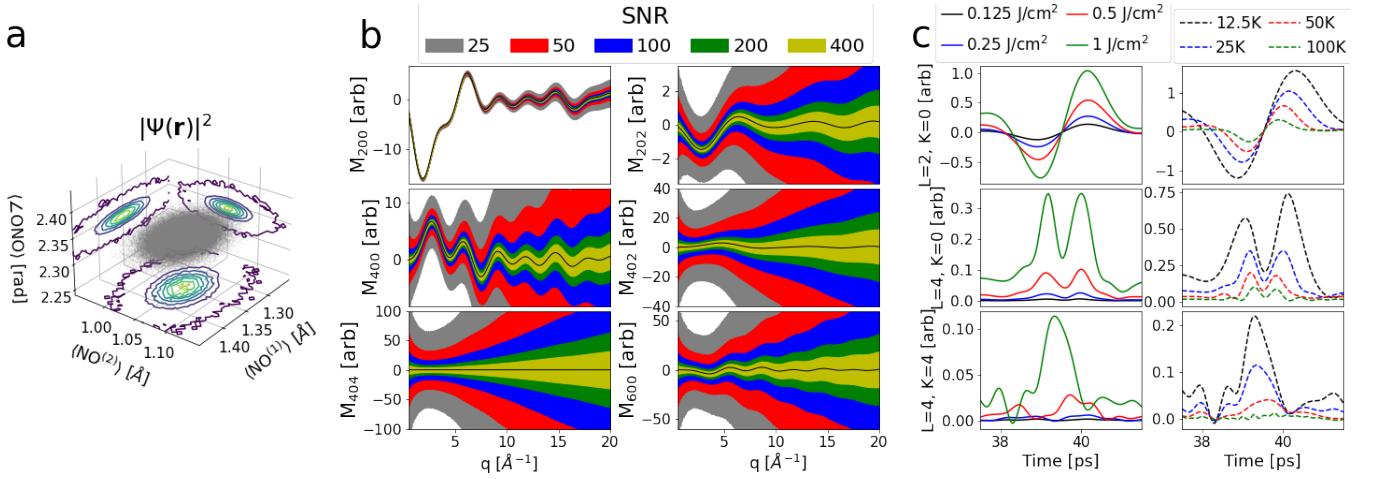


FIG. 4. For simulated NO<sub>2</sub> we defined a  $|\Psi(\mathbf{r})|^2$  distribution, from which we calculated the  $C_{lmk}(q)$  under various experimental conditions. Panel a shows the simulated NO<sub>2</sub> distribution that we use to calculate the simulated NO<sub>2</sub> responses ( $C_{lmk}(q)$  and  $M_{lmk}(q)$ ). Panel b shows  $M_{lmk}(q)$  for various SNR ratios for the case of an ensemble temperature of 100 K and kick fluence of 1 J/cm<sup>2</sup>. Panel c shows the ADMs' dependence on pump strength (constant ensemble temperature of 25 K) and temperature (constant pump fluence of 1 J/cm<sup>2</sup>).

compensate for the rapid  $q^{-4}$  falloff in the electron scattering amplitudes. For the N<sub>2</sub>O data, the poor signal to noise precludes all contributions except  $C_{200}(q)$ . Figure 3 (bottom row) shows the retrieved  $M_{lmk}(q)$  for both the simulated and measured data. Depending on the data quality and degree of orthogonality in the ADMs, one may need to employ regularization to return physical values. Regularization adds a fitting cost to extraneous coefficients, thus minimize the impact of non-orthogonal ADMs. Supplementary Section X provides further discussion on fitting the ADMs and regularization.

## B. Applying Bayesian Inferencing

Having isolated the molecular frame terms ( $C_{lmk}(q)$ ), we approximate  $|\Psi(\mathbf{r})|^2$  with a chosen model and use Bayesian Inferencing [31, 34] to adapt said model to the observed data. We again emphasize that  $\mathbf{r}$  represents the

molecular frame coordinates of the nuclei, unless otherwise stated. We approximate  $|\Psi(\mathbf{r})|^2$  with the probability distribution  $P(\mathbf{r}|\Theta, C)$ , which is parameterized by  $\Theta$  and conditioned (optimized) on the observed  $C_{lmk}(q)$  coefficients. This necessitates two key steps in the analysis. Firstly, one must choose a functional form of  $P(\mathbf{r}|\Theta, C)$  dependent on the system's state and the desired degree of accuracy. For example, one may choose a multidimensional delta function for a single molecule response, a normal distribution to model the ground state, or Hermite polynomials to describe vibronic states. Secondly, given the presumed functional form of  $P(\mathbf{r}|\Theta, C)$ , one will find the globally optimal  $\Theta$  parameters ( $\Theta^*$ ) that best describes the measured  $C_{lmk}(q)$  coefficients. Since we are retrieving the ground state geometry we ultimately want the normal distribution. The delta distribution is analogous to calculating the diffraction pattern from a single geometry and comparing it to one's measurement. This is important for intermediate results and in some cases may be the only tractable solution. Here we explicitly write out  $P(\mathbf{r}|\Theta, C)$  and the  $\Theta$  parameters

$$P(\mathbf{r}|\Theta, C) \approx |\Psi(\mathbf{r})|^2 \quad (7)$$

$$P^{(\delta)}(\mathbf{r}|\Theta, C) = \delta(\Theta^{(\delta)} - \mathbf{r}) \quad (8)$$

$$\Theta^{(\delta)} = [\langle \text{NO}^{(1)} \rangle, \langle \text{NO}^{(2)} \rangle, \langle \angle \text{ONO} \rangle] \quad (9)$$

$$P^{(N)}(\mathbf{r}|\Theta, C) = \frac{1}{\sqrt{2\pi}^{N_{\text{dof}}} \prod_{i=0}^{i < N_{\text{dof}}} \Theta_{2i+1}^{(N)}} \exp \left\{ -\frac{1}{2} \sum_{i=0}^{i < N_{\text{dof}}} \left( \frac{\Theta_{2i}^{(N)} - \mathbf{r}_i}{\Theta_{2i+1}^{(N)}} \right)^2 \right\} \quad (10)$$

$$\Theta^{(N)} = [\langle \text{NO}^{(1)} \rangle, \sigma(\text{NO}^{(1)}), \langle \text{NO}^{(2)} \rangle, \sigma(\text{NO}^{(2)}), \langle \angle \text{ONO} \rangle, \sigma(\angle \text{ONO})] \quad (11)$$

The  $\Theta$  parameters include the  $3N_{\text{atom}} - 6$  geometric degrees of freedom ( $N_{\text{dof}}$ ) needed to define the molecular geometry, and the width parameters in the case of  $P^{(\mathcal{N})}(\mathbf{r}|\Theta, C)$ . It is important to note that  $\Theta$  has the minimal number of parameters needed to define  $P(\mathbf{r}|\Theta, C)$ . Adding redundant parameters can significantly alter  $P(\Theta|C)$ .

With our chosen  $P(\mathbf{r}|\Theta, C)$  and measured  $C_{lmk}(q)$  we now retrieve  $\Theta^*$ , which is the mode of the posterior distribution  $P(\Theta|C)$ . It is required to build  $P(\Theta|C)$  and find  $\Theta^*$  in the full  $\Theta$ -space without marginalizing over individual parameters. This is because the mean and mode of  $P(\Theta|C)$  will disagree due to correlations between parameters and  $P(\Theta|C)$ . Consequently, we must next tackle the curse of dimensionality.

### C. Solving for the high dimensional model parameters $\Theta$

We retrieve  $P(\Theta|C)$  with the Metropolis Hastings algorithm (MHA) from the following system of equations:

$$C_{lmk}(q) = \int H_{lmk}(q, \mathbf{r}) |\Psi(\mathbf{r})|^2 d\mathbf{r} \quad (12)$$

$$C_{lmk}^{(\text{calc})}(q, \Theta) = \int H_{lmk}(q, \mathbf{r}) P(\mathbf{r}|\Theta, C) d\mathbf{r} \quad (13)$$

$$H_{lmk}(q, \mathbf{r}) = \mathcal{I}\text{Re} \left\{ i^l (-1)^{k-m} 8\pi^2 \sqrt{\frac{4\pi}{(2l+1)}} \right. \\ \left. \times \sum_{\mu, \nu: \mu \neq \nu} |f_\mu(q)| |f_\nu(q)| j_l(q\Delta r_{\mu\nu}) Y_l^{-k}(\theta_{\mu\nu}^{(\text{mf})}, \phi_{\mu\nu}^{(\text{mf})}) \right\}. \quad (14)$$

We note the high dimensionality and complexity of Eq. 13, which is a system of order 10 equations, each with order 100 terms, embedded in an order 100-dimensional space of  $q$  bins. This must be evaluated on a  $N_{\text{dof}}$ -dimensional space of all possible molecular geometries and width parameters. The MHA is chosen for its ability to retrieve probability distributions from high dimensional integral equations like Eq. 13 [34, 36].

The MHA is designed to efficiently and preferentially sample regions of  $\Theta$ -space proportional to the agreement with data, spending the vast majority of its time sampling regions of high probability. The MHA builds  $P(\Theta|C)$  by accumulating  $\Theta$  parameters based on comparing their likelihood to neighboring  $\Theta'$  parameters. For instance, if the likelihood of  $\Theta$  is 1000 times larger than  $\Theta'$ , the MHA will visit  $\Theta'$  once for every 1000 visits to  $\Theta$ . This likelihood is the probability of observing the data  $C_{lmk}(q)$  with a corresponding standard error of the

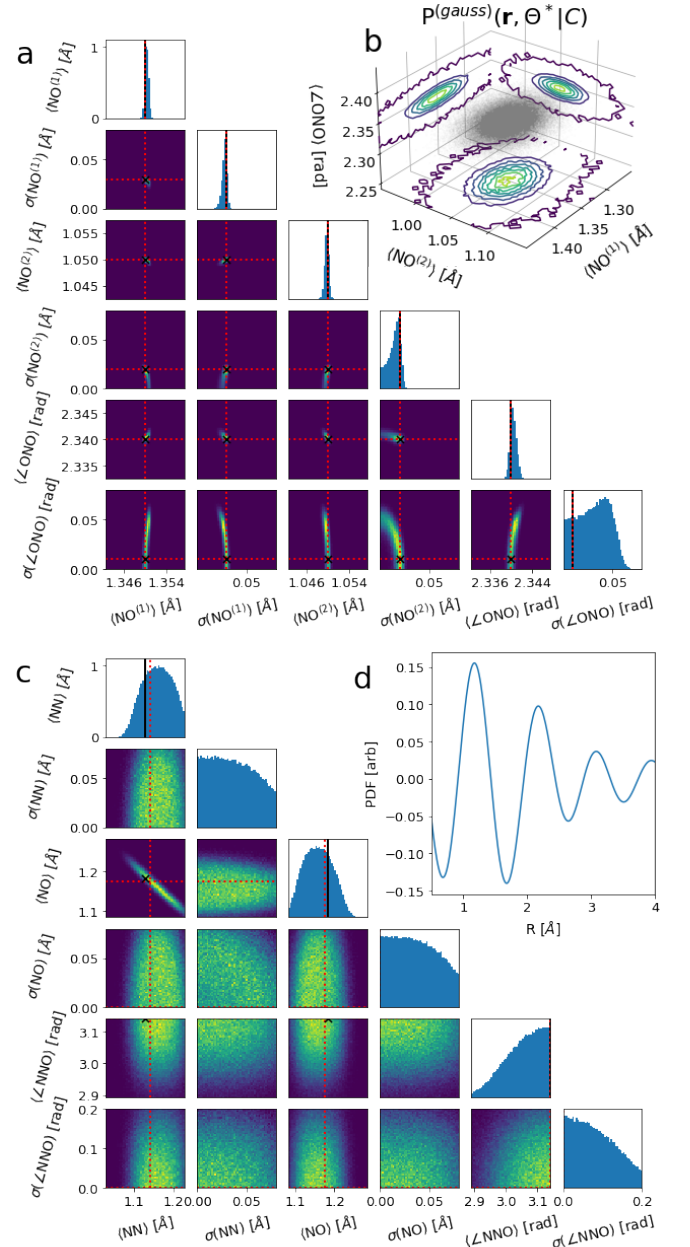


FIG. 5. We successfully retrieve the multidimensional posterior  $P^{(\mathcal{N})}(\Theta|C)$  for NO<sub>2</sub> and N<sub>2</sub>O from which we find  $\Theta^*$ . Panel a shows the 1d and 2d projections of the retrieved  $P^{(\mathcal{N})}(\Theta|C)$  distributions for the simulated NO<sub>2</sub> response. The recovered  $P^{(\mathcal{N})}(\mathbf{r}|\Theta^*, C)$  (panel b) is what we compare to Fig. 4a. The red dashed lines indicate  $\Theta^*$ , while the black “x” and solid black lines indicate the ground truth, respectively. Panel c shows the 1d and 2d projections of the retrieved  $P^{(\mathcal{N})}(\Theta|C)$  distributions for N<sub>2</sub>O data, though only using the  $C_{200}(q)$  contribution. The black “x” and solid black lines indicate previously measured values for N<sub>2</sub>O [35]. For comparison, panel d shows the simulated PDF from the same  $q$  range.

mean  $\sigma_{lmk}(q)$ , given the parameters  $\Theta$ :

$$P(C|\Theta) = \left[ \prod_{lmk,q} \frac{1}{\sigma_{lmk}(q)\sqrt{2\pi}} \right] e^{K(\Theta)} \times \exp \left\{ \frac{-1}{2} \sum_{lmk,q} \left( \frac{C_{lmk}(q) - C_{lmk}^{(\text{calc})}(q, \Theta)}{\sigma_{lmk}(q)} \right)^2 \right\}. \quad (15)$$

Here,  $K(\Theta)$  is used to constrain parameters to physicality e.g.,  $\Theta > 0$  and  $\angle\text{ONO} < \pi$ . We note the likelihood function, and hence the MHA, is theory independent and is analogous to a random walk guided by the relative agreement of neighboring  $\Theta$  parameters to the data. Reference [34] gives a detailed description of combining Bayesian Inferencing and the MHA, as well as the MHA python package used in this work. Supplementary Section XI describes our use of the MHA and Bayesian Inferencing in greater detail and how one can introduce physical intuition, or *a priori* knowledge, into the MHA.

The measured  $q$  range, the induced rotational wavepacket, and the  $\sigma_{lmk}(q)$  are vital in determining the width, shape, and parameter correlations of  $P(\Theta|C)$ . To investigate such dependencies we first define a  $|\Psi(\mathbf{r})|^2$  distribution for  $\text{NO}_2$  to calculate  $C_{lmk}(q)$ . Figure 4a and Table I show and describe this distribution, respectively. Measuring more diffraction patterns increases the signal to noise ratio (SNR) by reducing  $\sigma_{lmk}(q)$  which scales as  $1/\sqrt{N}$ . Here, the SNR is the geometric mean of  $C_{000}(q)/\sigma_{000}(q)$  between  $0.5 < q < 4 \text{ \AA}^{-1}$ . Figure 4b illustrates the  $C_{lmk}(q)$  coefficients used in this analysis with the following SNRs based on previous UED [37] and x-ray [8] diffraction experiments: 25, 50, 100, 200, 400. To calculate  $\sigma_{lmk}(q)$  for  $\text{NO}_2$  we add Poisson noise to the diffraction patterns and propagate that noise through the lab frame anisotropy and ADM fits outlined above (see Supplementary Section XII). For the  $\text{N}_2\text{O}$  data, Supplementary Section XII describes the data processing and retrieval of  $\sigma_{lmk}(q)$ . Increasing the average pump fluence by increasing the pump pulse FWHM induces a larger rotational coherence while increasing the ensemble temperature increases the spread of initial rotational states. Figure 4c shows how the ADMs' amplitudes increase and decrease by increasing the pump fluence and ensemble temperature, respectively. We also note the ADMs oscillate faster and with more complexity as both the pump fluence and temperature increase. Unless otherwise stated, the standard configuration of experimental parameters for our  $\text{NO}_2$  results is a  $q$  range of  $[0.5, 10] \text{ \AA}^{-1}$ , a SNR of 100, a pump fluence of  $1 \text{ J/cm}^2$  and a 100 K ensemble temperature.

This method ultimately yields the following three results; a distribution of  $\Theta$  parameters (the posterior  $P(\Theta|C)$ ), the optimal set of model parameters ( $\Theta^*$ ), and a parameterized probability of molecular geometries  $P(\mathbf{r}|\Theta^*, C)$ . For each individual  $\Theta$  parameter, where the  $i^{\text{th}}$  parameter is denoted as  $\Theta_i$ , we calculate its resolution as the standard deviation of the projection onto

$\Theta_i$ . This resolution,  $\sigma^\Theta$ , is the one dimensional standard deviation after marginalizing over all other parameters, which removes the correlations between  $\Theta$  parameters. That is, if one randomly draws some parameters  $\Theta$  from  $P(\Theta|C)$ , the distribution of parameter  $\Theta_i$  will have a width of  $\sigma^\Theta$ . The mean and mode of said marginalized distribution will likely not correspond to  $\Theta^*$ , since  $\Theta^*$  is the mode of the full  $\Theta$ -space distribution. We find  $\Theta^*$  via a simple mode search algorithm based on a weighted averaging search (see Supplementary Section XIII).

### III. RESULTS

To illustrate our method's efficacy, we retrieve  $P^{(\mathcal{N})}(\mathbf{r}|\Theta^*, C)$  from both simulated  $\text{NO}_2$   $C_{lmk}(q)$  coefficients under varying experimental conditions and measured  $\text{N}_2\text{O}$  data. As discussed, we first build the posterior  $P^{(\mathcal{N})}(\Theta|C)$  which is shown in Fig. 5 for simulated  $\text{NO}_2$  (a) and measured  $\text{N}_2\text{O}$  data (c). Panels b and d show  $P^{(\mathcal{N})}(\mathbf{r}|\Theta^*, C)$  for  $\text{NO}_2$  and the simulated PDF for  $\text{N}_2\text{O}$ , respectively. Tables I and II give the extracted  $\Theta^*$  and  $\sigma^\Theta$  for  $\text{NO}_2$  and  $\text{N}_2\text{O}$ , respectively. For  $\text{NO}_2$ ,  $P^{(\mathcal{N})}(\Theta|C)$ , of width  $\sigma^\Theta \sim 30 \text{ fm}$ , fully encompasses the ground truth values. Despite the largely flat  $\langle\angle\text{ONO}\rangle$  distribution,  $\Theta^*$  still converges on the ground truth values. For  $\text{N}_2\text{O}$  data, the retrieved  $P^{(\mathcal{N})}(\Theta|C)$  encompasses the previously measured results of Ref. [35]. The uncorrelated widths of this distribution  $\sigma^\Theta$  are of order picometers even with our limited  $q$  range of  $[3.5, 7.25] \text{ \AA}^{-1}$  and a very poor SNR. Most notably, the retrieved  $\langle\angle\text{NNO}\rangle$  is  $\pi$  and we resolve the  $\sim 5 \text{ pm}$  difference between the  $\text{N}^{\text{T}}\text{N}^{\text{C}}$  and  $\text{N}^{\text{C}}\text{O}$  bond distances (Table II). The retrieved widths  $\sigma(\text{N}^{\text{T}}\text{N}^{\text{C}})$  and  $\sigma(\angle\text{NNO})$  are unphysical due to the limited  $q$  range, as discussed later. The PDF peaks'  $\sim 25 \text{ pm}$  widths (Fig. 5d), are an order of magnitude larger than our resolution. The missing low and high  $q$  components produce ringing artifacts in this inverse Fourier Transform because of the incomplete Fourier space. This confuses the PDF results as they are not positive definite and these artifacts can be substantial at large distances.

Figure 5a and c both show how  $\Theta^*$  does not correspond to the mean or mode of most  $P^{(\mathcal{N})}(\Theta|C)$  projections. This is due to the non-linearity and correlations of  $P(\Theta|C)$  in  $\Theta$  space. The plotted  $P(\Theta|C)$  projections trace over variables. Tracing over variables removes correlations that are important to the resolution of  $P(\Theta|C)$  and accuracy of  $\Theta^*$ . We must find  $\Theta^*$  in this correlated space since the geometry parameters are indeed correlated.

Our main results are given in Figs. 5 and Tables I and II. We now show how these results would behave by altering experimental parameters. Figures 6, 7, and 8 show these exploratory results.

Expanding the measured  $q$  range improves  $\sigma^\Theta$  only until  $\sim 8 \text{ \AA}^{-1}$ , but continuous to reduce false correlations between  $\Theta$  parameters beyond this. Figure 6a summa-



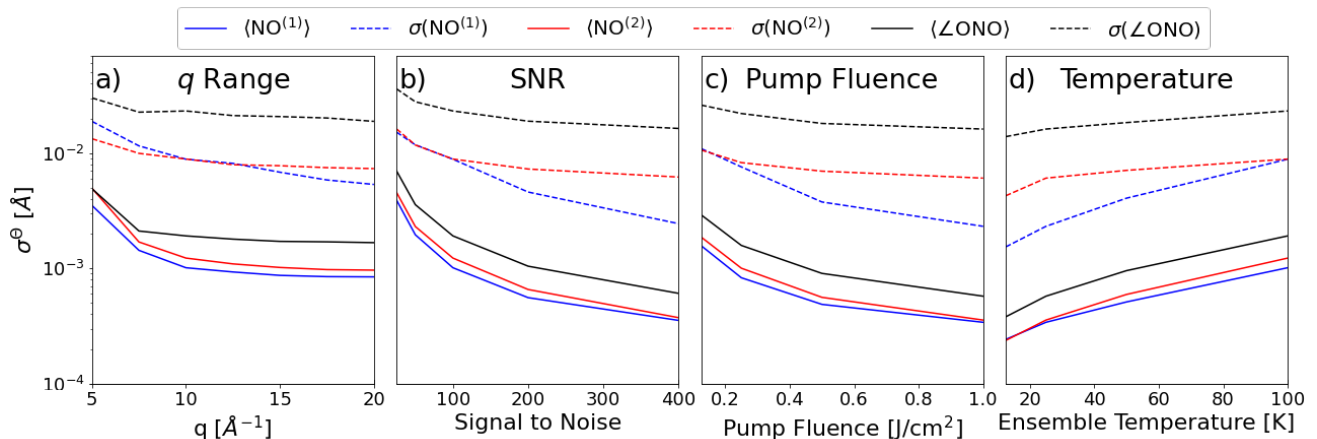


FIG. 6. Varying experimental parameters affects the resolution (width) of  $P^{(\mathcal{N})}(\Theta|C)$ , but our method is most sensitive to SNR. Panel a shows how the uncorrelated widths of  $P^{(\mathcal{N})}(\Theta|C)$ , denoted by  $\sigma^\Theta$ , changes by increasing  $q$  range. Panel b similarly shows the dependence of  $\sigma^\Theta$  and  $\Theta^*$  error versus SNR. Panel c shows the dependence of  $\sigma^\Theta$  and  $\Theta^*$  error versus pump fluence (width of the rotational wavepacket). Panel d shows the dependence of  $\sigma^\Theta$  and  $\Theta^*$  error versus the molecular ensemble temperature.

	Input	$\Theta^*$	$\sigma^\Theta$
$\langle \text{NO}^{(1)} \rangle [\text{\AA}]$	1.35	1.3500	0.00029
$\sigma(\text{NO}^{(1)}) [\text{\AA}]$	0.03	0.03000	0.0019
$\langle \text{NO}^{(2)} \rangle [\text{\AA}]$	1.05	1.0500	0.00029
$\sigma(\text{NO}^{(2)}) [\text{\AA}]$	0.02	0.02000	0.0054
$\langle \angle \text{ONO} \rangle [\text{rad}]$	2.34	2.340	0.00047
$\sigma(\angle \text{ONO}) [\text{rad}]$	0.01	0.01010	0.015

TABLE I. We provide the input  $\Theta$  parameters for our  $\text{NO}_2$  simulation, the retrieved  $\Theta^*$  and the uncorrelated widths of  $P(\Theta|C)$ ,  $\sigma^\Theta$ .

	$\Theta^*$ Literature	$\Theta^*$	$\sigma^\Theta$
$\langle \text{N}^{\text{T}}\text{N}^{\text{C}} \rangle [\text{\AA}]$	1.128	1.142	0.039
$\sigma(\text{N}^{\text{T}}\text{N}^{\text{C}}) [\text{\AA}]$		0.081	0.028
$\langle \text{N}^{\text{C}}\text{O} \rangle [\text{\AA}]$	1.184	1.175	0.036
$\sigma(\text{N}^{\text{C}}\text{O}) [\text{\AA}]$		$3.08 \times 10^{-8}$	0.027
$\langle \angle \text{NNO} \rangle [\text{rad}]$	3.142	3.142	0.061
$\sigma(\angle \text{NNO}) [\text{rad}]$		$5.5 \times 10^{-12}$	0.062

TABLE II. We provide the literature values of  $\Theta^*$  [35] with the retrieved  $\Theta^*$ , along with the uncorrelated widths,  $\sigma^\Theta$ , from the  $\text{N}_2\text{O}$  data.

izes how  $\sigma^\Theta$  decreases and then plateaus with increasing  $q$  range. Increasing the measured reciprocal range  $q$  provides more information about the system and reduces correlations in  $P(\Theta|C)$  (Fig. 7). Since these correlations diminish with added information, we refer to them as false correlations. Figures 7a and c illustrate how the false correlations diminish from a  $q$  range of  $[0.5, 5] \text{\AA}^{-1}$  to  $[0.5, 20] \text{\AA}^{-1}$ , respectively, under conditions of SNR of 100 and a fluence of  $1 \text{ J/cm}^2$ . The plotted correlation in Fig. 7e is between all six  $\Theta$  parameters.

Our method is strongly sensitive to SNR due to our sta-

tistical interpretation. Figure 6b shows that  $\sigma^\Theta$  rapidly decreases with increasing SNR with  $q$  of  $[0.5, 10]$ . Increasing SNR by an order of magnitude decreases  $\sigma^\Theta$  by an order of magnitude for pair-wise distances and angles. The shape of  $P^{(\mathcal{N})}(\Theta|C)$  does not change since we are not adding new information given the fixed  $q$  range.

Increasing the induced rotational coherence and lowering the ensemble temperature improves the measured resolution similarly to increasing the SNR. This is caused by the increased magnitude and variation in the ADMs (Fig. 4c). Figure 6c and d show how rapidly  $P(\Theta|C)$  resolution improves by increasing rotational coherence (25 K ensemble temperature) and decreasing ensemble temperature ( $1 \text{ J/cm}^2$  pump fluence), respectively

Generally, when varying the  $q$  range, SNR levels, pump fluence, and ensemble temperature we find the pair-wise distances'  $\sigma^\Theta$  to be of order 100 fm; for the width parameters,  $\sigma^\Theta$  is order 1 pm. Our retrieved  $\Theta^*$  values are generally within a relative error of  $\sim 10^{-7}$  and  $\sim 10^{-3}$  from the ground truth values for geometric parameters and width parameters, respectively. This resolution is often  $\sim 100$  times better than PDF based methods because our statistical treatment is highly sensitive to SNR.

As noted above, we run the intermediate delta distribution on the same  $\text{NO}_2$  simulation (Fig. 4). With  $P^{(\delta)}(\mathbf{r}|\Theta, C)$ , we assume a single molecule response can describe a signal averaged over an ensemble of geometries. This systematic error introduces an order of magnitude increase in  $\sigma^\Theta$ . When increasing  $q$ ,  $P^{(\delta)}(\Theta|C)$  seems to converge in an unstable fashion on the ground truth (Fig. 8), unlike  $P^{(\mathcal{N})}(\mathbf{r}|\Theta, C)$ . We note that this calculation runs  $\sim 100$  times faster than  $P^{(\mathcal{N})}(\Theta|C)$  since it doesn't have to sum over many geometries in Eq. 13. For this reason  $P^{(\delta)}(\mathbf{r}|\Theta, C)$  primarily serves as the intermediate to quickly test one's analysis before switching to the normal distribution. For large molecules,

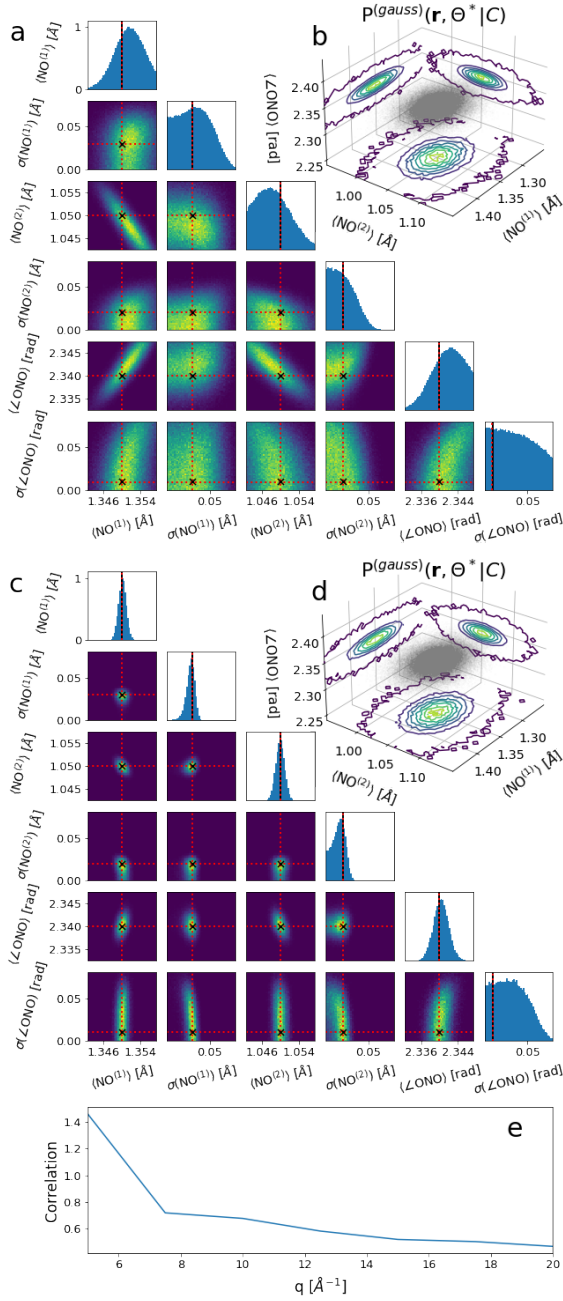


FIG. 7. Varying the measured  $q$  range affects false correlations in  $P^{(N)}(\Theta|C)$  for  $\text{NO}_2$ ; a larger reciprocal space provides more information and dampens false correlations. Panel a shows the 1d and 2d projections of  $P^{(N)}(\Theta|C)$  for a limited  $q$  range of  $[0.5, 5] \text{ \AA}^{-1}$ . The red dashed lines illustrate  $\Theta^*$ , while the black “X” and solid lines indicate the ground truth values. Panel b shows the corresponding  $P^{(N)}(\mathbf{r}|\Theta^*, C)$ . Similarly, panel c shows the 1d and 2d projections of  $P^{(N)}(\Theta|C)$  for the broader  $q$  range of  $[0.5, 20] \text{ \AA}^{-1}$ . Panel d shows the corresponding  $P^{(N)}(\mathbf{r}|\Theta^*, C)$ . Panel e shows the correlation between all  $\Theta$  parameters as a function of  $q$  range. We note the decrease in correlations with larger  $q$ , where panels a and b illustrate how the width and false correlations in  $P^{(N)}(\Theta|C)$  decrease with higher  $q$ .

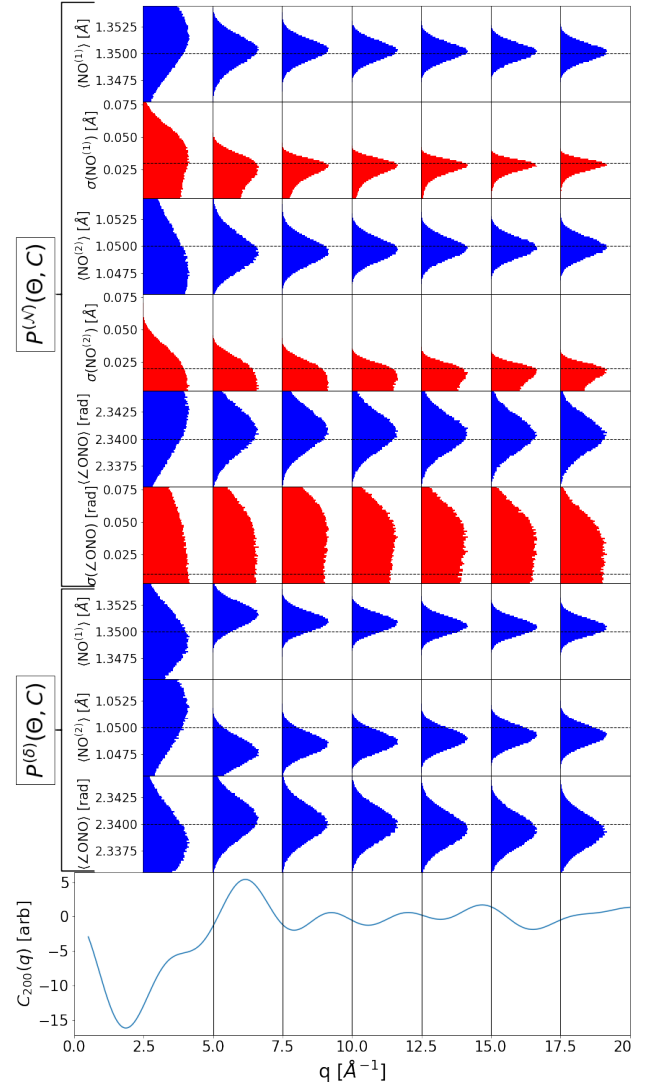


FIG. 8. The  $P^{(\delta)}(\Theta|C)$  distribution suffers from a  $q$  dependent systematic error stemming from the false assumption that a single geometry describes the results measured from an ensemble. Here we show the 1d projections of  $P^{(\delta)}(\Theta|C)$  and  $P^{(N)}(\Theta|C)$  as a function of measured  $q$  range. Each column indicates a different  $q$  range starting at  $0.5 \text{ \AA}^{-1}$  with the end of said  $q$  range indicated by the right most border of that column. The dashed lines are the ground truth values. The bottom plot is the simulated  $C_{200}(q)$  coefficient used for both posteriors and is intersected by black lines that indicate the upper  $q$  range of each column.

$P^{(\delta)}(\mathbf{r}|\Theta, C)$  may be the only tractable method. Supplementary Section XIV provides plots and further discussion of these results.

#### IV. DISCUSSION

We divide the following discussion into three categories covering the two major points of our analysis and how

one may extend it to excited states dynamics. Firstly, we provide intuition for the need of induced anisotropy to access the molecular frame geometric angles  $\theta_{\mu\nu}^{(\text{mf})}$  and  $\phi_{\mu\nu}^{(\text{mf})}$ . Secondly, we will compare conventional PDF based methods to our Bayesian Inferencing approach. We also discuss how systematic errors and various experimental parameters affect the MHA results. Finally, we introduce methods to evaluate excited state dynamics by evaluating only the isotropic component and by introducing a separation of timescale approximation to Eq. 2. Both

these methods do not require any complex excited state dynamic simulations.

### A. The Role of Anisotropy

To provide intuition for the distinct angular terms, we condense and label the important reference frames from Eq. 2

$$\langle I(q)_{\text{mol}} \rangle = \dots \sum_{m,k} (-1)^{k-m} \underbrace{Y_l^{-m}(\theta_q^{(\text{lf})}, \phi_q^{(\text{lf})})}_{\text{Lab Frame}} \underbrace{D_{mk}^l(\phi_1^{(\text{lf})}, \theta_1^{(\text{lf})}, \chi_1^{(\text{lf})})}_{\text{Ensemble Anisotropy}} \underbrace{j_l(q\Delta r_{\mu\nu}) Y_l^{-k}(\theta_{\mu\nu}^{(\text{mf})}, \phi_{\mu\nu}^{(\text{mf})})}_{\text{Molecular Frame Geometry}} |\Psi(t)\rangle. \quad (16)$$

The molecular frame geometry component separates into distance and angular terms. The former is the pair-wise distance term ( $j_l(q\Delta r_{\mu\nu})$ ) that governs the  $q$  dependence. The latter ( $Y_l^{-k}(\theta_{\mu\nu}^{(\text{mf})}, \phi_{\mu\nu}^{(\text{mf})})$ ), is the angular decomposition of the molecular geometry and acts as a scaling parameter. This molecular frame geometry term is coupled to the measured lab frame anisotropy ( $Y_l^{-m}(\theta_q^{(\text{lf})}, \phi_q^{(\text{lf})})$ ) by the ensemble anisotropy. The ensemble anisotropy,  $D_{mk}^l(\phi_1^{(\text{lf})}, \theta_1^{(\text{lf})}, \chi_1^{(\text{lf})})$ , acts as a key from the measured lab frame diffraction pattern to the molecular frame geometry. Similar derivations in Refs. [38] and [39] exist but do not stress the dependence on molecular frame coordinates; Ref. [38] is not treated fully quantum mechanically as done here in Supplementary Section IX. Anisotropy is required for our method to have an explicit dependence on the pair-wise angles. Without anisotropy,  $C_{000}(q)$  has no explicit angular dependence (Eq. 5), just like the PDF.

Stronger impulsive alignment produces a broader coherent rotational wavepacket which exhibits higher amplitude signals with more variations (Fig. 4c). Larger amplitude ADMs improve  $C_{lmk}(q)$  SNR by lifting higher order coefficients up out of the noise, resulting in similar resolution improvements to only increasing SNR, shown in Fig. 6c. Increasing the number of  $C_{lmk}(q)$  coefficients improves the  $\theta_{\mu\nu}^{(\text{mf})}$  and  $\phi_{\mu\nu}^{(\text{mf})}$  resolution since each  $C_{lmk}(q)$  provides a new angular constraint via  $Y_l^{-k}(\theta_{\mu\nu}^{(\text{mf})}, \phi_{\mu\nu}^{(\text{mf})})$  (Eq. 5).

One can produce fast signal variations with an initially broad hot thermal ensemble. Writing coherence onto hotter molecular ensembles produces weak but fast varying ADMs, shown in Fig. 4c. Figure 6d shows how quickly the resolution worsens at higher temperatures. When fitting the ADMs to  $B_l^m(q, t)$ , one ideally measures particular points that include two separate regions where the ADMs have high variation and sufficiently before and after the prominent anisotropy signal where their magnitude dampens. We note, however, one need not strictly measure the entire transient rotational signal.

When simulating or inducing molecular tumbling is prohibitively difficult, one may use the induced anisotropy from the photo-excitation. Producing sufficiently large rotational coherences in large molecules is challenging. The option of using dipole alignment from the excitation pulse allows this technique to be more generally applicable to most molecular systems of interest.

### B. Bayesian Inferencing and the MHA

We use Bayesian Inferencing to retrieve  $P(\Theta|C)$  and ultimately the  $P(\mathbf{r}|\Theta^*, C)$  distribution.  $P(\mathbf{r}|\Theta^*, C)$  is significantly more information rich than the simple PDF. Our method decomposes anisotropic diffraction into individual  $C_{lmk}(q)$ , each of which independently constrains  $P(\Theta|C)$  and consequently the molecular geometries. The  $P(\mathbf{r}|\Theta^*, C)$  distribution, which approximates  $|\Psi(\mathbf{r})|^2$ , allows us to find the most probable pair-wise distances and angles to define a most-likely geometry that is unique. Traditionally, an ideal PDF derived from an infinite  $q$  range, being the inverse Fourier transform of  $qM_{000}(q)$ , is at best a weighted histogram of unlabeled pair-wise distances. Since our measurements necessarily do not measure  $q$  all the way to 0, and the signal drop-off limits our ability to measure high  $q$ , our  $q$  range is always limited. These limitations obfuscate the PDF interpretations by introducing sinusoidal systematics that result in negative probabilities, shown in Fig 5d where we do not expect any distance above 2.3 Å. To alleviate the ambiguity of Fig. 5d, we typically simulate  $|\Psi(\mathbf{r})|^2$  with *a priori* knowledge and validate simulation against the measured PDF. Instead of this traditional approach, our method uncovers the globally optimal parameters ( $\Theta^*$ ) from the data for a given  $P(\mathbf{r}|\Theta, C)$ . This requires only the initial ground state geometry, simulations of the coherent rotational wavepacket when using  $C_{lmk}(q)$  for  $l > 0$ , and for excited state dynamics one additionally needs relevant transition dipole moments. As made clear by comparing

Figs. 5b and d, the  $P(\mathbf{r}|\Theta^*, C)$  distribution is significantly more information rich than the simple PDF, e.g. it provides the 3d molecular geometry and width of the  $|\Psi(\mathbf{r})|^2$ . This method thus has the potential to shift ultrafast diffraction to a discovery method applicable even to systems that extend beyond the scope of theory.

Our method retrieves the labelled pair-wise distances with  $\sim 100$  times better resolution than the PDF. This is due to our statistical treatment using Bayesian Inferencing and the MHA. In the MHA, each  $lmk$  and  $q$  contribution is itself a probability distribution; each is an experiment of its own. When adding a new  $\Theta$  to  $P(\Theta|C)$  the relative ratio of the likelihood function  $P(C|\Theta)$  (Eq. 15) decreases since each additional  $C_{lmk}(q)$  increases the magnitude of the negative exponent. That is, with more measurements Eq. 15 becomes smaller and  $P(\Theta|C)$  becomes sharper. Our method therefore heavily relies on  $\sigma_{lmk}(q)$  and  $C_{lmk}(q)$ . Statistical noise tends to increase  $\sigma_{lmk}(q)$ , making  $P(\Theta|C)$  wider ( $\sigma^\Theta$  larger), while systematic errors in  $C_{lmk}(q)$  tend to shift the centroid of  $P(\Theta|C)$ , as seen in the  $\text{N}_2\text{O}$  data. Supplementary Section XII describes our method for consistently accounting for both statistical and systematic errors. The PDF error adds in quadrature in  $\sigma_{lmk}(q)$ ; its scale is set by the largest error bar and disproportionately suffers from poorly measured data points. Conversely, since each term of the negative sum in the argument of the exponent in Eq. 15 is weighted by  $1/\sigma_{lmk}(q)$ , the MHA reduces the contribution from poorly measured data points while increasing the effect of high precision measurements.

Our Bayesian Inferencing approach expands the utility of gas-phase ultrafast diffraction to measure previously inaccessible variables, such as the width of  $|\Psi(\mathbf{r})|^2$ . Given  $P(\mathbf{r}|\Theta, C)$  is a generic function parameterized by  $\Theta$ , one can introduce variables through  $\Theta$  by selecting a  $P(\mathbf{r}|\Theta, C)$  that depends on it. Here, we expanded the measurable parameters of gas-phase ultrafast diffraction to include the width of  $|\Psi(\mathbf{r})|^2$ .  $P^{(N)}(\mathbf{r}|\Theta, C)$  quantifiably measures  $|\Psi(\mathbf{r})|^2$  width and reduces the systematic effects from assuming a single geometry, illustrated in Fig. 8, even when  $|\Psi(\mathbf{r})|^2$  is not well modeled by a Gaussian. One can choose a more accurate  $P(\mathbf{r}|\Theta^*, C)$  for their system e.g., one may choose Hermite polynomials for vibrationally excited states. For the  $\text{N}_2\text{O}$  data, our  $q$  range of  $[3.5, 7.25] \text{ \AA}^{-1}$  is insufficient to resolve the width of  $|\Psi^{(\text{N}_2\text{O})}(\mathbf{r})|^2$ , making the width a nuisance fit parameter used to avoid the above-mentioned systematic errors induced by the delta distribution. Instead, we can use the retrieved distances from  $\Theta^*$  (using the normal distribution) as input into the delta distribution in order to approximate  $|\Psi(\mathbf{r})|^2$ .

The MHA performs an unbiased search through  $\Theta$  space guided by the  $C_{lmk}(q)$  coefficients and correlates each  $\Theta$  parameter. Our method is model independent and does not suffer from model bias as might be a concern for conventional methods. Simultaneously evaluating each  $\Theta$  parameter artificially introduces correlations between them. Since  $\Theta$  is the minimal set of parameters

to define  $P(\mathbf{r}|\Theta, C)$ , we expect the parameters to be uncorrelated. Figure 7 shows how adding information by extending the  $q$  range decreases false correlations, which are caused by integrating over insufficiently large  $q$  regions. For the  $\text{N}_2\text{O}$  data, we observe these false correlations, most notably between  $\langle \text{N}^{\text{T}}\text{N}^{\text{C}} \rangle$  vs  $\langle \text{N}^{\text{C}}\text{O} \rangle$  (Fig. 5c). Simultaneously evaluating all  $\Theta$  parameters leverages well-resolved parameters to constrain poorly resolved parameters. For example, the long OO bond (or  $\angle\text{ONO}$ ) in our asymmetric  $\text{NO}_2$  is the best constrained parameter as it produces the most  $q$  oscillations. The MHA removes geometries where the two NO distances are inconsistent with the well-resolved OO distance. These correlations similarly help find  $\Theta^*$ , as observed with  $\text{N}_2\text{O}$ , where the  $P^{(N)}(\Theta|C)$  uncorrelated widths do not distinguish the  $\text{N}^{\text{T}}\text{N}^{\text{C}}$  and  $\text{N}^{\text{C}}\text{O}$  bonds but  $\Theta^*$  does.

The width of  $P(\Theta|C)$  ( $\sigma^\Theta$ ) relies heavily on SNR rather than increased  $q$  range, which is ideal since it is generally prohibitively difficult to change the  $q$  range at ultrafast diffraction facilities and easier to reduce the SNR by taking more measurements. Similarly, Ref. [40] illustrated the importance of SNR. Below  $8 \text{ \AA}^{-1}$ ,  $\sigma^\Theta$  for the pair-wise distances and angles quickly decreases as the  $q$  range increases, shown in Figs. 6a and 7. Above  $8 \text{ \AA}^{-1}$ ,  $\sigma^\Theta$  for the pair-wise distances and angles does not change significantly. In contrast,  $\sigma^\Theta$  continuously decreases with improved SNR, shown in Fig. 6b. This is because smaller  $\sigma_{lmk}(q)$  makes it less probable for the MHA to visit  $\Theta$  parameters with larger residuals. Which is again due to increasing the magnitude of the exponential's argument in Eq. 15. For the PDF, the resolution goes as  $2\pi/\Delta q$ , or 1.26, 0.63, and  $0.31 \text{ \AA}$  for  $q$  ranges of 5, 10, and  $20 \text{ \AA}^{-1}$  respectively, which is roughly 1000 times larger than our observed resolution for  $\text{NO}_2$ . Our method therefore lends itself well to high repetition-rate machines, such as the upcoming LCLS II. We note that increasing the  $q$  range above  $8 \text{ \AA}^{-1}$  has a larger effect on the width parameters (dashed lines of Fig. 6a) and that one may prioritize higher  $q$  over SNR if they are more interested in the width of  $|\Psi(\mathbf{r})|^2$ .

### C. Potential Extension to Excited State Dynamics

Our method is broadly applicable to diffraction experiments with laser excitation, including dynamics from excited electronic states. Here, the laser excitation imparts one or more units of angular momentum providing at least the anisotropy terms  $C_{20k}(q)$ . From  $\text{N}_2\text{O}$  data and from low SNR  $\text{NO}_2$  simulations we see that the  $C_{200}(q)$  alone recovers  $\sim 4 \text{ pm}$  resolution. The primary difficulty with extending our method to excited states dynamics lies in isolating the ADMs in rovibronically coupled systems at sufficiently long timescales. Since the principle moments of inertia change with the geometry, one must reorient the altered excited state molecular geometry by adding three molecular frame Euler angles to the  $\Theta$  parameters. The generally much wider width of  $|\Psi(\mathbf{r}, t)|^2$  in

the excited state dampens the  $C_{lmk}(q)$  coefficients faster than the ground state signal, reducing the need for extending  $q$ . Next we discuss two variants, a time separable method and an isotropic method. Both variations isolate the ADMs as we did in the rigid-rotor approximation.

The time separable method introduces a separation of time scales since the vibronic dynamics are typically

much faster than the rotational dynamics. Here we assume the ADMs are relatively stationary during the vibronic motion. This approximation is analogous to the Born-Oppenheimer approximation and allows us to separate the rotational and vibronic timescales. Applying this approximation to an experiment with a single excitation pulse, the measured results are given by Eq. 17,

$$\begin{aligned} \langle I(\mathbf{q}) \rangle_{\text{sep}}^{(1)}(t) = & \mathcal{I} \left( \sum_{\mu} |f_{\mu}(q)|^2 + \sum_{\mu, \nu: \mu \neq \nu} \text{Re} \left\{ f_{\mu}(q) f_{\nu}(q) \sum_l i^l 8\pi^2 \sqrt{\frac{4\pi}{(2l+1)}} \right. \right. \\ & \left. \left. \times \sum_{m_1, m_2} (-1)^{m_1 - m_2} Y_l^{-m_2} \left( \theta_q^{(\text{lf})}, \phi_q^{(\text{lf})} \right) \langle \Psi_{\text{vib}}(t) | j_l(q\Delta r_{\mu\nu}) Y_l^{-m_1} \left( \theta_{\mu\nu}^{(\text{mf})}, \phi_{\mu\nu}^{(\text{mf})} \right) | \Psi_{\text{vib}}(t) \rangle \mathcal{A}_{m_2 m_1}^l(0) \right\} \right). \end{aligned} \quad (17)$$

Here,  $\mathcal{A}_{m_2 m_1}^l(0)$  are the ADMs calculated with respect to the ground state geometry and evaluated immediately after laser excitation. The dipole selection rule induces the above anisotropy, and for a single photon transition provides at least the  $C_{20k}(q, t)$  coefficients. This variation is independent of one's ability to induce a rotational wavepacket, particularly for large molecules. However, it requires knowledge of either the transition dipole moment or the Frank-Condon factor and the ground state dipole.

To further constrain  $P(\Theta|C)$ , one can couple to more  $C_{lmk}(q)$  coefficients by introducing a precursor pulse that excites a rotational wavepacket. This precursor pulse,

assumed to be a rotational Raman impulse, is chosen to have a negligible effect on the vibronic system thus maintaining consistency with our separation of timescale approximation. The Raman impulse first induces the rotational coherence. Following the Raman impulse, the system evolves for a rotational time  $\tau$ , at this point the vibronic excitation pulse arrives. One would measure the vibronic dynamics over a small window ( $t \ll \tau$ ) for different orientations by also scanning the delay  $\tau$  over an appreciable portion of the rotational evolution. This window, measured by  $t$ , is typically of order picosecond or less such that the  $\mathcal{A}_{mk}^l(t)$  do not appreciably change. The measured diffraction images are given by Eq. 18

$$\begin{aligned} \langle I(\mathbf{q}) \rangle_{\text{sep}}^{(2)}(t, \tau) = & \mathcal{I} \left( \sum_{\mu} |f_{\mu}(q)|^2 + \sum_{\mu, \nu: \mu \neq \nu} \text{Re} \left\{ f_{\mu}(q) f_{\nu}^*(q) \sum_l i^l 8\pi^2 \sqrt{4\pi(2l+1)} \sum_{m_1, m_2} (-1)^{m_1 - m_2} \right. \right. \\ & \left. \left. \times Y_l^{-m_2} \left( \theta_q^{(\text{lf})}, \phi_q^{(\text{lf})} \right) \tilde{\mathcal{A}}_{m_1 m_2}^l(n, n'; \tau) \langle \psi_{\text{el-vib}}^n(t) | j_l(q\Delta r_{\mu\nu}) Y_l^{-m_1} \left( \theta_{\mu\nu}^{(\text{mf})}, \phi_{\mu\nu}^{(\text{mf})} \right) | \psi_{\text{el-vib}}^n(t) \rangle \right\} \right) \end{aligned} \quad (18)$$

where  $n$  labels the vibronic states,  $|\psi_{\text{el-vib}}^n(t)\rangle$  is the vibronic wavefunction (assumed unknown),  $\tilde{\mathcal{A}}_{m_1 m_2}^l(n, n'; \tau)$  are the modified ADMs, and  $t$  is the arrival time of the probe after the second excitation pulse. These modified ADMs consider the angular momentum transfer by the photon for the excitation to the vibronic state. This only requires calculating the ground state transition dipole moment. One then follows the same analysis procedure outlined above for the ground state for all  $C_{lmk}(q, t)$  coefficients at each probe time  $t$ . In such an experiment, one should measure the ensemble anisotropy without the vibronic excitation pulse. This would provide the best fit ADMs via fits to pulse intensity and temperature. Supplementary Section IX further describes our separation of timescale approximation and provides the derivations for Eqs. 17

and 18, and describes the required molecular frame orientation angles when  $l \neq 0$ .

The isotropic method uses only the  $C_{000}(q, t)$  term similar to conventional analyses. The  $\mathcal{A}_{00}^0(t)$  is a constant which eliminates the need to simulate either the full ADMs or the full modified ADMs. This places all the time dependence into the molecular frame geometry term of Eq. 16. Thus, it can be applied to either single (Eq. 17) or double pulse (Eq. 18) modalities and relies on the Bayesian Inferencing and MHA mapping rather than anisotropy. One then performs the MHA for each  $C_{000}(q, t)$ . The  $C_{000}(q, t)$  term only implicitly depends on the pair-wise angles through  $\Delta r_{\mu\nu}$ . This is in contrast to the explicit pair-wise angle dependence in the higher order  $C_{lmk}(q)$  terms. Our statistical treatment likely provides adequate pair-wise angle resolution be-

cause we have more pair-wise distances than are required to uniquely specify a geometry.

When using a Raman inducing precursor pulse, one will likely use a combination of the isotropic and time separable methods. For fast dynamics one would use the time separable method for small windows shortly following the rotation time  $\tau$ . Longer lived dynamics can be retrieved by the isotropic method. When retrieving  $P(\Theta|C)$  in either case one initiates the MHA with the ground state  $\Theta^*$  parameters. For each subsequent time step one initiates MHA with the  $\Theta^*$  parameters from the previous time step.

Vibronic wavepackets bifurcate into multiple states, e.g. at conical intersections, causing  $P(\mathbf{r}, t|\Theta^*, C)$  to bifurcate as well. We account for these different states by

$$P(\mathbf{r}, t|\Theta^*, C) = \sum_i^{N_{\text{ex}}} c_i P(\mathbf{r}, \Theta_i^*, t|C) \quad (19)$$

where  $N_{\text{ex}}$  is the number of excited state distributions with appreciable population. Conical intersections will induce bifurcations that spawn a new distribution that adds to  $N_{\text{ex}}$ . In this way we consider this method to be fully data-driven since we can change our theoretical description ( $c_i$ ) based on data alone.

In the excited state,  $|\Psi(\mathbf{r}, t)|^2$  often takes on shapes that are poorly represented by normal distributions [41]. Nevertheless, the normal distribution acts as a second order improvement upon fitting with a single geometry [19, 20]. This improvement dampens the single geometry systematics shown in Fig. 8 and retrieves a quantifiable measurement of  $|\Psi(\mathbf{r}, t)|^2$  widths. This is particularly useful for vibronic wavepackets with appreciable width. One can better describe amorphous  $|\Psi(\mathbf{r}, t)|^2$  [42] by using more representative distributions, such as Hermite polynomials, for  $P(\mathbf{r}, t|\Theta^*, C)$ .

Thus far we have only considered diffraction consistent with the independent atom approximation and all the equations above have been derived under this approximation. Recently, however, diffraction beyond the independent atom approximation has been observed in both electron [43] and x-ray diffraction [44]. Under such conditions this method must be modified by either re-deriving the above equations to consider these effects or by accounting for this signal in the  $C_{lmk}(q)$  coefficients. For MeV electron diffraction, inelastic scattering is limited to the low  $q < 1 \text{ \AA}^{-1}$  region and can be easily removed from the  $C_{lmk}(q)$  coefficients. For x-rays, diffraction beyond the independent atom approximation contributes a constant offset after the initial signal turn-on that spans the entire  $q$  range. References [19, 44] observed a constant signal from the electron vacancy after exciting the molecule into a Rydberg state. Since this signal does not vary appreciably in time, it can safely be subtracted out before applying our method. Alternatively, one can alter  $P(\mathbf{r}, t|\Theta^*, C)$  to include this offset by adding a corresponding parameter to  $\Theta$ .

## V. CONCLUSION AND OUTLOOK

We have shown that our method can approximate  $|\Psi(\mathbf{r})|^2$  with  $P(\mathbf{r}|\Theta^*, C)$  for the ground states of  $\text{NO}_2$  and  $\text{N}_2\text{O}$ . In simulation, we retrieve  $\sim 100$  fm resolution for  $\text{NO}_2$ . From measured  $\text{N}_2\text{O}$  UED data, we retrieve  $\sim 4$  pm resolution despite a short  $q$  range of  $[3.5, 7.25] \text{ \AA}^{-1}$  and high SNR. This method returns the labeled pair-wise distances and the angles with  $\sim 100$  times better resolution than PDF-based methods. Furthermore, we can retrieve the unique molecular geometry more directly from the data. In spite of similar bond distances and atomic scattering amplitudes for  $\text{NO}_2$ , our method distinguishes bond distances from the  $C_{200}(q)$  coefficient alone. Adding a comparatively low SNR and a narrow  $q$  range of  $[3.5, 7.25] \text{ \AA}^{-1}$  to the UED data we still observed picometer resolution from the  $\text{N}_2\text{O}$  data and can even begin to resolve the  $\langle \text{N}^{\text{T}}\text{N}^{\text{C}} \rangle$  and  $\langle \text{N}^{\text{C}}\text{O} \rangle$  distances. These results are highly encouraging and illustrate the viability of our Bayesian Inferencing approach and inspires further expansion into excited states dynamics. The code repository [32] contains the algorithms used for this work and instructions on how to reproduce these results. It also contains instructions on how to run this analysis and templates for applying this method to new molecules.

This Bayesian Inferencing approach is best suited for gas-phase ultrafast diffraction instruments that have high SNR such as high repetition-rate free electron facilities, e.g. LCLS-II-HE. Resolution quickly improves with SNR considerably faster than if one increases  $q$  beyond  $\sim 8 \text{ \AA}^{-1}$ . Illustrated in our measurement of  $\text{N}_2\text{O}$  with a limited  $q$  range below  $8 \text{ \AA}^{-1}$ ,  $[3.5, 7.25] \text{ \AA}^{-1}$ , we demonstrate  $\sim 40$  times better resolution than the Fourier limit. Nevertheless, larger  $q$  ranges improve resolution for widths of  $|\Psi(\mathbf{r})|^2$  and diminish false correlations between  $\Theta$  parameters.

Our general method has the potential to become common-place for ultrafast gas-phase diffraction measurements due to its broad applicability and its independence from complex excited state simulations. In this work, we validated its use for standard pump probe setup. One can extend this method to excited state dynamics either with or without anisotropy. Our isotropic method is well suited for current pump probe setups that generally focus on the isotropic component. This method however greatly benefits from deterministic anisotropy that can either be induced by impulsive Raman or by the dipole moment selection from the excitation pulse. Beyond ultrafast gas-phase diffraction, one can apply this general framework to other classes of experiments, e.g. the previously mentioned photo-electron experiments [22–24, 27, 28]. This is done by deriving the molecular frame response (Eq. 2) and applying our Bayesian Inferencing approach.

Given its broad applicability, high resolution, amenability to various measurements, and independence from complex molecular dynamic simulations, our method has the potential to effectively turn ultrafast

gas-phase molecular diffraction into a discovery-oriented technique. This method can retrieve the unique molecular geometry of a general molecule to  $\sim 100$  fm resolution without relying on complex molecular simulations. Moreover, because our method is parameterized by  $\Theta$ , we have the opportunity to expand the scope of ultrafast gas-phase diffraction into previously inaccessible measurements. For instance, we demonstrated the use of this parameterization to measure the width of  $|\Psi(\mathbf{r}, t)|^2$ ; this width is important in the excited state where single geometries lose their meaning. This method unlocks our ability to study larger and more complex systems that are currently too difficult to simulate.

## VI. DATA AVAILABILITY

The UED  $\text{N}_2\text{O}$  data used in this analysis will be provided by the corresponding authors upon reasonable request. The simulated  $\text{NO}_2$  data,  $C_{lmk}(q)$ , can be calculated by the supplied analysis code in Ref. [32].

## VII. CODE AVAILABILITY

The code used in this analysis can be found in Ref. [32]. Here, one will find a detailed description of the code and how to run it in order to reproduce the  $\text{NO}_2$  results. This repository also includes templates for one to apply this algorithm to new molecules.

## ACKNOWLEDGMENTS

Use of the Linac Coherent Light Source (LCLS), SLAC National Accelerator Laboratory, is supported by the U.S. Department of Energy, Office of Science, Office of Basic Energy Sciences under Contract No. DE-AC02-76SF00515. The UED work was performed at SLAC MeVUED, which is supported in part by the DOE BES SUF Division Accelerator and Detector research and development program, the LCLS Facility, and SLAC under contract Nos. DE-AC02-05-CH11231 and DE-AC02-76SF00515. Markus Ilchen acknowledges funding by the Volkswagen foundation for a Peter-Paul-Ewald Fellowship. We thank Markus Gühr for his help in setting up the SLAC gas phase UED experiment. We thank Theodore Vecchione for his help operating the SLAC UED facility. We thank Gregory Stewart for creating Figs. 1 and S2.

- 
- [1] J. Charles Williamson, Jianming Cao, Hyotcherl Ihee, Hans Frey, and Ahmed H. Zewail, “Clocking transient chemical changes by ultrafast electron diffraction,” *Nature* **386**, 159–162 (1997).
- [2] John Ewbank, Walter Faust, Jing Luo, Jeffrey English, David Monts, David Paul, Qun Dou, and Lothar Schafer, “Instrumentation for gas electron diffraction employing a pulsed electron beam synchronous with photoexcitation,” *Review of Scientific Instruments* **63**, 3352 – 3358 (1992).
- [3] John Ewbank, Jing Luo, Jeffrey English, Ruifeng Liu, Walter Faust, and Lothar Schafer, “Time-resolved gas electron diffraction study of the 193-nm photolysis of 1,2-dichloroethenes,” *The Journal of Physical Chemistry* **97** (1993), 10.1021/j100136a016.
- [4] X. Shen, J. P. F. Nunes, J. Yang, R. K. Jobe, R. K. Li, Ming-Fu Lin, B. Moore, M. Niebuhr, S. P. Weathersby, T. J. A. Wolf, C. Yoneda, Markus Guehr, Martin Centurion, and X. J. Wang, “Femtosecond gas-phase mega-electron-volt ultrafast electron diffraction,” *Structural Dynamics* **6**, 054305 (2019), <https://doi.org/10.1063/1.5120864>.
- [5] Brian Stankus, Haiwang Yong, Jennifer Ruddock, Lingyu Ma, Andres Moreno Carrascosa, Nathan Goff, Sébastien Boutet, Xuan Xu, Nikola Zotev, Adam Kirrander, Michael P Minitti, and Peter M Weber, “Advances in ultrafast gas-phase x-ray scattering,” *Journal of Physics B: Atomic, Molecular and Optical Physics* **53**, 234004 (2020).
- [6] M. P. Minitti, J. M. Budarz, A. Kirrander, J. S. Robinson, D. Ratner, T. J. Lane, D. Zhu, J. M. Glowia, M. Kozina, H. T. Lemke, M. Sikorski, Y. Feng, S. Nelson, K. Saita, B. Stankus, T. Northey, J. B. Hastings, and P. M. Weber, “Imaging molecular motion: Femtosecond x-ray scattering of an electrocyclic chemical reaction,” *Phys. Rev. Lett.* **114**, 255501 (2015).
- [7] Matthew R. Ware, James M. Glowia, Adi Natan, James P. Cryan, and Philip H. Bucksbaum, “On the limits of observing motion in time-resolved x-ray scattering,” *Phil. Trans. R. Soc. A* (2019), 10.1098/rsta.2017.0477.
- [8] Matthew R. Ware, James M. Glowia, Noor Al-Sayyad, Jordan T. O’Neal, and Philip H. Bucksbaum, “Characterizing dissociative motion in time-resolved x-ray scattering from gas-phase diatomic molecules,” *Phys. Rev. A* **100**, 033413 (2019).
- [9] Philip H. Bucksbaum, Matthew R. Ware, Adi Natan, James P. Cryan, and James M. Glowia, “Characterizing multiphoton excitation using time-resolved x-ray scattering,” *Phys. Rev. X* **10**, 011065 (2020).
- [10] D. K. Saldin, V. L. Shneerson, D. Starodub, and J. C. H. Spence, “Reconstruction from a single diffraction pattern of azimuthally projected electron density of molecules aligned parallel to a single axis,” *Acta Crystallographica Section A* **66**, 32–37 (2010).
- [11] Dmitri Starodub, John C. H. Spence, and Dilano K. Saldin, “Reconstruction of the electron density of molecules with single-axis alignment,” in *Image Reconstruction from Incomplete Data VI*, Vol. 7800, edited by Philip J. Bones, Michael A. Fiddy, and Rick P. Millane, International Society for Optics and Photonics (SPIE, 2010) pp. 188 – 196.

- [12] P. J. Ho, D. Starodub, D. K. Saldin, V. L. Shneerson, A. Ourmazd, and R. Santra, “Molecular structure determination from x-ray scattering patterns of laser-aligned symmetric-top molecules,” *The Journal of Chemical Physics* **131**, 131101 (2009), <https://doi.org/10.1063/1.3245404>.
- [13] Veit Elser, “Three-dimensional structure from intensity correlations,” *New Journal of Physics* **13**, 123014 (2011).
- [14] H.-C. Poon, P. Schwander, M. Uddin, and D. K. Saldin, “Fiber diffraction without fibers,” *Phys. Rev. Lett.* **110**, 265505 (2013).
- [15] Peter Reckenthaeler, Martin Centurion, Werner Fuß, Sergei A. Trushin, Ferenc Krausz, and Ernst E. Fill, “Time-resolved electron diffraction from selectively aligned molecules,” *Phys. Rev. Lett.* **102**, 213001 (2009).
- [16] Stefan Pabst, Phay J. Ho, and Robin Santra, “Computational studies of x-ray scattering from three-dimensionally-aligned asymmetric-top molecules,” *Phys. Rev. A* **81**, 043425 (2010).
- [17] Jie Yang, Varun Makhija, Vinod Kumarappan, and Martin Centurion, “Reconstruction of three-dimensional molecular structure from diffraction of laser-aligned molecules,” *Structural Dynamics* **1**, 044101 (2014), <https://doi.org/10.1063/1.4889840>.
- [18] Christopher J. Hensley, Jie Yang, and Martin Centurion, “Imaging of isolated molecules with ultrafast electron pulses,” *Phys. Rev. Lett.* **109**, 133202 (2012).
- [19] Brian Stankus, Haiwang Yong, Nikola Zotev, Jennifer M. Ruddock, Darren Bellshaw, Thomas J. Lane, Mengning Liang, Sébastien Boutet, Sergio Carbajo, Joseph S. Robinson, Wenpeng Du, Nathan Goff, Yu Chang, Jason E. Koglin, Michael P. Minitti, Adam Kirrander, and Peter M. Weber, “Ultrafast x-ray scattering reveals vibrational coherence following rydberg excitation,” *Nature Chemistry* **11**, 716–721 (2019).
- [20] Adi Natan, “Real-space inversion and super-resolution of ultrafast scattering using natural scattering kernels,” (2021).
- [21] Adi Natan, Aviad Schori, Grace Owolabi, James P. Cryan, James M. Glowonia, and Philip H. Bucksbaum, “Resolving multiphoton processes with high-order anisotropy ultrafast x-ray scattering,” *Faraday Discuss.* **228**, 123–138 (2021).
- [22] Varun Makhija, Xiaoming Ren, Drue Gockel, Anh-Thu Le, and Vinod Kumarappan, “Orientation resolution through rotational coherence spectroscopy,” (2016), [arXiv:1611.06476 \[physics.atom-ph\]](https://arxiv.org/abs/1611.06476).
- [23] Claude Marceau, Varun Makhija, Dominique Platzter, A. Yu. Naumov, P. B. Corkum, Albert Stolow, D. M. Villeneuve, and Paul Hockett, “Molecular frame reconstruction using time-domain photoionization interferometry,” *Phys. Rev. Lett.* **119**, 083401 (2017).
- [24] Margaret Gregory, Paul Hockett, Albert Stolow, and Varun Makhija, “Towards molecular frame photoelectron angular distributions in polyatomic molecules from lab frame coherent rotational wavepacket evolution,” *Journal of Physics B: Atomic, Molecular and Optical Physics* **54**, 145601 (2021).
- [25] Péter Sándor, Adonay Sissay, François Mauger, Paul M. Abanador, Timothy T. Gorman, Timothy D. Scarborough, Mette B. Gaarde, Kenneth Lopata, Kenneth J. Schafer, and Robert R. Jones, “Angle dependence of strong-field single and double ionization of carbonyl sulfide,” *Phys. Rev. A* **98**, 043425 (2018).
- [26] Jochen Mikosch, Andrey E. Boguslavskiy, Iain Wilkinson, Michael Spanner, Serguei Patchkovskii, and Albert Stolow, “Channel- and angle-resolved above threshold ionization in the molecular frame,” *Phys. Rev. Lett.* **110**, 023004 (2013).
- [27] Péter Sándor, Adonay Sissay, François Mauger, Mark W. Gordon, T. T. Gorman, T. D. Scarborough, Mette B. Gaarde, Kenneth Lopata, K. J. Schafer, and R. R. Jones, “Angle-dependent strong-field ionization of halomethanes,” *The Journal of Chemical Physics* **151**, 194308 (2019), <https://doi.org/10.1063/1.5121711>.
- [28] Péter Sándor, Adonay Sissay, François Mauger, Paul M. Abanador, Timothy T. Gorman, Timothy D. Scarborough, Mette B. Gaarde, Kenneth Lopata, Kenneth J. Schafer, and Robert R. Jones, “Angle dependence of strong-field single and double ionization of carbonyl sulfide,” *Phys. Rev. A* **98**, 043425 (2018).
- [29] Albert Stolow and Jonathan G. Underwood, “Time-resolved photoelectron spectroscopy of nonadiabatic dynamics in polyatomic molecules,” in *Advances in Chemical Physics* (John Wiley & Sons, Ltd, 2008) Chap. 6, pp. 497–584, <https://onlinelibrary.wiley.com/doi/pdf/10.1002/9780470259498.ch6>.
- [30] Jonathan G. Underwood and Katharine L. Reid, “Time-resolved photoelectron angular distributions as a probe of intramolecular dynamics: Connecting the molecular frame and the laboratory frame,” *The Journal of Chemical Physics* **113**, 1067–1074 (2000), <https://doi.org/10.1063/1.481918>.
- [31] G.E.P. Box and G.C. Tiao, *Bayesian Inference in Statistical Analysis*, Wiley Classics Library (Wiley, 2011).
- [32] github, “Bigr github repository,” (2022).
- [33] Paul Hockett, “General phenomenology of ionization from aligned molecular ensembles,” *New Journal of Physics* **17**, 023069 (2015).
- [34] Daniel Foreman-Mackey, David W. Hogg, Dustin Lang, and Jonathan Goodman, “emcee: The MCMC hammer,” *Publications of the Astronomical Society of the Pacific* **125**, 306–312 (2013).
- [35] Gerhard Herzberg, *Electronic Spectra and electronic structure of Polyatomic Molecules* (Nostrand, 1966).
- [36] W. K. Hastings, “Monte Carlo sampling methods using Markov chains and their applications,” *Biometrika* **57**, 97–109 (1970), <https://academic.oup.com/biomet/article-pdf/57/1/97/23940249/57-1-97.pdf>.
- [37] T. J. A. Wolf, D. M. Sanchez, J. Yang, R. M. Parrish, J. P. F. Nunes, M. Centurion, R. Coffee, J. P. Cryan, M. Gühr, K. Hegazy, A. Kirrander, R. K. Li, J. Ruddock, X. Shen, T. Vecchione, S. P. Weathersby, P. M. Weber, K. Wilkin, H. Yong, Q. Zheng, X. J. Wang, M. P. Minitti, and T. J. Martínez, “The photochemical ring-opening of 1,3-cyclohexadiene imaged by ultrafast electron diffraction,” *Nature Chemistry* **11**, 504–509 (2019).
- [38] J. Spencer Baskin and Ahmed H. Zewail, “Oriented ensembles in ultrafast electron diffraction,” *ChemPhysChem* **7**, 1562–1574 (2006), <https://chemistry-europe.onlinelibrary.wiley.com/doi/pdf/10.1002/cphc.200600133>.
- [39] Robert Parrish and Todd Martinez, “Ab initio computation of rotationally-averaged pump-probe x-ray and electron diffraction signals,” *Journal of Chemical Theory and Computation* **15** (2019), [10.1021/acs.jctc.8b01051](https://doi.org/10.1021/acs.jctc.8b01051).



- [40] Lingyu Ma, Haiwang Yong, Joseph D. Geiser, Andrés Moreno Carrascosa, Nathan Goff, and Peter M. Weber, “Ultrafast x-ray and electron scattering of free molecules: A comparative evaluation,” *Structural Dynamics* **7**, 034102 (2020), <https://doi.org/10.1063/4.0000010>.
- [41] Varun Makhija, Andrey E. Boguslavskiy, Ruaridh Forbes, Kevin Veyrinas, Iain Wilkinson, Rune Lausten, Michael S. Schuurman, Edward R. Grant, and Albert Stolow, “A quantum molecular movie: polyad predissociation dynamics in the vuv excited  $3p\sigma 2\sigma u$  state of  $\text{NO}_2$ ,” *Faraday Discuss.* **228**, 191–225 (2021).
- [42] Peter M. Felker and Ahmed H. Zewail, “Direct observation of nonchaotic multilevel vibrational energy flow in isolated polyatomic molecules,” *Phys. Rev. Lett.* **53**, 501–504 (1984).
- [43] Jie Yang, Xiaolei Zhu, J. Pedro F. Nunes, Jimmy K. Yu, Robert M. Parrish, Thomas J. A. Wolf, Martin Centurion, Markus Gühr, Renkai Li, Yusong Liu, Bryan Moore, Mario Niebuhr, Suji Park, Xiaozhe Shen, Stephen Weathersby, Thomas Weinacht, Todd J. Martinez, and Xijie Wang, “Simultaneous observation of nuclear and electronic dynamics by ultrafast electron diffraction,” *Science* **368**, 885–889 (2020), <https://www.science.org/doi/pdf/10.1126/science.abb2235>.
- [44] Haiwang Yong, Nikola Zotev, Jennifer M. Ruddock, Brian Stankus, Mats Simmermacher, Andrés Moreno Carrascosa, Wenpeng Du, Nathan Goff, Yu Chang, Darren Bellshaw, Mengning Liang, Sergio Carbajo, Jason E. Koglin, Joseph S. Robinson, Sébastien Boutet, Michael P. Minitti, Adam Kirrander, and Peter M. Weber, “Observation of the molecular response to light upon photoexcitation,” *Nature Communications* **11**, 2157 (2020).
- [45] Richard N. Zare, *Angular Momentum: Understanding Spatial Aspects in Chemistry and Physics* (Wiley-Interscience, 1991).
- [46] Mikael D Poulsen, Emmanuel Peronne, Henrik Stapelfeldt, Christer Z Bisgaard, Simon S Viftrup, Edward Hamilton, and Tamar Seideman, “Nonadiabatic alignment of asymmetric top molecules: Rotational revivals,” *The Journal of chemical physics* **121**, 783–791 (2004).
- [47] Jonathan G Underwood, Benjamin J Sussman, and Albert Stolow, “Field-free three dimensional molecular axis alignment,” *Physical review letters* **94**, 143002 (2005).
- [48] A Rouzée, S Guérin, Vincent Boudon, B Lavorel, and O Faucher, “Field-free one-dimensional alignment of ethylene molecule,” *Physical Review A* **73**, 033418 (2006).
- [49] Norio Takemoto and Kaoru Yamanouchi, “Fixing chiral molecules in space by intense two-color phase-locked laser fields,” *Chemical Physics Letters* **451**, 1–7 (2008).
- [50] Yasuhiro Ohshima and Hirokazu Hasegawa, “Coherent rotational excitation by intense nonresonant laser fields,” *International Reviews in Physical Chemistry* **29**, 619–663 (2010).
- [51] Stefan Pabst, Phay J Ho, and Robin Santra, “Computational studies of x-ray scattering from three-dimensionally-aligned asymmetric-top molecules,” *Physical Review A* **81**, 043425 (2010).
- [52] Varun Makhija, Xiaoming Ren, and Vinod Kumarappan, “Metric for three-dimensional alignment of molecules,” *Physical Review A* **85**, 033425 (2012).
- [53] Christiane P Koch, Mikhail Lemeshko, and Dominique Sugny, “Quantum control of molecular rotation,” *Reviews of Modern Physics* **91**, 035005 (2019).
- [54] Kang Lin, Ilya Tutunnikov, Junyang Ma, Junjie Qiang, Lianrong Zhou, Olivier Faucher, Yehiam Prior, Ilya Sh Averbukh, and Jian Wu, “Spatiotemporal rotational dynamics of laser-driven molecules,” *Advanced Photonics* **2**, 024002 (2020).
- [55] A. Rouzée, S. Guérin, O. Faucher, and B. Lavorel, “Field-free molecular alignment of asymmetric top molecules using elliptically polarized laser pulses,” *Phys. Rev. A* **77**, 043412 (2008).
- [56] A. Rouzée, S. Guérin, V. Boudon, B. Lavorel, and O. Faucher, “Field-free one-dimensional alignment of ethylene molecule,” *Phys. Rev. A* **73**, 033418 (2006).
- [57] Edward Hamilton, Tamar Seideman, Tine Ejdrup, Mikael D. Poulsen, Christer Z. Bisgaard, Simon S. Viftrup, and Henrik Stapelfeldt, “Alignment of symmetric top molecules by short laser pulses,” *Phys. Rev. A* **72**, 043402 (2005).
- [58] Lotte Holmegaard, Simon S. Viftrup, Vinod Kumarappan, Christer Z. Bisgaard, Henrik Stapelfeldt, Edward Hamilton, and Tamar Seideman, “Control of rotational wave-packet dynamics in asymmetric top molecules,” *Phys. Rev. A* **75**, 051403 (2007).
- [59] Xiaoming Ren, Varun Makhija, and Vinod Kumarappan, “Measurement of field-free alignment of jet-cooled molecules by nonresonant femtosecond degenerate four-wave mixing,” *Phys. Rev. A* **85**, 033405 (2012).
- [60] Tamar Seideman, “On the dynamics of rotationally broad, spatially aligned wave packets,” *The Journal of Chemical Physics* **115**, 5965–5973 (2001), <https://doi.org/10.1063/1.1400131>.
- [61] Henrik Stapelfeldt and Tamar Seideman, “Colloquium: Aligning molecules with strong laser pulses,” *Rev. Mod. Phys.* **75**, 543–557 (2003).
- [62] Han Liu, John Lafferty, and Larry Wasserman, “Sparse nonparametric density estimation in high dimensions using the rodeo,” in *Proceedings of the Eleventh International Conference on Artificial Intelligence and Statistics*, *Proceedings of Machine Learning Research*, Vol. 2, edited by Marina Meila and Xiaotong Shen (PMLR, San Juan, Puerto Rico, 2007) pp. 283–290.
- [63] P. J. Cumpson and M. P. Seah, “Random uncertainties in aes and xps: I: Uncertainties in peak energies, intensities and areas derived from peak synthesis,” *Surface and Interface Analysis* **18**, 345–360 (1992).

## Supplemental Information

### VIII. CALCULATING THE AXIS DISTRIBUTION MOMENTS

We first address how to calculate the axis distribution moments (ADMs) for a simple linear symmetric top, like  $\text{N}_2\text{O}$ . A linear rotor has two unique principal components of inertia, where the single unique moment is much smaller than the other two equal components. In the rigid rotor approximation,

$$\langle jm|\theta, \phi\rangle = Y_j^m(\theta, \phi) \quad (\text{S1})$$

$$E_{jm} = Bj(j+1) \quad (\text{S2})$$

$$B = \frac{\hbar^2}{2I} \quad (\text{S3})$$

where  $B$  is the rotational constant for  $\text{N}_2\text{O}$  and  $I$  is the moment of inertia. Before the alignment pulse ( $t < 0$ ) each molecule is in a single rotational eigenstate  $|j, m\rangle$ . The alignment pulse launches a rotational wavepacket by introducing a rotational coherence between eigenstates

$$|\psi^{(i)}(t)\rangle = \sum_{j,m} c_{j_i m_i j m}(t) |j, m\rangle \quad (\text{S4})$$

where  $j_i$  and  $m_i$  label the initial ( $t < 0$ ) rotational eigenstate for a single molecule. Our ensemble, however, is made of many molecules in different rotational eigenstates that are populated according to the Boltzmann Distribution. This thermal ensemble is represented by the density matrix

$$\rho(t) = \sum_i p_i |\psi^{(i)}(t)\rangle \langle \psi^{(i)}(t)| \quad (\text{S5})$$

$$p_i = \frac{\exp\{-E_{j_i m_i}/(k_b T)\}}{Z} \quad (\text{S6})$$

where we sum over the initial  $|j_i, m_i\rangle$  states,  $Z$  is the partition function,  $k_b$  is the Boltzmann, and  $T$  is the temperature.

The ADMs is a sparse basis that encodes the angular relationship between the lab frame and the distribution of molecular frame. More specifically, the ADMs ( $\mathcal{A}_m^l(t)$ ) are the projection of the ensemble anisotropy (distribution of molecular frames with respect to the lab frame) onto the Spherical Harmonics basis.

$$P(\theta, \phi, t) = \sum_{l,m} \mathcal{A}_m^l(t) Y_l^m(\theta, \phi) = |\langle \psi|\theta, \phi\rangle|^2 \quad (\text{S7})$$

Here  $\theta$  and  $\phi$  are the polar and azimuthal angles, respectively, measured from the lab frame to the molecular frame and  $P(\theta, \phi, t)$  is the probability of finding a molecule oriented at these angles. The molecule's smallest moment of inertia defines the molecular frame  $\hat{\mathbf{z}}$  axis, along the rotor. The laser polarization defines the lab frame  $z$  axis ( $\hat{\mathbf{z}}$ ). We calculate the ADMs by

$$\begin{aligned} \mathcal{A}_m^l(t) &= \frac{2l+1}{4\pi} \text{Tr}(\rho Y_l^m) \\ &= \frac{2l+1}{4\pi} \sum_i p_i \sum_{j_1, m_1} \sum_{j_2, m_2} c_{j_i m_i j_1 m_1}^*(t) c_{j_i m_i j_2 m_2}(t) \\ &\quad \times \int Y_{j_1}^{*m_1} Y_l^m Y_{j_2}^{m_2} \sin\theta d\theta d\phi \\ &= \frac{2l+1}{4\pi} \sum_i p_i \sum_{j_1, m_1} \sum_{j_2, m_2} c_{j_i m_i j_1 m_1}^*(t) c_{j_i m_i j_2 m_2}(t) \\ &\quad \times \sqrt{\frac{(2j_1+1)(2l+1)(2j_2+1)}{4\pi}} \\ &\quad \times \begin{pmatrix} j_1 & l & j_2 \\ 0 & 0 & 0 \end{pmatrix} \begin{pmatrix} j_1 & l & j_2 \\ -m_1 & m & m_2 \end{pmatrix}. \end{aligned} \quad (\text{S8})$$

Asymmetric rigid rotors have three unique principal axes with  $A \neq B \neq C$ , such that  $I_A < I_B < I_C$ . As a result, they have a fundamentally different energy level structure. In general, the energy eigenvalues may be determined analytically for each  $J$  using the  $D_2$  symmetry group of the rigid rotor Hamiltonian. This renders the Hamiltonian matrix in the  $|jmk\rangle$  symmetric top basis block diagonal [45]. Here  $k$  is the angular momentum quantum number corresponding to the projection of the angular momentum on the molecular frame  $\hat{\mathbf{z}}$ . Writing the eigenstates in this basis yields,

$$|jm\tau\rangle = \sum_k C_{jmk} |jmk\rangle. \quad (\text{S9})$$

The asymmetric top eigenstates  $|jm\tau\rangle$  each correspond to an energy eigenvalue  $E_{jm\tau}$ , and the spacing between eigenstates determines the field-free evolution of the rotational wavepacket excited by the alignment pulse from an initial state rotational state ( $i$ ),

$$|\psi^{(i)}(t)\rangle = \sum_{jm\tau} c_{jm\tau} \exp\left\{\frac{-iE_{jm\tau}t}{\hbar}\right\} |jm\tau\rangle. \quad (\text{S10})$$

The coefficients  $c_{jm\tau}$  are determined by solving the TDSE for the asymmetric rigid rotor in a non-resonant time dependent electric field. The field-matter interaction is typically mediated by the molecular polarizability, resulting in a series of Raman Transitions. Such a calculation has been detailed by several authors [46–54], so we do not discuss it here. The density matrix  $\rho_{jm\tau}^{j'm'\tau'}(t)$  can then be determined as discussed above for the linear molecule. Finally, the ADMs can be calculated from the density matrix transformed into the  $|jmk\rangle$  basis as follows,

$$\begin{aligned} \mathcal{A}_{QS}^K(t) &= \frac{2K+1}{8\pi^2} \text{Tr}(\rho D_{QS}^K) \\ &= \frac{2K+1}{8\pi^2} \sum_{j,m,k} \sum_{j',m',k'} \rho_{jmk}^{j'm'k'}(t) \\ &\quad \times \sqrt{(2j+1)(2j'+1)} (-1)^{m-k} \\ &\quad \times \begin{pmatrix} j & j' & K \\ -m & m' & Q \end{pmatrix} \begin{pmatrix} j & j' & K \\ -k & k' & S \end{pmatrix}. \end{aligned} \quad (\text{S11})$$

## IX. ANISOTROPY DERIVATION

We now show how deterministic anisotropy allows one to access molecular frame geometric information by coupling the lab and molecular frame. Using the Independent Atom model (IAM), the x-ray, or electron, diffraction intensity from a single molecule is given by

$$\begin{aligned} I(\mathbf{q}) &= \mathcal{I} \left( \sum_{\mu} |f_{\mu}(q)|^2 \right. \\ &\quad \left. + \sum_{\mu,\nu:\mu \neq \nu} \text{Re}\{f_{\mu}(q)f_{\nu}^*(q) \exp(i\mathbf{q} \cdot (\mathbf{r}_{\mu} - \mathbf{r}_{\nu}))\} \right) \end{aligned} \quad (\text{S12})$$

$$\mathcal{I} = \begin{cases} I_0 & : \text{x-ray diffraction} \\ \frac{I_0}{R^2} & : \text{electron diffraction} \end{cases} \quad (\text{S13})$$

where  $\mathcal{I}$  is a scaling coefficient,  $I_0$  is the initial intensity of the probe,  $R$  is the distance between the sample and where the electron was detected,  $\mathbf{r}_{\mu}$  is the position of the  $\mu^{\text{th}}$  atom, and  $f_{\mu}(q)$  is either the electron scattering amplitude or x-ray form factor of the  $\mu^{\text{th}}$  atom. Here  $\mathbf{q}$  is the momentum transfer imparted on either the electron or x-ray after scattering from the molecule. In the case of x-ray scattering, we assume one has already removed the anisotropic effects from Thomson Scattering. The difference in the scattered x-ray and electron wave functions accounts for the  $R^{-2}$  factor in  $\mathcal{I}$ . The first term  $\left(\sum_{\mu} |f_{\mu}(q)|^2\right)$  is independent of the molecule's geometry and is referred to as the atomic scattering contribution. The second term depends on the pair-wise distances of atoms and is known as the molecular diffraction.

Our objective is to represent the lab frame diffraction pattern, parameterized by the momentum transfer  $q = |\mathbf{q}|$  and the detector's azimuthal angle  $\theta^{(\text{d})}$ , in terms of the molecular frame pair-wise distances and angles  $\Delta\mathbf{r}_{\mu\nu} = \mathbf{r}_{\mu} - \mathbf{r}_{\nu} =$

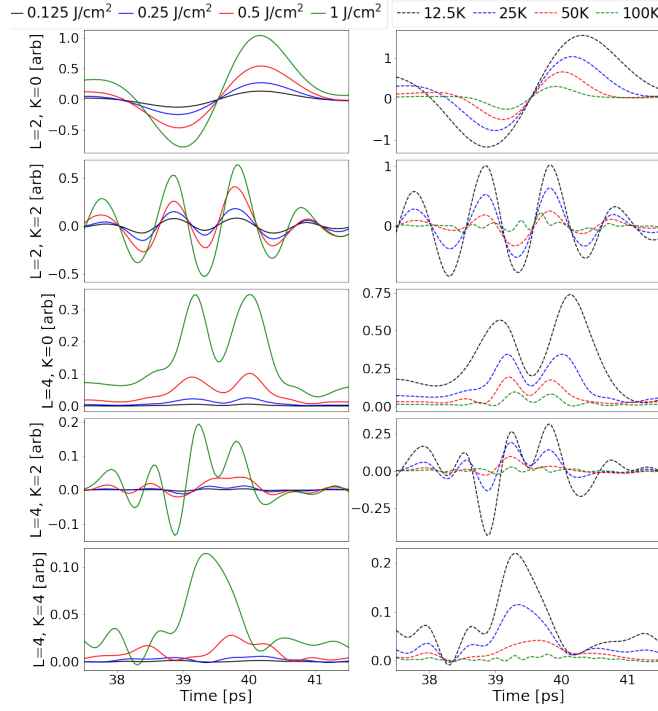


FIG. S1. The axis distribution moments vary as a function of pump fluence and ensemble temperature. The left column varies the pump fluence with a constant temperature of 25 K. The right column varies the temperature with a constant fluence of 1 J/cm<sup>2</sup>.

$[\Delta r_{\mu\nu}, \theta_{\mu\nu}^{(\text{mf})}, \phi_{\mu\nu}^{(\text{mf})}]$ . This derivation focuses on a single  $(\mu, \nu)$  pair from the molecular diffraction sum in Eq. S12, where the  $\nu^{\text{th}}$  atom defines the origin as we rotate between the lab and various body reference frames. Figure S2 illustrates these various frames serving as an intuitive guide, with the  $\nu^{\text{th}}$  atom translated to the origin. Such translations are allowed since they cancel in the  $\Delta \mathbf{r}_{\mu\nu}$  term. For our rotations, we use the conventions in Ref. [45]. Unless otherwise stated,  $\theta$  and  $\phi$  represent the polar and azimuthal angles, respectively, in a spherical coordinate system.

We define the pair-wise frame (pf) such that  $\hat{\mathbf{z}}^{(\text{pf})} = \Delta \hat{\mathbf{r}}_{\mu\nu}$ , again emphasizing we translate the molecule such that the  $\nu^{\text{th}}$  atom is at the origin. The pair-wise frame is shown in Fig. S2c. The exponential term in Eq. S12 is rewritten using the partial wave expansion

$$\exp(i\mathbf{q} \cdot \Delta \mathbf{r}_{\mu\nu}) = \sum_l i^l (2l+1) j_l(q\Delta r_{\mu\nu}) \times Y_l^0(\theta_q^{(\text{pf})}, \phi_q^{(\text{pf})}) \quad (\text{S14})$$

Here,  $j_l(q\Delta r_{\mu\nu})$  are the spherical Bessel functions of the first kind,  $Y_l^m(\theta_q^{(\text{pf})}, \phi_q^{(\text{pf})})$  are spherical harmonics, and  $(\theta_q^{(\text{pf})}, \phi_q^{(\text{pf})})$  are the polar and azimuthal angles that define  $\mathbf{q}$  in the pair-wise frame. In the above equation, we extract the labelled pair-wise distance  $\Delta r_{\mu\nu}$ : one of our parameters of interest.

The molecular frame (mf) is defined by the molecule's principal moments of inertia, here the  $\hat{\mathbf{z}}^{(\text{mf})}$ ,  $\hat{\mathbf{y}}^{(\text{mf})}$ , and  $\hat{\mathbf{x}}^{(\text{mf})}$  axes correspond to the moments with increasing rotational inertia. Figure S2b shows the molecular frame for NO<sub>2</sub> with the nitrogen translated to the origin. We passively rotate from the pair-wise frame into the molecular frame, shown in Fig. S2 as green and orange, respectively.

$$\exp(i\mathbf{q} \cdot \Delta \mathbf{r}_{\mu\nu}) = \sum_l i^l (2l+1) j_l(q\Delta r_{\mu\nu}) \sum_{m_1} [D_{m_1 0}^l(\phi_{\mu\nu}^{(\text{mf})}, \theta_{\mu\nu}^{(\text{mf})}, 0)]^\dagger Y_l^{m_1}(\theta_q^{(\text{mf})}, \phi_q^{(\text{mf})}) \quad (\text{S15})$$

$$= \sum_l i^l \sqrt{4\pi(2l+1)} j_l(q\Delta r_{\mu\nu}) \sum_{m_1} Y_l^{m_1}(\theta_{\mu\nu}^{(\text{mf})}, \phi_{\mu\nu}^{(\text{mf})}) Y_l^{m_1}(\theta_q^{(\text{mf})}, \phi_q^{(\text{mf})}) \quad (\text{S16})$$

The molecular frame angles  $\phi_{\mu\nu}^{(\text{mf})}$  and  $\theta_{\mu\nu}^{(\text{mf})}$  define the orientation of  $\Delta \hat{\mathbf{r}}_{\mu\nu}$ , where  $\chi_{\mu\nu}^{(\text{mf})} = 0$  since  $\Delta \mathbf{r}_{\mu\nu}$  is a vector. We stress the importance of these molecular frame geometry angles  $(\theta_{\mu\nu}^{(\text{mf})}, \phi_{\mu\nu}^{(\text{mf})})$  as they are needed, along with  $\Delta r_{\mu\nu}$  to

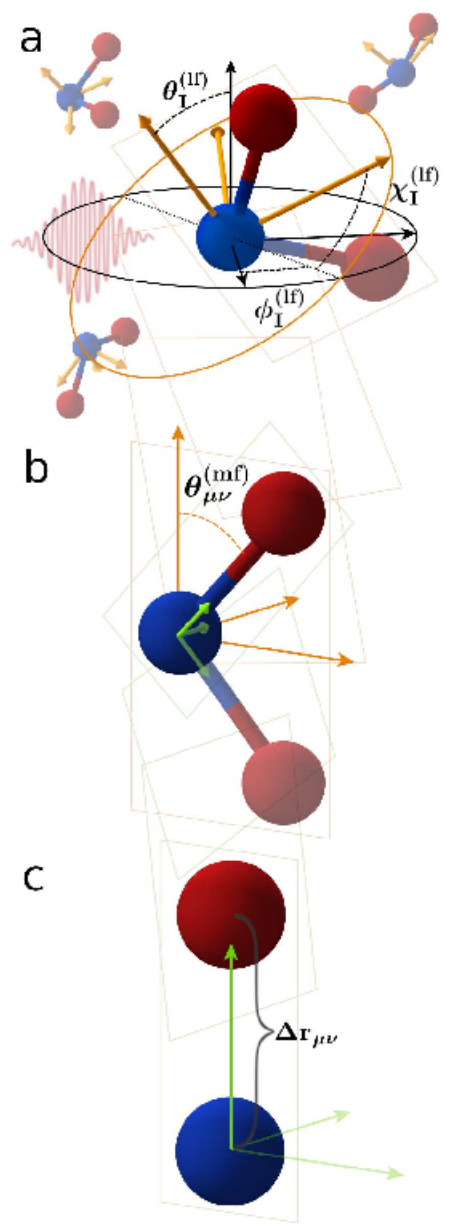


FIG. S2. To relate the ensemble anisotropy to the lab frame observable, we must rotate between the pair-wise, molecular, and lab frames. Using NO<sub>2</sub>, we illustrate these three reference frames. Here we highlight a single NO bond and moved the oxygen to the origin, as is done in the derivation. On the left is the lab frame (lf) where the laser polarization and the direction of the probe beam define  $\hat{z}^{(lf)}$  and  $\hat{y}^{(lf)}$  respectively. In the molecular frame (mf), shown in the center, is defined by the molecule's principal moments of inertia where the molecular A, B, and C axis define  $\hat{z}^{(mf)}$ ,  $\hat{y}^{(mf)}$ , and  $\hat{x}^{(mf)}$ . Each pair of two atoms has its own pair-wise frame (pf) where  $\hat{z}^{(pf)}$  is defined by  $\mathbf{r}_{\mu\nu}$ .

define a unique molecular geometry. With PDF methods alone, one only has access to unlabeled  $\Delta r_{\mu\nu}$  and generally cannot define a unique molecular geometry. These molecular frame angles are the last two geometric parameters of interest.

To connect our molecular frame calculation to our measurement, we passively rotate into the lab frame (lf). The lab frame  $\hat{z}^{(lf)}$  is defined as the polarization of the alignment laser ( $\hat{\epsilon}$ ), and  $\hat{y}^{(lf)}$  is along the probe path and normal

to the detector.

$$\begin{aligned} \exp(i\mathbf{q} \cdot \Delta\mathbf{r}_{\mu\nu}) &= \sum_l i^l \sqrt{4\pi(2l+1)} j_l(q\Delta r_{\mu\nu}) \\ &\times \sum_{m_1 m_2} \left[ D_{m_2 m_1}^l \left( \phi_1^{(\text{lf})}, \theta_1^{(\text{lf})}, \chi_1^{(\text{lf})} \right) \right]^\dagger Y_l^{m_1} \left( \theta_{\mu\nu}^{(\text{mf})}, \phi_{\mu\nu}^{(\text{mf})} \right) Y_l^{m_2} \left( \theta_q^{(\text{lf})}, \phi_q^{(\text{lf})} \right) \end{aligned} \quad (\text{S17})$$

$$\begin{aligned} &= \sum_l i^l \sqrt{4\pi(2l+1)} j_l(q\Delta r_{\mu\nu}) \\ &\times \sum_{m_1 m_2} (-1)^{m_2 - m_1} D_{-m_2 - m_1}^l \left( \phi_1^{(\text{lf})}, \theta_1^{(\text{lf})}, \chi_1^{(\text{lf})} \right) Y_l^{m_1} \left( \theta_{\mu\nu}^{(\text{mf})}, \phi_{\mu\nu}^{(\text{mf})} \right) Y_l^{m_2} \left( \theta_q^{(\text{lf})}, \phi_q^{(\text{lf})} \right) \end{aligned} \quad (\text{S18})$$

Here  $\phi_1^{(\text{lf})}$ ,  $\theta_1^{(\text{lf})}$ , and  $\chi_1^{(\text{lf})}$  are the conventional Euler angles in the lab frame that describe the orientation of the molecule's principal moments of inertia with respect to the lab frame. Finally, without loss of generality, we take  $m_1 \rightarrow -m_1$  and  $m_2 \rightarrow -m_2$ , and combine Eqs. S18 and S12 to get the following general expression for the diffraction intensity of a single molecule

$$\begin{aligned} I(\mathbf{q}) &= \mathcal{I} \left( \sum_\mu |f_\mu(q)|^2 + \sum_{\mu, \nu: \mu \neq \nu} \text{Re} \left\{ f_\mu(q) f_\nu^*(q) \sum_l i^l 8\pi^2 \sqrt{4\pi(2l+1)} j_l(q\Delta r_{\mu\nu}) \right. \right. \\ &\times \left. \left. \sum_{m_1, m_2} (-1)^{m_1 - m_2} D_{m_2, m_1}^l \left( \phi_1^{(\text{lf})}, \theta_1^{(\text{lf})}, \chi_1^{(\text{lf})} \right) Y_l^{-m_1} \left( \theta_{\mu\nu}^{(\text{mf})}, \phi_{\mu\nu}^{(\text{mf})} \right) Y_l^{-m_2} \left( \theta_q^{(\text{lf})}, \phi_q^{(\text{lf})} \right) \right\} \right). \end{aligned} \quad (\text{S19})$$

We have now expressed the measurable diffraction (Eq. S12) in terms of the pair-wise molecular frame distances and angles, as well as the lab frame angles  $(\theta_q^{(\text{lf})}, \phi_q^{(\text{lf})})$  that define  $\mathbf{q}$ .

In gas-phase diffraction experiments one measures an ensemble of molecules at different orientations, alignments, and possibly differing geometries depending on the populated rovibronic states. One samples that ensemble at a variety of times relative to the evolving ensemble anisotropy, revealing the following observable,

$$\begin{aligned} \langle I(\mathbf{q}) \rangle(t) &= \mathcal{I} \left( \sum_\mu |f_\mu(q)|^2 + \sum_{\mu, \nu: \mu \neq \nu} \text{Re} \left\{ f_\mu(q) f_\nu^*(q) \sum_l i^l 8\pi^2 \sqrt{4\pi(2l+1)} \right. \right. \\ &\times \left. \left. \sum_{m_1, m_2} (-1)^{m_1 - m_2} Y_l^{-m_2} \left( \theta_q^{(\text{lf})}, \phi_q^{(\text{lf})} \right) \langle \Psi(t) \left| D_{m_2 m_1}^l \left( \phi_1^{(\text{lf})}, \theta_1^{(\text{lf})}, \chi_1^{(\text{lf})} \right) j_l(q\Delta r_{\mu\nu}) Y_l^{-m_1} \left( \theta_{\mu\nu}^{(\text{mf})}, \phi_{\mu\nu}^{(\text{mf})} \right) \right| \Psi(t) \right\rangle \right) \end{aligned} \quad (\text{S20})$$

where  $\Psi(t)$  is the molecular ensemble wavefunction that describes both the rotational and vibronic dynamics of the system. This is the general expression for the scattered intensity from the entire molecular ensemble in lab frame coordinates, with the explicit dependence on the molecular frame atomic pair-wise coordinates.

When considering typical experimental setups, we must employ common symmetries and relate the calculated lab frame diffraction signal to the 2d detector, parameterized by  $q = |\mathbf{q}|$  and  $\theta^{(\text{d})}$ . The detector lies in the x-z plane of the lab frame where  $\theta^{(\text{d})}$  is with respect to  $\hat{\mathbf{z}}^{(\text{lf})}$ .

$$\alpha = 2 \sin^{-1} \left( \frac{q\lambda}{4\pi} \right) + \frac{\pi}{2} \quad (\text{S21})$$

$$\theta_q^{(\text{lf})} = \cos^{-1} \left( \sin(\alpha) \cos(\theta^{(\text{d})}) \right) \quad (\text{S22})$$

$$\phi_q^{(\text{lf})} = \tan^{-1} \left( \frac{\cos(\alpha)}{\sin(\alpha) \sin(\theta^{(\text{d})})} \right) \quad (\text{S23})$$

Where  $\lambda$  is either the deBroglie wavelength of the electron probe, or the x-ray wavelength, and  $\alpha$  is the scattering angle rotated by  $\pi/2$ . For the 3.7 MeV electron probe at the SLAC Ultrafast Electron Diffraction facility [4]  $\lambda = 3.0 \times 10^{-3} \text{\AA}$  and the above relations simplify to

$$\begin{aligned} \alpha &\approx \frac{\pi}{2} \\ \theta_q^{(\text{lf})} &\approx \theta^{(\text{d})} \\ \phi_q^{(\text{lf})} &\approx 0 \end{aligned}$$

For x-ray diffraction at  $\sim 10$  keV this expression does not simplify due to larger x-ray scattering angles. Often, one uses a linearly polarized alignment pump pulse which induces cylindrical symmetry in the ensemble rotation wave packet, which results in  $m_2 = 0$ . Equation S19 is derived for an asymmetric top, for a symmetric top there is symmetry about the molecular frame  $z$  axis, which sets  $m_1 = 0$ .

It is difficult to extract  $\Delta \mathbf{r}_{\mu\nu}$  from Eq. S20 in its current form since rovibronic coupling may affect the time dependent anisotropy. With rovibronic coupling, to calculate the ensemble anisotropy we may be required to simulate the excited state with the complex excited state simulations we do not want to rely on. This coupling, therefore, may render the anisotropy calculation too difficult. Instead, we consider two methods to separate the ensemble anisotropy and the molecular frame pair-wise terms, where we assume the molecular geometry is rigid over the measurement period. We decompose the ensemble anisotropy into the Axis Distribution Moments (ADMs) by projecting the ensemble of molecular frame orientations, with respect to the lab frame (Fig. S2a), onto the Wigner D matrices,

$$\mathcal{A}_{mk}^l(t) = \frac{2l+1}{8\pi^2} \left\langle \Psi(t) \left| D_{mk}^l \left( \phi_{\text{I}}^{(\text{lf})}, \theta_{\text{I}}^{(\text{lf})}, \chi_{\text{I}}^{(\text{lf})} \right) \right| \Psi(t) \right\rangle \quad (\text{S24})$$

$$\mathcal{A}_{mk}^l(t)|_{\text{rigid}} = \frac{2l+1}{8\pi^2} \left\langle \Psi_{\text{rigid}}(t) \left| D_{mk}^l \left( \phi_{\text{I}}^{(\text{lf})}, \theta_{\text{I}}^{(\text{lf})}, \chi_{\text{I}}^{(\text{lf})} \right) \right| \Psi_{\text{rigid}}(t) \right\rangle. \quad (\text{S25})$$

Simulations of the rotational wavefunction for rigid symmetric and rigid asymmetric tops [55–61] produce good agreement with measured alignment signatures. To extract  $\Delta \mathbf{r}_{\mu\nu}$  from Eq. S20 we consider two approximations: the typical rigid rotor approximation and a separation of time scales.

### A. Rigid Rotor Approximation

We first consider the rigid rotor approximation, which assumes the molecular geometry is constant throughout the rotational dynamics. This allows us to take the expectation value of the molecular geometry, the molecular frame terms, with respect to the ground state structure at  $t = 0$ . We may also calculate the ADMs with respect to the ground state geometry, which allows us to separate the ADMs from the molecular frame terms

$$\begin{aligned} \langle I(\mathbf{q}) \rangle_{\text{rigid}}(t) = \mathcal{I} & \left( \sum_{\mu} |f_{\mu}(q)|^2 + \sum_{\mu, \nu: \mu \neq \nu} \text{Re} \left\{ f_{\mu}(q) f_{\nu}^*(q) \sum_l i^l 8\pi^2 \sqrt{\frac{4\pi}{(2l+1)}} \right. \right. \\ & \left. \left. \times \sum_{m_1, m_2} (-1)^{m_1 - m_2} Y_l^{-m_2} \left( \theta_q^{(\text{lf})}, \phi_q^{(\text{lf})} \right) \left\langle \Psi(0) \left| j_l(q \Delta r_{\mu\nu}) Y_l^{-m_1} \left( \theta_{\mu\nu}^{(\text{mf})}, \phi_{\mu\nu}^{(\text{mf})} \right) \right| \Psi(0) \right\rangle \mathcal{A}_{m_2 m_1}^l(t) \right|_{\text{rigid}} \right\} \right). \end{aligned} \quad (\text{S26})$$

This approximation is useful when investigating the ground state structure of a molecule or when the change in the molecule's geometry has a negligible impact on the moments of inertia.

### B. A Separation of Timescales Approximation for Excited State Dynamics

The second approximation is a separation of time scales between the rotational and vibronic dynamics. The anisotropy signature,  $\mathcal{A}_{mk}^l(t)$ , lasts of order one to tens of picoseconds for molecules with a few to tens of atoms, respectively. When the vibration or dissociation occurs on a much faster timescale than the change in anisotropy, we can calculate the rotational dynamics with respect to the known ground state geometry rather than with the unknown excited state geometry. The disparity in timescales is very common, and this approximation is analogous to the Born-Oppenheimer approximation.

We first consider the more general case of a double pump pulse experiment that first induces a rotational wavepacket and then launches a vibronic wavepacket. The first pulse increases the ensemble anisotropy and consequently the number of  $C_{lmk}(q, t)$  coefficients. The second pulse further mixes the rotational states while exciting vibronic modes. Let  $\tau$  denote the arrival time of the second vibration inducing pulse after the first rotation inducing pulse, and  $t$  is the elapsed time after the second pump pulse.

Our initial state is considered to be a thermal ensemble in the vibronic ground state. We describe a single initial state ( $i$ ) in the Born-Oppenheimer basis as

$$\left| \psi^{(i)}(0) \right\rangle = |J_i M_i K_i\rangle |0\rangle \quad (\text{S27})$$

prior to any pulses. After the alignment pulse, and before the vibration inducing pulse, our coherent rotational state evolves as

$$|\psi^{(i)}(\tau)\rangle = \sum_{JMK} c_{JMK}^{(i)}(\tau) |JMK\rangle |0\rangle. \quad (\text{S28})$$

The vibration pump pulse induces the excited state dynamics, while the photon's angular momentum mixes the rotational states. We project the vibronically excited state onto the Born-Oppenheimer basis,

$$|\Psi^{(i)}(t, \tau)\rangle = \sum_n \sum_{J_n M_n K_n} |J_n M_n K_n\rangle |n\rangle \langle J_n M_n K_n n | \Psi^{(i)}(t, \tau)\rangle \quad (\text{S29})$$

where the vibronic and rotational states are mixed by the ground state dipole moment and its orientation, respectively. To calculate the coefficients we apply time dependent perturbation theory and assumed an impulsive excitation

$$\langle J_n M_n K_n n | \Psi^{(i)}(t, \tau)\rangle = \sum_\gamma \langle J_n M_n K_n n | D_{0\gamma}^{1*} \mu_\gamma^1 | \psi^{(i)}(t, \tau)\rangle \frac{-i}{\hbar} \int_0^\infty E_0(t') e^{-i\Delta E t' / \hbar} dt' \quad (\text{S30})$$

$$= \tilde{E} \sum_{JMK} c_{JMK}^{(i)}(\tau + t) \sum_\gamma A(J_n, J; K_n, K; M\gamma) \langle n | \mu_\gamma^1 | 0\rangle \quad (\text{S31})$$

$$A(J_n, J; K_n, K; M\gamma) \equiv \langle J_n M K n | D_{0\gamma}^{1*} | J M K\rangle \quad (\text{S32})$$

$$= \sqrt{(2J+1)(2J_n+1)} (-1)^{\gamma+K-M} \begin{pmatrix} J & 1 & J_n \\ -M & 0 & M \end{pmatrix} \begin{pmatrix} J & 1 & J_n \\ -K & -\gamma & K_n \end{pmatrix}. \quad (\text{S33})$$

where  $\mu_\gamma^1$  is the spherical tensor of the transition dipole moment operator,  $E_0(t')$  is the electric field of the vibration inducing pulse,  $\Delta E$  is the energy difference between the initial rotational state and the excited state, and

$$\tilde{E} = \int_0^\infty E_0(t') e^{-i\Delta E t' / \hbar} dt'. \quad (\text{S34})$$

At this point we have only considered a single initial rotational state in our thermal ensemble. By summing over initial thermal states, weighting them by the Boltzmann distribution, the complete rovibronic state immediately after the vibration excitation pulse is given by

$$|\Psi(0, \tau)\rangle = \sum_{n J_n M K n} |n J_n M K n\rangle X_{J_n K_n}^n(M; 0, \tau) \quad (\text{S35})$$

$$X_{J_n K_n}^n(M; t, \tau) = \sum_{JK} \left( \frac{1}{Z} \sum_i c_{JMK}^{(i)}(\tau + t) p^{(i)} \right) \sum_\gamma \langle n | \mu_\gamma^1 | 0\rangle A(J_n, J; K_n, K; M\gamma). \quad (\text{S36})$$

Here  $Z$  is the partition function of the initial rotational states and  $p^{(i)}$  is Boltzmann weighting factor. Since we are interested in the time dynamics of the vibronic state, we apply the time translation operator to Eq. S35.

$$|\Psi(t, \tau)\rangle = \sum_{J_n M K n} \sum_n X_{J_n K_n}^n(M; t, \tau) |\psi_{\text{el-vib}}^n(t)\rangle |J_n M K n\rangle \quad (\text{S37})$$

$$|\psi_{\text{el-vib}}^n(t)\rangle = \hat{U}(t) |n\rangle \quad (\text{S38})$$

Now that we've calculated the time dependent rovibronic state in the Born-Oppenheimer basis, we must apply it to our measurement. We do this by taking the expectation value of our diffraction observable (Eq. S20) with respect to our new rovibronic system, Eq. S37. Here, we only look at the molecular scattering term since it is the only term



affected by  $|\Psi(t, \tau)\rangle$  and pull out the scattering amplitudes  $f_\mu(q)$  due to the independent atom approximation.

$$\langle I(\mathbf{q}) \rangle_{\text{sep}}^{(2)}(t, \tau) |_{\text{mol}} = \mathcal{I} \sum_{\mu, \nu: \mu \neq \nu} \text{Re} \left\{ f_\mu(q) f_\nu^*(q) \sum_l i^l 8\pi^2 \sqrt{4\pi(2l+1)} \sum_{m_1, m_2} (-1)^{m_1 - m_2} Y_l^{-m_2} \left( \theta_q^{(\text{lf})}, \phi_q^{(\text{lf})} \right) \right. \\ \left. \times \left\langle \Psi(t, \tau) \left| D_{m_2 m_1}^l \left( \phi_{\text{I}}^{(\text{lf})}, \theta_{\text{I}}^{(\text{lf})}, \chi_{\text{I}}^{(\text{lf})} \right) j_l(q\Delta r_{\mu\nu}) Y_l^{-m_1} \left( \theta_{\mu\nu}^{(\text{mf})}, \phi_{\mu\nu}^{(\text{mf})} \right) \right| \Psi(t, \tau) \right\rangle \right\} \quad (\text{S39})$$

$$= \mathcal{I} \sum_{\mu, \nu: \mu \neq \nu} \text{Re} \left\{ f_\mu(q) f_\nu^*(q) \sum_l i^l 8\pi^2 \sqrt{4\pi(2l+1)} \sum_{m_1, m_2} (-1)^{m_1 - m_2} Y_l^{-m_2} \left( \theta_q^{(\text{lf})}, \phi_q^{(\text{lf})} \right) \right. \\ \left. \times \sum_{nn'} \tilde{\mathcal{A}}_{m_1 m_2}^l(n, n'; t, \tau) \left\langle \psi_{\text{el-vib}}^{n'}(t) \left| j_l(q\Delta r_{\mu\nu}) Y_l^{-m_1} \left( \theta_{\mu\nu}^{(\text{mf})}, \phi_{\mu\nu}^{(\text{mf})} \right) \right| \psi_{\text{el-vib}}^n(t) \right\rangle \right\} \quad (\text{S40})$$

$$\tilde{\mathcal{A}}_{m_1 m_2}^l(n, n'; t, \tau) \equiv \sum_{J_n M K_n} \sum_{J'_n M' K'_n} X_{J_n K_n}^n(M; t, \tau) X_{J'_n K'_n}^{n'}(M'; t, \tau) \langle J'_n M' K'_n | D_{m_2 m_1}^l | J_n M K_n \rangle \quad (\text{S41})$$

We have again separated the ensemble anisotropy ( $\tilde{\mathcal{A}}_{m_1 m_2}^l(n, n'; t, \tau)$ ) from the molecular frame geometry term, which includes all the vibronic dynamics. The modified ADMs,  $\tilde{\mathcal{A}}_{m_1 m_2}^l(n, n'; t, \tau)$ , are analogous to the original ADMs, but now include the coherent rotational mixing from the vibronic inducing pulse. That is, each vibronic state will have its own rotational coherence that must be accounted for when calculating the ensemble anisotropy. Finally, plugging the molecular diffraction term (Eq. S40) into the full diffraction expression we get

$$\langle I(\mathbf{q}) \rangle_{\text{sep}}^{(2)}(t, \tau) = \mathcal{I} \left( \sum_\mu |f_\mu(q)|^2 + \sum_{\mu, \nu: \mu \neq \nu} \text{Re} \left\{ f_\mu(q) f_\nu^*(q) \sum_l i^l 8\pi^2 \sqrt{4\pi(2l+1)} \sum_{m_1, m_2} (-1)^{m_1 - m_2} \right. \right. \\ \left. \left. \times Y_l^{-m_2} \left( \theta_q^{(\text{lf})}, \phi_q^{(\text{lf})} \right) \tilde{\mathcal{A}}_{m_1 m_2}^l(n, n'; t, \tau) \left\langle \psi_{\text{el-vib}}^{n'}(t) \left| j_l(q\Delta r_{\mu\nu}) Y_l^{-m_1} \left( \theta_{\mu\nu}^{(\text{mf})}, \phi_{\mu\nu}^{(\text{mf})} \right) \right| \psi_{\text{el-vib}}^n(t) \right\rangle \right\} \right). \quad (\text{S42})$$

Due to the difference in timescales between the rotational and vibrational dynamics, we further simplify Eq. S42. In its current form, Eq. S42 relies on updating the ensemble anisotropy calculation as the geometry changes with vibration. This requires us to know what the geometry will be at time  $t$ , which is what we are ultimately trying to solve for. Instead, when the change in ensemble anisotropy is negligible with respect to the timescale of the vibration we can hold the anisotropy constant

$$\tilde{\mathcal{A}}_{m_1 m_2}^l(n, n'; \tau) = \tilde{\mathcal{A}}_{m_1 m_2}^l(n, n'; 0, \tau) \approx \tilde{\mathcal{A}}_{m_1 m_2}^l(n, n'; t, \tau) \quad (\text{S43})$$

$$\langle I(\mathbf{q}) \rangle_{\text{sep}}^{(2)}(t, \tau) \approx \mathcal{I} \left( \sum_\mu |f_\mu(q)|^2 + \sum_{\mu, \nu: \mu \neq \nu} \text{Re} \left\{ f_\mu(q) f_\nu^*(q) \sum_l i^l 8\pi^2 \sqrt{4\pi(2l+1)} \sum_{m_1, m_2} (-1)^{m_1 - m_2} \right. \right. \\ \left. \left. \times Y_l^{-m_2} \left( \theta_q^{(\text{lf})}, \phi_q^{(\text{lf})} \right) \tilde{\mathcal{A}}_{m_1 m_2}^l(n, n'; \tau) \left\langle \psi_{\text{el-vib}}^{n'}(t) \left| j_l(q\Delta r_{\mu\nu}) Y_l^{-m_1} \left( \theta_{\mu\nu}^{(\text{mf})}, \phi_{\mu\nu}^{(\text{mf})} \right) \right| \psi_{\text{el-vib}}^n(t) \right\rangle \right\} \right). \quad (\text{S44})$$

and the ensemble anisotropy and vibronic geometric dependence are completely separable. We therefore continue to calculate the ensemble anisotropy with respect to the ground state geometry while the molecular geometry has not appreciably changed on the timescale of the rotational dynamics.

In some cases, a single pump pulse experiment is preferred over a two pump pulse experiment when the setup is too difficult or when the anisotropy is difficult to induce or measure. In such a case, we simplify Eq. S44 by setting  $\tau = 0$ . Here, the ensemble anisotropy is imprinted immediately after the pulse by the interaction between the polarized laser and the excitation dipole.

$$\tilde{\mathcal{A}}_{m_1 m_2}^l(n, n') = \tilde{\mathcal{A}}_{m_1 m_2}^l(n, n'; 0, 0) \approx \tilde{\mathcal{A}}_{m_1 m_2}^l(n, n'; t, 0) \quad (\text{S45})$$

$$\langle I(\mathbf{q}) \rangle_{\text{sep}}^{(2)}(t, \tau) \approx \mathcal{I} \left( \sum_\mu |f_\mu(q)|^2 + \sum_{\mu, \nu: \mu \neq \nu} \text{Re} \left\{ f_\mu(q) f_\nu^*(q) \sum_l i^l 8\pi^2 \sqrt{4\pi(2l+1)} \sum_{m_1, m_2} (-1)^{m_1 - m_2} \right. \right. \\ \left. \left. \times Y_l^{-m_2} \left( \theta_q^{(\text{lf})}, \phi_q^{(\text{lf})} \right) \tilde{\mathcal{A}}_{m_1 m_2}^l(n, n'; t) \left\langle \psi_{\text{el-vib}}^{n'}(t) \left| j_l(q\Delta r_{\mu\nu}) Y_l^{-m_1} \left( \theta_{\mu\nu}^{(\text{mf})}, \phi_{\mu\nu}^{(\text{mf})} \right) \right| \psi_{\text{el-vib}}^n(t) \right\rangle \right\} \right). \quad (\text{S46})$$

Depending on the system, one may further improve this approximation by calculating the ensemble dynamics with respect to a reference geometry for  $t > 0$ . In some cases, the vibronic transience may be on the timescale of the rotational transience. Once Eqs S43 or S45 no longer hold at some time  $t$  there are two options. Firstly, one can use

only  $C_{000}(q, t)$  which does not rely on anisotropy and Eq. S42 will be exact. Secondly, one can continue calculating  $\tilde{\mathcal{A}}_{m_1 m_2}^l(n, n'; t, \tau)$  with respect to a reference geometry. For example, if one knows an excited state geometry is similar to the ground state one can continue to use  $\tilde{\mathcal{A}}_{m_1 m_2}^l(n, n'; t, \tau)$ . One must prove this through a priori knowledge or through the retrieved geometries at earlier times. In the case that the dynamics do not deviate from some other known geometry one may calculate the  $\tilde{\mathcal{A}}_{m_1 m_2}^l(n, n'; t, \tau)$  with respect to this geometry.

### X. FITTING FOR $B_l^m(q, t)$ AND $C_{lmk}(q)$ , AND COMMON MISTAKES

Our method relies heavily on two fitting procedures that will likely be the most important steps of the analysis as they define the  $C_{lmk}(q)$  coefficients and  $\sigma_{lmk}(q)$ . Below, we describe how one performs these fits analytically by minimizing the  $\chi^2$ . These analytical methods, however, will struggle to fit the measured time dependence with ADMs if there is not enough anisotropy and/or there is poor SNR. We therefore highly encourage one to validate the below, or their own, fitting procedure on their expected simulated data. One can employ L1 regularization techniques to improve these fits, but will likely have to use gradient descent since the derivative of  $|x|$  is undefined at  $x = 0$  and we do not know the sign of the  $B_l^m(q, t)$  and  $C_{lmk}(q)$  coefficients. Gradient descent will be much slower for numerous fits and should be used if the analytical approach is insufficient.

To minimize the  $\chi^2$  we cast it as a weighted linear regression problem with the loss function

$$\begin{aligned} L &= \frac{1}{2} \sum_{\mu} \frac{(\sum_{\nu} X_{\mu\nu} F_{\nu} - Y_{\mu})^2}{\epsilon_{\mu}} \\ &= \frac{1}{2} (\mathbf{X}\mathbf{F} - \mathbf{Y})^T \mathbf{W} (\mathbf{X}\mathbf{F} - \mathbf{Y}). \end{aligned} \quad (\text{S47})$$

Here,  $\mathbf{Y}$  is the data vector we wish to fit, the matrix  $\mathbf{X}$  are the fit bases (features) that span the columns,  $\mu$  sums over the detector pixels, and  $\nu$  sums over the fit bases. The bases are scaled by the fit coefficients  $\mathbf{F}$  and each data point's contribution to the fit is weighted by  $\mathbf{W}$ , where

$$\epsilon_{\mu} = \text{Var}(Y_{\mu}) \quad (\text{S48})$$

$$\mathbf{W} = \begin{bmatrix} \frac{1}{\epsilon_0} & 0 & \dots & 0 \\ 0 & \frac{1}{\epsilon_1} & & \\ \vdots & & \ddots & \\ 0 & & & \frac{1}{\epsilon_N}. \end{bmatrix} \quad (\text{S49})$$

Solving Eq. S47 for the optimal fit coefficients yields

$$\mathbf{F} = (\mathbf{X}^T \mathbf{W} \mathbf{X})^{-1} \mathbf{X}^T \mathbf{W} \mathbf{Y}. \quad (\text{S50})$$

The first fitting procedure in this method is to fit the measured data,  $I(\langle \mathbf{q}(\theta^{(d)}), t \rangle)$ , with the spherical harmonics,  $Y_l^m(\theta_q^{(\text{lf})}, \phi_q^{(\text{lf})})$ , to retrieve the  $B_l^m(q, t)$  coefficients. Where Eqs. S22 and S23 relate  $\theta_q^{(\text{lf})}$  and  $\phi_q^{(\text{lf})}$  in terms of  $\theta^{(d)}$ . Although the spherical harmonics are orthonormal, this orthonormality is broken by our finite sampling due to detector binning. To account for this now nonzero overlap between different bases, we fit the spherical harmonics to the data instead of projecting onto them. This is very important at low  $q$  where one often has the best SNR and the fewest bins to resolve  $\theta^{(d)}$ . We note that this can still be important even for the isotropic component due to the Jacobian. In the limit that the number of bins reaches infinity, the fit (Eq. S50) turns into a weighted projection. We use the trapezoidal rule to increase the orthonormality of our binned spherical harmonics

$$X_{\mu\nu} = \frac{1}{2} \left( Y_l^{\nu}(\theta_{q\mu}^{(\text{lf})}, \phi_{q\mu}^{(\text{lf})}) + Y_l^{\nu}(\theta_{q\mu+1}^{(\text{lf})}, \phi_{q\mu+1}^{(\text{lf})}) \right) \quad (\text{S51})$$

$$Y_{\mu} = \frac{1}{2} \left( \langle I(q, \theta_{\mu}^{(d)}, t) \rangle + \langle I(q, \theta_{\mu+1}^{(d)}, t) \rangle \right) \quad (\text{S52})$$

$$\epsilon_{\mu} = \frac{1}{2} \left( \text{Var} \left( \langle I(q, \theta_{\mu}^{(d)}, t) \rangle \right) + \text{Var} \left( \langle I(q, \theta_{\mu+1}^{(d)}, t) \rangle \right) \right) \quad (\text{S53})$$

$$F_{\nu} = B_l^{\nu}(q, t). \quad (\text{S54})$$

In Eq. S50 we are summing over  $\theta^{(d)}$  ( $\mu$ ), but since  $Y_l^m(\theta_q^{(\text{lf})}, \phi_q^{(\text{lf})}) \propto P_l^m(\cos(\theta_q^{(\text{lf})}))$  we must consider the  $\cos(\theta_q^{(\text{lf})})$  Jacobian. This can be resolved in two ways, by rebinning  $\theta^{(d)}$  in equally sized  $\cos(\theta_q^{(\text{lf})})$  bins, or by introducing the

Jacobian into  $\mathbf{W}$ . Since rebinning reduces our resolution, we alter the weight matrix

$$\widetilde{\theta}_{q\mu}^{(\text{lf})} = \frac{1}{2} \left( \theta_{q\mu}^{(\text{lf})} + \theta_{q\mu+1}^{(\text{lf})} \right) \quad (\text{S55})$$

$$\Delta\theta_{q\mu}^{(\text{lf})} = \theta_{q\mu+1}^{(\text{lf})} - \theta_{q\mu}^{(\text{lf})} \quad (\text{S56})$$

$$\mathbf{W} = \mathbb{1} \begin{bmatrix} \frac{\sin\left(\widetilde{\theta}_{q0}^{(\text{lf})}\right) \Delta\theta_{q0}^{(\text{lf})}}{\epsilon_0} \\ \frac{\sin\left(\widetilde{\theta}_{q1}^{(\text{lf})}\right) \Delta\theta_{q1}^{(\text{lf})}}{\epsilon_1} \\ \vdots \\ \frac{\sin\left(\widetilde{\theta}_{qN-1}^{(\text{lf})}\right) \Delta\theta_{qN-1}^{(\text{lf})}}{\epsilon_{N_{\text{bins}}-1}} \end{bmatrix} \quad (\text{S57})$$

where  $\mathbb{1}$  is the identity matrix.

Now we focus on retrieving the  $C_{lmk}(q)$  coefficients by fitting the  $\mathcal{A}_{mk}^l(t)$  to the  $B_l^m(q, t)$  coefficients. The  $\mathcal{A}_{mk}^l(t)$  are likely not orthogonal and may vary strongly in their magnitude (L2 norm). Consequently, the fit results from ADMs bases with larger magnitude can easily skew the results of other bases with lower magnitude. These skews can completely ruin the fit for the lower magnitude bases, while not being noticeable in the larger magnitude basis fit. This issue is also mitigated, or exacerbated, by increasing or decreasing the SNR, respectively. Another way to mitigate this issue is to add regularization terms to Eq. S47, which will alter Eq. S50. One would ideally like to use L1 regularization for sparsity, but for the reasons mentioned above one would need to use the gradient descent, which is much slower. To use Eqs. S47 and S50, one must make the following alterations:

$$X_{\mu\nu} = \frac{1}{2} \left( \mathcal{A}_{m_2\nu}^l(t_\mu) + \mathcal{A}_{m_2\nu}^l(t_{\mu+1}) \right) \quad (\text{S58})$$

$$Y_\mu = \frac{1}{2} \left( B_l^{m_2}(q, t_\mu) + B_l^{m_2}(q, t_{\mu+1}) \right) \quad (\text{S59})$$

$$\epsilon_\mu = \frac{1}{2} \left( \text{Var} \left( B_l^{m_2}(q, t_\mu) \right) + \text{Var} \left( B_l^{m_2}(q, t_{\mu+1}) \right) \right) \quad (\text{S60})$$

$$F_\nu = C_{lm_2\nu}(q) \quad (\text{S61})$$

$$\mathbf{W} = \begin{bmatrix} \frac{1}{\epsilon_0} & 0 & \dots & 0 \\ 0 & \frac{1}{\epsilon_1} & & \\ \vdots & & \ddots & \\ 0 & & & \frac{1}{\epsilon_N} \end{bmatrix}. \quad (\text{S62})$$

To improve the  $C_{lmk}(q)$  fitting, one can increase the SNR or induce a broader rotational wavepacket. In Figs. 4b and 6d we show how increasing the SNR improves the  $C_{lmk}(q)$  resolution. Figure 6f also shows how broadening the rotational wavepacket by a higher kick fluence has the similar effect. Again, we recommend that one runs these fit methods on the ground state geometry with simulated ADMs to see which  $C_{lmk}(q)$  coefficients will be retrieved with the expected anisotropy and SNR.

## XI. USING BAYESIAN INFERENCE AND THE METROPOLIS HASTINGS ALGORITHM

To measure  $|\Psi(\mathbf{r})|^2$  we analytically relate the data's dependence on  $|\Psi(\mathbf{r})|^2$  and determine a model to describe  $|\Psi(\mathbf{r})|^2$  and its dependence on said data. To aid the reader through this section, they may simultaneously read our simplified toy problem (Supplementary Section XIA), that follows this discussion step by step. Using Eq. S26 we isolate the molecular geometry terms and gain access to  $|\Psi(\mathbf{r})|^2$ , as shown in Eqs. 3-12.

$$C_{lmk}(q) = \int H_{lmk}(q, \mathbf{r}) |\Psi(\mathbf{r})|^2 d\mathbf{r} \quad (\text{S63})$$

$$H_{lmk}(q, \mathbf{r}) = \mathcal{I}\text{Re} \left\{ i^l (-1)^{k-m} 8\pi^2 \sqrt{\frac{4\pi}{(2l+1)}} \sum_{\mu, \nu: \mu \neq \nu} |f_\mu(q)| |f_\nu(q)| j_l(q\Delta r_{\mu\nu}) Y_l^{-k} \left( \theta_{\mu\nu}^{(\text{mf})}, \phi_{\mu\nu}^{(\text{mf})} \right) \right\} \quad (\text{S64})$$

We approximate  $|\Psi(\mathbf{r})|^2$  by choosing a probabilistic model that best describes our data, which we denote as  $P(\mathbf{r}|\Theta, C)$ . Our model  $P(\mathbf{r}|\Theta, C)$  is parameterized by  $\Theta$  and dependent on the measured  $C_{lmk}(q)$  coefficients, here denoted as  $C$ . We now rewrite Eq. S63 with our new model as

$$C_{lmk}^{(\text{calc})}(q, \Theta) = \int H_{lmk}(q, \mathbf{r}) P(\mathbf{r}|\Theta, C) d\mathbf{r}. \quad (\text{S65})$$

Some possible forms of  $P(\mathbf{r}|\Theta, C)$  include a multidimensional delta function which is analogous to a single geometry, a normal distribution of geometries which would describe the ground state, or the Hermite polynomials which would describe a vibronic wavefunction. In this work, we focus on the following  $P(\mathbf{r}|\Theta, C)$  and their corresponding  $\Theta$

$$P(\mathbf{r}|\Theta, C) \approx |\Psi(\mathbf{r})|^2 \quad (\text{S66})$$

$$P^{(\delta)}(\mathbf{r}|\Theta, C) = \delta(\Theta^{(\text{delta})} - \mathbf{r}) \quad (\text{S67})$$

$$\Theta^{(\text{delta})} = [\langle \text{NO}^{(1)} \rangle, \langle \text{NO}^{(2)} \rangle, \langle \angle \text{ONO} \rangle] \quad (\text{S68})$$

$$P^{(\mathcal{N})}(\mathbf{r}|\Theta, C) = \frac{1}{\sqrt{2\pi}^{N_{\text{dof}}} \prod_{i=0}^{i < N_{\text{dof}}} \Theta_{2i+1}^{(\text{gauss})}} \exp \left\{ \frac{-1}{2} \sum_{i=0}^{i < N_{\text{dof}}} \left( \frac{\Theta_{2i}^{(\text{gauss})} - \mathbf{r}_i}{\Theta_{2i+1}^{(\text{gauss})}} \right)^2 \right\} \quad (\text{S69})$$

$$\Theta^{(\text{gauss})} = [\langle \text{NO}^{(1)} \rangle, \sigma(\text{NO}^{(1)}), \langle \text{NO}^{(2)} \rangle, \sigma(\text{NO}^{(2)}), \langle \angle \text{ONO} \rangle, \sigma(\angle \text{ONO})]. \quad (\text{S70})$$

Given our model  $P(\mathbf{r}|\Theta, C)$ , we use Bayesian Inferencing and Markov Chain Monte Carlo (MCMC) techniques to find the optimal  $\Theta$  parameters ( $\Theta^*$ ) that best describe the observed  $C_{lmk}(q)$ . Bayesian Inferencing encompasses methods that use Bayes' Theorem to update the hypothesis [31, 34]. The most time, and computationally, intensive step of this analysis is building the posterior  $P(\Theta|C)$ , which we define through Baye's Theorem

$$P(\Theta|C) = \frac{P(C|\Theta)P(\Theta)}{P(C)}. \quad (\text{S71})$$

Here,  $P(C|\Theta)$  is the likelihood function which is the probability of measuring the data  $C$  given our selected model with the given  $\Theta$  parameters. The likelihood probability plays the largest role in building the posterior and is how information from the data enters the analysis. This can be calculated by assuming each  $C_{lmk}(q)$  measurement is its own experiment that results in a probability distribution. That is, given many measurements ( $N_{\text{images}}$ ) one builds a distribution of events for  $C_{lmk}(q)$  which quickly becomes a normal distribution, due to the Central Limit Theorem, with a mean and standard error of the mean. To calculate  $P(C|\Theta)$  one must multiply all of these probabilities

$$P(C|\Theta) = \left[ \prod_{lmk,q} \frac{1}{\sigma_{lmk}(q)\sqrt{2\pi}} \right] \exp \left\{ \frac{-1}{2} \sum_{lmk,q} \left( \frac{C_{lmk}(q) - C_{lmk}^{(\text{calc})}(q, \Theta)}{\sigma_{lmk}(q)} \right)^2 \right\} \quad (\text{S72})$$

where  $\sigma_{lmk}(q)$  is the standard error of the mean of  $C_{lmk}(q)$ . Since  $\sigma_{lmk}(q) \propto 1/\sqrt{N_{\text{images}}}$ , the summation in Eq. S72 scales as  $N_{\text{images}}$ . By measuring more photons or electrons, one exponentially sharpens the probability distribution  $P(\Theta|C)$ . As mentioned above, this assumes that each  $C_{lmk}(q)$  is an independent measurement which is not the case with sufficiently large x-ray/electron beams which have widths larger than the detector pixels. In such a scenario, one must alter Eq. S72 to account for this lack of independence.

The prior probability,  $P(\Theta)$ , describes the likelihood of a given  $\Theta$ . Since  $P(\Theta)$  does not depend on data, it encapsulates our prior knowledge of the  $\Theta$  parameters. Because we do not want to bias our search through  $\Theta$ -space we define

$$P(\Theta) = e^{K(\Theta)} \quad (\text{S73})$$

where  $K(\Theta) = 0$  for physical values and  $K(\Theta) = -\infty$  for unphysical values:  $\Theta < 0$  or  $\langle \angle \text{ONO} \rangle > \pi$ .

The marginal likelihood,  $P(C)$ , is the probability of observing our measured data. This probability is not something we concern ourselves with. Since it is not dependent on  $\Theta$  it is a constant that we cancel out in our MCMC technique.

Having chosen a model to approximate  $|\Psi(\mathbf{r})|^2$ , employed Bayesian Inferencing to define the posterior ( $P(\Theta|C)$ ) in terms of the  $C_{lmk}(q)$  coefficients, we now use MCMC techniques to build for  $P(\Theta|C)$ . We ultimately aim to invert a system of integral equations, but the complexity of Eq. S64 greatly limits the available methods to solve for  $P(\Theta|C)$ . For  $\text{NO}_2$ , we have  $\sim 10$   $C_{lmk}$  coefficients, each with 6 terms from summing over  $\Delta \mathbf{r}_{\mu\nu}$  that span  $\sim 100$   $q$  bins. When evaluating  $C_{lmk}^{(\text{calc})}(q, \Theta)$ , such equations are parameterized within the 6d space of  $\Theta$  parameters. This  $\theta$

dimensional space is where the curse of dimensionality comes in, as  $\theta$  has at least  $3N_{\text{atoms}} - 6$  parameters that dictates the dimensionality we must search in to build  $P(\Theta|C)$ . To evaluate all these equations, even for a triatomic, in a random or grid-like search to find  $\Theta^*$  with femtometer resolution is computationally infeasible. Instead, we retrieve  $P(\Theta|C)$  with the Metropolis-Hasting algorithm (MHA): a MCMC method developed for such high dimensional integral equations [36], as in Eq. S65.

The MHA is a sampling algorithm that builds the joint probability distribution  $P(\Theta|C)$  by randomly selecting  $\Theta$  parameters and comparing their likelihood probabilities with neighboring  $\Theta'$  parameters. At completion, our retrieved  $P(\Theta|C)$  is a list of selected  $\Theta$  parameters randomly selected from the true  $P(\Theta|C)$  distribution. Reference [34] describes the python package used in this analysis. To help the reader better understand our use of the MHA, we now describe one iteration. Let  $\Theta$  be the latest addition to  $P(\Theta|C)$ . The MHA selects a nearby  $\Theta'$  with the transition probability  $Q(\Theta, \Theta')$ . We require  $Q(\Theta, \Theta') = Q(\Theta', \Theta)$  so it is equally likely to revisit every region of  $\Theta$ -space. Generally  $Q(\Theta, \Theta')$  is uniform or Gaussian. With  $\Theta$  and  $\Theta'$  selected, the MHA appends  $\Theta'$  to  $P(\Theta|C)$  with probability

$$\begin{aligned} \rho(\Theta, \Theta') &= \min \left[ 1, \frac{P(\Theta'|C) Q(\Theta, \Theta')}{P(\Theta|C) Q(\Theta', \Theta)} \right] \\ &= \min \left[ 1, \frac{P(C|\Theta') P(\Theta') Q(\Theta, \Theta')}{P(C|\Theta) P(\Theta) Q(\Theta', \Theta)} \right], \end{aligned} \tag{S74}$$

otherwise it appends  $\Theta$  again. The ratio in Eq. S74 cancels out  $P(C)$ , and when  $P(\Theta) = P(\Theta')$  for all physical quantities, as it does for our case, we are only concerned with the ratio of likelihood probabilities. The process then repeats itself by selecting a new  $\Theta'$ . Since each  $\Theta$  has either the same values or is a neighbor of the previously selected  $\Theta$  the raw  $P(\Theta|C)$  distribution is not an independently drawn distribution. To remove this correlation between consecutively selected  $\Theta$  parameters, we select the  $\Theta$  parameters after every  $\tau^{(\text{AC})}$ . Here  $\tau^{(\text{AC})}$  is the autocorrelation time; the number of MHA steps needed to no longer be correlated with your starting position [34]. Thus, our retrieved  $P(\Theta|C)$  is a set of  $\Theta$  parameters independently drawn from the true  $P(\Theta|C)$ . Since the early MHA selected  $\Theta$  parameters will be affected by our initial guess and the MHA requires time to equilibrate, we remove the first 5  $\Theta$ s (after pruning by  $\tau^{(\text{AC})}$ ). Reference [34] describes in more detail how to determine when  $P(\Theta|C)$  has converged.

The intuition of Eq. S74 is that if one cannot evaluate  $P(\Theta|C)$  analytically or numerically, but can calculate it up to a constant, then they can build  $P(\Theta|C)$  by taking the ratio of neighboring points. The MHA uses the ratio of likelihood probabilities as a guide towards regions of higher posterior probability. That is, the ratio of likelihood functions, where  $P(\Theta|C) \propto P(C|\Theta)$ , may indicate that  $\Theta$  is twice as likely as  $\Theta'$  and consequently the MHA will visit  $\Theta$  twice as often as  $\Theta'$ . This selective sampling of  $\Theta$  parameters allows one to tackle the curse of dimensionality by efficiently sampling  $\Theta$ -space while ignoring regions of low probability. For example, if  $\Theta''$  were 100 time less likely than  $\Theta'$ , and  $\Theta'$  is 50 times less likely than  $\Theta$ , one would visit  $\Theta''$  once for every 50,000 visits to  $\Theta$ . This makes it very unlikely one ever visits the region near  $\Theta''$  or any region further in  $\Theta$ -space that would be less likely. This also means that one spend most of their time sampling the highly likely region around  $\Theta$  to improve resolution. Stated more rigorously, the region of  $\Delta\Theta$  is sampled  $(\int_{\Delta\Theta} P(C|\theta)d\theta)/(\int_{\Delta\Theta'} P(C|\theta)d\theta) = (\int_{\Delta\Theta} P(\theta|C)d\theta)/(\int_{\Delta\Theta'} P(\theta|C)d\theta)$  times more than  $\Delta\Theta'$ . The MHA search is analogous to a random walk guided by the geometries' relative agreement to the data, rather than a random sampling of distributions.

With the retrieved  $P(\Theta|C)$  is we can find  $\Theta^*$ , the global maximum, and evaluate the correlations between the parameters,  $\sigma^\Theta$ . Since  $P(\Theta|C)$  is a list of  $\Theta$  parameters, we can calculate aggregate quantities. With enough samples, one can histogram the collected  $\Theta$  parameters and/or apply a high dimensional kernel density estimator to retrieve a functional form of  $P(\Theta|C)$  [62].

It is important to note the MHA is theory independent when  $P(\Theta)$  is constant, and that filtering the MHA results by  $\tau^{(\text{AC})}$  yields independently drawn samples. This alleviates any bias of sampling geometries from physically motivated distributions that are not fully validated. One can use  $P(\Theta)$  to input chemical knowledge of the system if preferred. Although the results will be biased by this input, one will not spend time sampling potentially erroneous  $\Theta$  parameters.

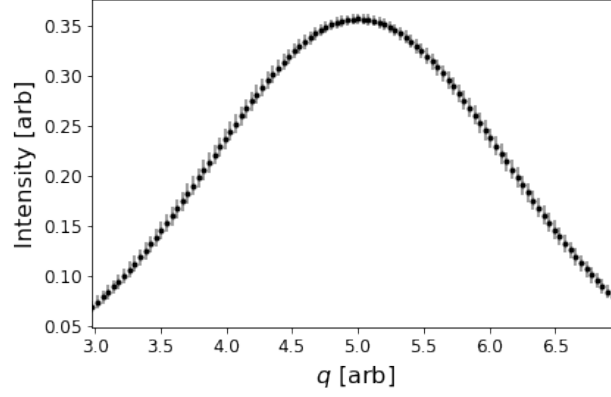


FIG. S3. We show the simulated dataset for the toy MCMC problem.

### A. Toy Problem

To illustrate how the MHA retrieves  $|\Psi(\mathbf{r})|^2$  we solve a toy problem with similar features. The physical distribution we want to measure is

$$|\Psi(m)|^2 = \frac{1}{\sigma_{\text{toy}}\sqrt{2\pi}} e^{\left(\frac{-(m-\bar{M})^2}{2\sigma_{\text{toy}}^2}\right)} \quad (\text{S75})$$

$$\bar{M} = 5 \quad (\text{S76})$$

$$\sigma_{\text{toy}} = 0.5. \quad (\text{S77})$$

Similar to our diffraction experiment, we do not know the prior ( $P(m)$ ) which would require an a priori theoretical calculation, which we assume is prohibitively difficult. We aim to retrieve the model parameters  $\bar{M}$  and  $\sigma_{\text{toy}}$ .

For our example, we create a dataset and specify its dependence on the desired  $|\Psi(m)|^2$  distribution. We build the dataset by drawing 10000 events ( $m_i$ ) from  $|\Psi(m)|^2$  that are sent through an experimental response function, a Gaussian blur

$$\langle I_{\text{toy}}(q) \rangle = \sum_{i=1}^{10000} \frac{1}{\sigma_{\text{smear}}\sqrt{2\pi}} \exp\left\{\frac{-(m_i - q)^2}{2\sigma_{\text{smear}}^2}\right\}. \quad (\text{S78})$$

There are 100 events in each “measurement” and the resulting dataset is shown in Fig. S3, where the error bars are the standard error of the mean  $\sigma_I(q)$ . Figure S4a (blue histogram) shows the distribution of  $m_i$  drawn from  $|\Psi(m)|^2$  to calculate the dataset. In diffraction, Eq. S20 is the experimental response and the measurements are diffraction patterns. For the diffraction dataset we retrieved the  $C_{lmk}(q)$  coefficients by fitting the data, in this simplified example we can directly relate  $\langle I_{\text{toy}}(q) \rangle$  to  $|\Psi(m)|^2$  by

$$\langle I_{\text{toy}} \rangle(q) = \int_{-\infty}^{\infty} H_{\text{toy}}(q, m) |\Psi(m)|^2 dm \quad (\text{S79})$$

$$H_{\text{toy}}(q, m) = \frac{1}{\sigma_{\text{smear}}\sqrt{2\pi}} \exp\left\{\frac{-1}{2} \frac{(m - q)^2}{\sigma_{\text{smear}}^2}\right\} \quad (\text{S80})$$

which corresponds to Eqs. S63 and S64 for the diffraction experiment. Our calculated response is given by substituting the physical  $|\Psi(m)|^2$  for our model

$$\langle I_{\text{toy}}^{(\text{calc})} \rangle(q) = \int_{-\infty}^{\infty} H_{\text{toy}}(q, m) P(m|\Theta, \langle I_{\text{toy}} \rangle) dm. \quad (\text{S81})$$

With our dataset and a mathematical description of it in terms of  $|\Psi(m)|^2$ , we select a form of  $P(m|\Theta, \langle I_{\text{toy}} \rangle)$ ,

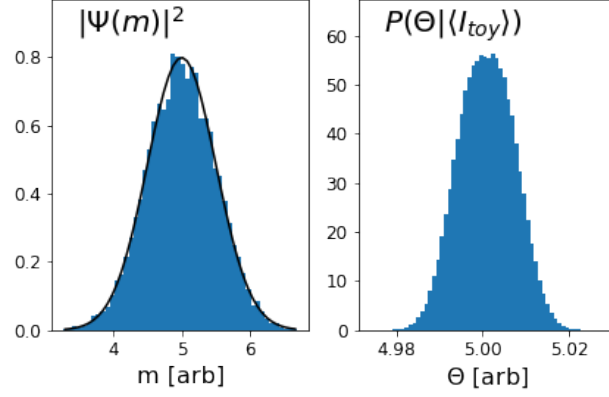


FIG. S4. In our toy MHA problem, we build the posterior and retrieve the correct  $|\Psi(m)|^2$ . In panel a, the blue histogram shows the distribution of points drawn from  $|\Psi(m)|^2$  and the black line represents the retrieved  $P(m|\Theta^*, \langle I_{\text{toy}} \rangle)$ . Panel b shows the retrieved  $P(\Theta|\langle I_{\text{toy}} \rangle)$  posterior with a much smaller width.

parameterized by  $\Theta$ . Since we already know the functional form of  $|\Psi(m)|^2$  we define our model as

$$P(m|\Theta, \langle I_{\text{toy}} \rangle) = \frac{1}{\sigma_{\text{toy}} \sqrt{2\pi}} \times \exp \left\{ \frac{-(m - \Theta)^2}{2\sigma_{\text{toy}}^2} \right\} \quad (\text{S82})$$

$$\Theta = \langle m \rangle \quad (\text{S83})$$

and  $\Theta$  is no longer a vector since we have only one parameter for simplicity. We now want to solve for the posterior  $P(\Theta|\langle I_{\text{toy}} \rangle)$  using Bayesian Inferencing by relating  $P(\Theta|\langle I_{\text{toy}} \rangle)$  to the data via Baye's Theorem

$$P(\Theta|\langle I_{\text{toy}} \rangle) = \frac{P(\langle I_{\text{toy}} \rangle|\Theta)P(\Theta)}{P(\langle I_{\text{toy}} \rangle)} \quad (\text{S84})$$

The  $P(\Theta)$ ,  $P(\langle I_{\text{toy}} \rangle)$ , and  $P(\langle I_{\text{toy}} \rangle|\Theta)$  are the prior, marginal likelihood, and likelihood distributions, respectively. In this toy example, we do not use the prior to constrain any values, so it is a constant. The marginal likelihood,  $P(\langle I_{\text{toy}} \rangle)$ , is a constant that is independent of  $\Theta$  and cancelled out. The likelihood probability,  $P(\langle I_{\text{toy}} \rangle|\Theta)$ , is given by

$$P(\langle I_{\text{toy}} \rangle|\Theta) = \prod_q \frac{1}{\sigma_I(q) \sqrt{2\pi}} \times \exp \left\{ \frac{-1}{2} \left( \frac{(\langle I_{\text{toy}} \rangle(q) - \langle I_{\text{toy}}^{\text{calc}} \rangle(q, \Theta))^2}{\sigma_I^2(q)} \right) \right\} \quad (\text{S85})$$

where  $\sigma_I(q)$  is the standard error of the mean.

Having set up the problem, we now solve for  $\Theta^*$  by building  $P(\Theta|\langle I_{\text{toy}} \rangle)$  via the MHA. Figure S4b shows the resulting  $P(\Theta|\langle I_{\text{toy}} \rangle)$  distribution with a  $\tau^{(\text{AC})} = 25$ . From  $P(\Theta|\langle I_{\text{toy}} \rangle)$  we find  $\Theta^* = 5.00$ , which matches our given value of  $\bar{M} = 5$ . The high SNR creates a peaked  $P(\Theta|\langle I_{\text{toy}} \rangle)$  with a standard deviation of 0.006.

We finish our measurement of  $|\Psi(m)|^2$  by completing our model  $P(m, \Theta|\langle I_{\text{toy}} \rangle)$ . To do so, we plug in the retrieved  $\Theta^*$  to yield  $P(m|\Theta^*, \langle I_{\text{toy}} \rangle)$ . Figure S4(a) shows both  $|\Psi(m)|^2$  (blue histogram) and  $P(m|\Theta^*, \langle I_{\text{toy}} \rangle)$  (black line). We see that they agree very well since  $\Theta^* = \bar{M}$ .

## XII. CALCULATING ERROR BARS FOR $B_l^m(q, t)$ AND $C_{lmk}(q)$ COEFFICIENTS

The standard error of the mean of the  $C_{lmk}(q)$  coefficients ( $\sigma_{lmk}(q)$ ) contains information regarding the width and shape of  $P(\Theta|C)$ . Similarly, the  $C_{lmk}(q)$  will shift the entire distribution  $P(\Theta|C)$  distribution and may also

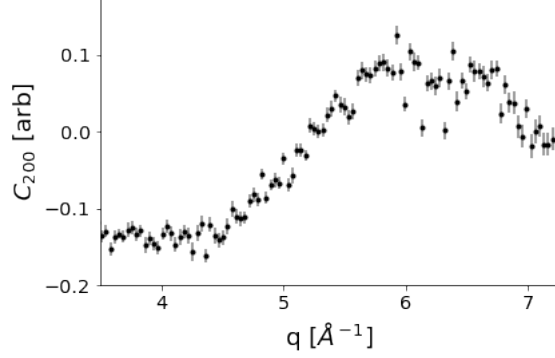


FIG. S5. We show the raw  $C_{200}(q)$  coefficients for the collected  $\text{N}_2\text{O}$  data.

change its shape. For these reasons, it is crucial to include systematic effects in  $\sigma_{lmk}(q)$  so the width of  $P(\Theta|C)$  will encompass the correct results even if  $P(\Theta|C)$  is systematically shifted. The  $\sigma_{lmk}(q)$  can be found in different ways, here we discuss three methods. The first method is to directly measure the statistical uncertainty, as we did for  $\text{N}_2\text{O}$ . The second method is a means of estimating systematic uncertainty from experimental artifacts, also used in our  $\text{N}_2\text{O}$  analysis. The third method is to analytically propagate the statistical uncertainty, which is useful for simulations.

The first method of directly measuring the statistical error follows standard practices. One first fits each individual diffraction image (Supplementary Section X) to retrieve the  $C_{lmk}(q)$  coefficients. One then calculates  $\sigma_{lmk}(q)$  from this distribution of the  $C_{lmk}(q)$  coefficients. One can also bootstrap  $\sigma_{lmk}(q)$  by fitting many different combinations of diffraction images for  $C_{lmk}(q)$  and calculating the standard deviation of the resulting distribution. In our  $\text{N}_2\text{O}$  analysis we fit single diffraction images for  $C_{lmk}(q)$  and calculated the standard error of the mean from this distribution, shown in Fig. S5.

The second method addresses systematic effects from the experimental apparatus that the first method will miss. In this dataset, the  $q$  calibration changed as a function of  $\theta^{(d)}$  which washed out the signal below  $3.5 \text{ \AA}^{-1}$  and created a time dependent offset that varied as  $\mathcal{A}_{00}^2(t)$ . This dataset also suffered from high frequency variations in  $q$ . We removed the high frequency noise and the time dependent offset from  $C_{200}(q)$  by applying a low-pass filter and subtracting an offset, shown in Fig. S6. The filter cut began around  $4 \text{ \AA}$ , far from our longest expected distance of  $2.3 \text{ \AA}$ . We note that

$$\mathcal{F}[C_{200}(q)] \propto \sum_{\mu\nu} \mathcal{F}[j_2(q\Delta r_{\mu\nu})]$$

and is not the PDF. Using the convolution theorem, we still do not expect any signal above  $2.3 \text{ \AA}$ . After subtracting an offset from the raw data and rescaling, we observe the dashed black line in Fig. S6a.

After applying the low-pass filter, we must account for the variations it removed in the error bars. Figure S7a shows the filtered results with the residuals added in quadrature to the original error bars, Fig. S7b shows these residuals. We fit the residuals with a quadratic since we do not expect the error to vary wildly between adjacent points after filtering. The final error bars are shown in Fig. S7c.

The third method, which is only for simulation, is to propagate the error through the fitting procedure. For simulated data we only need to consider minimizing the  $\chi^2$ , but for real data one will likely have to include regularization terms. Starting from Eqs. S50 and S49, the variance of our fit coefficients is given by

$$\text{Var}(\mathbf{F}) = (\mathbf{X}^T \mathbf{W} \mathbf{X})^{-1} \mathbf{X}^T \mathbf{W} \text{Var}(\mathbf{Y}) \left( (\mathbf{X}^T \mathbf{W} \mathbf{X})^{-1} \mathbf{X}^T \mathbf{W} \right)^T \quad (\text{S86})$$

$$= (\mathbf{X}^T \mathbf{W} \mathbf{X})^{-1} \mathbf{X}^T \mathbf{W} \mathbf{W}^{-1} \left( (\mathbf{X}^T \mathbf{W} \mathbf{X})^{-1} \mathbf{X}^T \mathbf{W} \right)^T \quad (\text{S87})$$

$$= (\mathbf{X}^T \mathbf{W} \mathbf{X})^{-1}. \quad (\text{S88})$$

To propagate the Poissonian noise measured on the detector to the  $C_{lmk}(q)$  coefficients we examine the two fitting procedures described in Supplementary Section X. We first propagate through fitting the diffraction images with Spherical Harmonics to retrieve the  $B_l^m(q, t)$  coefficients. The simulated Poissonian noise on the detector is given by

$$\text{Var}(\langle I(q, \theta^{(d)}, t) \rangle) = \langle I(q, \theta^{(d)}, t) \rangle \quad (\text{S89})$$



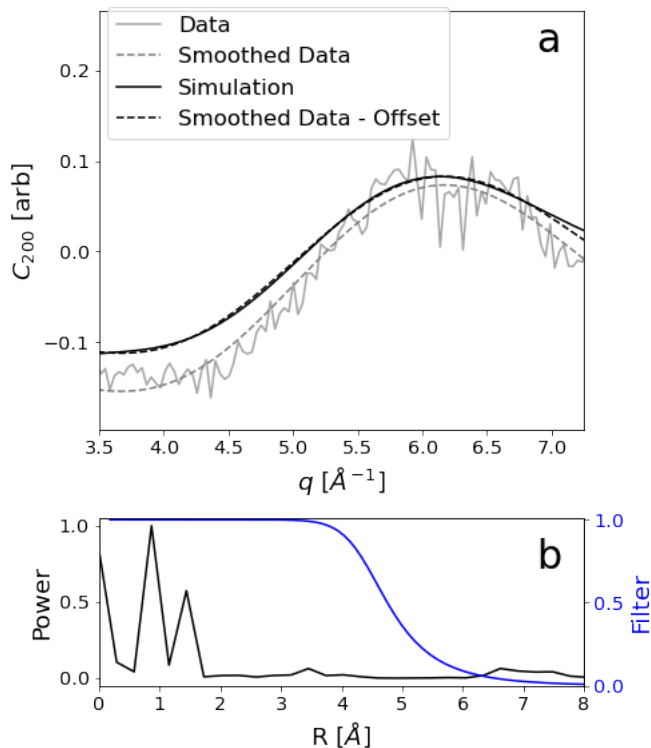


FIG. S6. Both systematic and statistical errors must be carefully addressed in measured data. Here, we show the data after accounting for noise and systematic effects. Panel a (gray) shows the original and smoothed data and its comparison to the simulated data before and after subtracting the offset. Panel b shows the Fourier power spectrum (PDF) of the data (black) and the applied a low-pass filter (blue).

where  $\mathbf{X}$  and  $\mathbf{W}$  are given by Eqs. S51 and S57 respectively. To calculate the  $C_{lmk}(q)$  coefficient error bars we again use Eq. S88. Instead, the  $\mathbf{X}$  and  $\mathbf{W}$  are given by Eqs. S58 and S62 respectively.

### XIII. SEARCHING FOR THE OPTIMAL $\Theta$ PARAMETERS

After retrieving  $P(\Theta|C)$ , one must find the most likely  $\Theta$  parameters,  $\Theta^*$ , by overcoming the curse of dimensionality. Here  $N_{\Theta}$  is the number of  $\Theta$  parameters and the dimensionality of our search space. Since this high dimensionality prohibits evaluating all the parameters with a reasonable resolution, we use Bayesian Inferencing and the Metropolis Hastings Algorithm (MHA) to retrieve  $P(\Theta|C)$ . We re-emphasize again that we are interested in the  $\Theta^*$  that best describes our data which is given by the mode of  $P(\Theta|C)$ , which does not necessarily correspond to the mean of  $P(\Theta|C)$ . As well, if one looks at a single parameter  $\theta$  the mean or mode of this uncorrelated distribution may not correspond to the value that would provide the highest  $P(\Theta|C)$  value in the full  $\Theta$ -space: illustrated in Fig. 7. One must therefore search the correlated  $\Theta$ -space. Once the MHA has converged,  $P(\Theta|C)$  may have significantly constrained  $\Theta$  space, but searching for the mode may still be infeasible for a simple grid search. Below we describe three methods to find  $\Theta^*$  using  $P(\Theta|C)$  to help us overcome the curse of dimensionality.

The first and most simple way to find  $\Theta^*$  is to apply the MHA to the measured  $C_{lmk}(q)$  coefficients in the same way as before, but significantly decrease  $\sigma_{lmk}(q)$ . One can make  $P(\Theta|C)$  arbitrarily sharp, effectively zooming onto the mode, by artificially decreasing  $\sigma_{lmk}(q)$ . With small enough  $\sigma_{lmk}(q)$  one can zoom into  $P(\Theta|C)$  until it is adequately described by a quadratic, where the mean and the mode of the distribution will be the same. The danger of using this method is that one may fall into a local minimum if one decreases  $\sigma_{lmk}(q)$  too quickly without being careful. For example, one's initial  $\Theta$  guess may be close to a local minimum and the small  $\sigma_{lmk}(q)$  will force the MHA into it and not sample outside of it. To avoid this, one must start the MHA in many different initial  $\Theta$  states and gradually decrease  $\sigma_{lmk}(q)$  to find the global minima and rule out any local minima.

The second method is to interpolate  $P(\Theta|C)$  between the evaluated MHA points using a high dimensional Kernel Density Estimator (KDE). We note that one can use all the MHA points rather than the points in  $P(\Theta|C)$  which

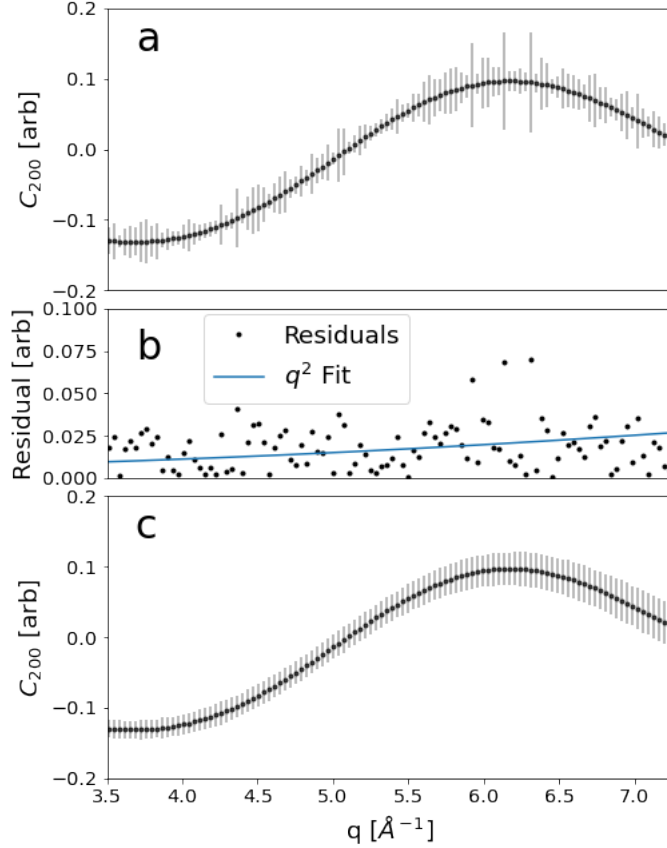


FIG. S7. After filtering the data, the error bars must be re-calibrated to account for the removed noise. We illustrate our procedure for finding  $\sigma_{200}(q)$  for the  $\text{N}_2\text{O}$  data. Panel a shows the low-pass filtered results where we added the residuals in quadrature with the error bars. Panel b shows these residuals between the low-pass filtered and original data, as well as a quadratic fit to them. Panel c shows the filtered data with error bars determined by the fit in panel b.

are filtered by the auto-correlation time  $\tau^{(\text{AC})}$ . This is because we are looking for the mode and not evaluating some function over the  $P(\Theta|C)$  distribution. The primary difficulty with KDEs is finding the shape and width of the kernel. Generally, KDE methods do not perform well for problems in larger than three dimensions. More recently, there has been work to generalize KDEs to high dimensions [62]. Calculating points in  $P(\Theta|C)$  with a KDE will be very fast. Such quick evaluations may allow one to find the mode through simple optimization schemes like a basic grid search or gradient descent.

The third method, used in this paper, is a mixture of simple searching methods and calculating  $\Theta^*$  by a weighted average of the most likely MHA points. By considering only the  $N_{\text{likely}}$  unique points with the highest likelihood probability we focus on the global minima while disregarding tails of the  $P(\Theta|C)$  distribution. Since we are only concerned with the most likely points, we look at all the points the MHA accepted instead of only looking at  $P(\Theta|C)$ , which takes MHA points separated by the auto-correlation time  $\tau^{\text{AC}}$ . We calculate  $\Theta^*$  by a weighted sum of the  $N_{\text{likely}}$   $\Theta$  parameters, weighting each by their likelihood probability. With our current calculated  $\Theta^*$  value we perform a grid search where points are separated by 0,  $\pm 1$ , and  $\pm 2$  standard deviations ( $\sigma_i^{(\text{MS})}$ ). Here  $\sigma_i^{(\text{MS})}$  is the one dimensional standard deviation of the  $i^{\text{th}}$   $\Theta$  parameter taken over the distribution of the  $N_{\text{likely}}$   $\Theta$ s. Once every parameter changes by  $< 3\%$  for five consecutive times we switch to a random sampling method. We randomly sample values from a normal distribution between 0.5 and  $2\sigma_i^{(\text{MS})}$  from the current  $\Theta^*$ . We consider  $\Theta^*$  has converged when every parameter has changed  $< 0.01\%$  for three consecutive random samplings, but require at least one value to change between samplings.

There are many ways to search for  $\Theta^*$  that generally trade between speed and accuracy. More advanced techniques will allow one to converge upon the ground truth values even with a broad and imprecise  $P(\Theta|C)$ . Our simple search method performed well for all our experimental variations, but was affected by the broadest  $P(\Theta|C)$  distributions. One may need a more advanced method for such broader distributions. In order to calculate the precision of  $\Theta^*$  one

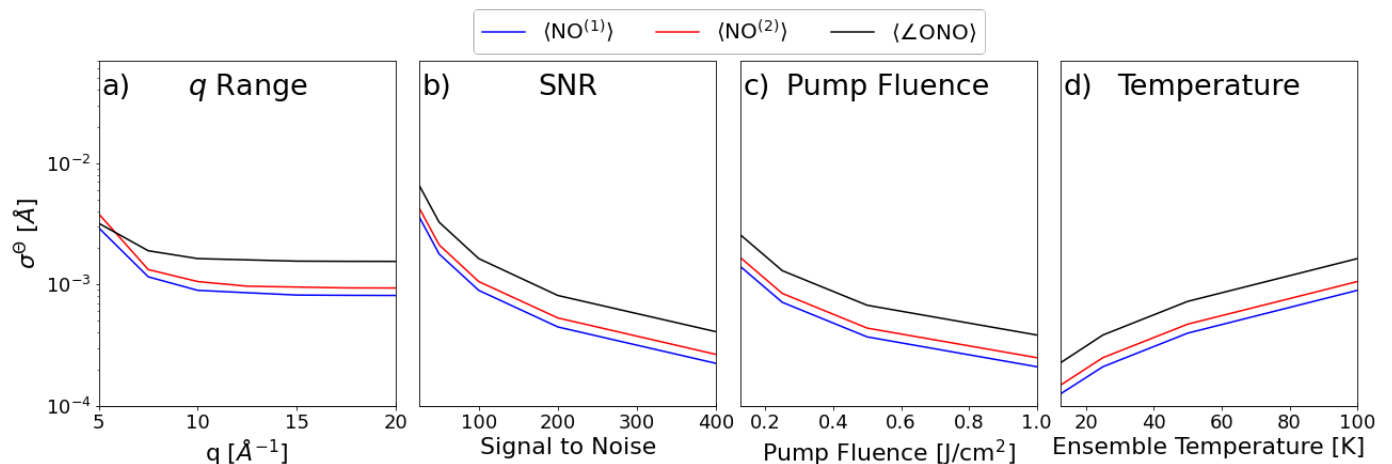


FIG. S8. Varying experimental parameters affect the retrieved resolution (width) of  $P^{(\delta)}(\mathbf{r}|\Theta, C)$ , which is most sensitive to SNR. Panel a shows how the uncorrelated widths of  $P^{(\delta)}(\Theta|C)$ , denoted by  $\sigma^\Theta$ , changes by increasing  $q$  range. Panel b similarly shows the dependence of  $\sigma^\Theta$  and  $\Theta^*$  error versus SNR. Panel c shows the dependence of  $\sigma^\Theta$  and  $\Theta^*$  error versus pump fluence (width of the rotational wavepacket). Panel d shows the dependence of  $\sigma^\Theta$  and  $\Theta^*$  error versus the molecular ensemble temperature.

must find the hyper curve in  $\Theta$  space with minimal precision, as outlined in Ref. [63].

#### XIV. RESULTS OF THE DELTA DISTRIBUTION POSTERIOR

The delta posterior,  $P^{(\delta)}(\mathbf{r}|\Theta, C)$ , is quick to calculate but assumes the  $C_{lmk}(q)$  coefficients calculated from a single geometry and measured from an ensemble of geometries are comparable. This assumption effectively ignores the damping of the  $C_{lmk}(q)$  as a function of  $q$ , similar to a damped oscillator, due to the width of  $|\Psi(\mathbf{r})|^2$ . Figure 8 shows this  $q$  dependent systematic where  $P^{(\delta)}(\Theta|C)$  converges on the ground truth values in an unstable fashion as  $q$  increases. The ground truth value, at times, can be considerably far from the retrieved distribution's mean, and with improved SNR may quickly be separated by  $> 3$  standard deviations. The retrieved mean can also jump to either side of the ground truth values at low  $q$ . This behavior, along with the systematic error, is absent in Fig. 8 for  $P^{(\mathcal{N})}(\Theta|C)$ .

Even with this systematic error, we find that  $P^{(\delta)}(\mathbf{r}|\Theta, C)$  follows the same trends as  $P^{(\mathcal{N})}(\mathbf{r}|\Theta, C)$  when varying experimental parameters, as shown in Fig. S8. We similarly see that for  $P^{(\delta)}(\mathbf{r}|\Theta, C)$  our method benefits more strongly from increased SNR, rather than increasing the measured  $q$  range. One will again see diminishing returns when measuring past  $\sim 8 \text{ \AA}^{-1}$ . Increasing the alignment kick strength and decreasing the ensemble temperature also have a similar effect as increasing the SNR.

Although the delta distribution suffers from the above-mentioned systematic, it is very important when building and debugging one's analysis and is necessary for very large molecules. Retrieving  $P^{(\delta)}(\Theta|C)$  is roughly 100 times faster than retrieving  $P^{(\mathcal{N})}(\Theta|C)$  due to dropping half the  $\Theta$  space dimensions in the retrieval of  $P^{(\mathcal{N})}(\Theta|C)$  and removing the integration over many geometries drawn from  $P^{(\mathcal{N})}(\mathbf{r}|\Theta, C)$  when calculating  $C_{lmk}^{(\text{calc})}(q)$ . We highly encourage the reader to use  $P^{(\delta)}(\Theta|C)$  when debugging due to its fast execution and sufficient accuracy for such intermediate evaluations. For large molecules  $\Theta$ -space grows exponentially and the  $C_{lmk}^{(\text{calc})}(q)$  integral becomes more computationally intensive. At some point, it is computationally infeasible for the MHA to search such a large  $\Theta$  space when it must compute the  $C_{lmk}^{(\text{calc})}(q)$  integral for every  $\Theta$  it randomly chooses. For such large molecules, one will need to use the delta distribution. To account for the delta distribution's systematic error, one can increase  $\sigma_{lmk}(q)$  so  $P^{(\delta)}(\Theta|C)$  comfortably encompasses the ground truth values. One can run the same simulations done in this paper on expected, or measured, geometries to determine such an increase. By doing so, one can report results that account for the induced systematic errors from our assumption of  $|\Psi(\mathbf{r}, t)|^2$ 's shape.

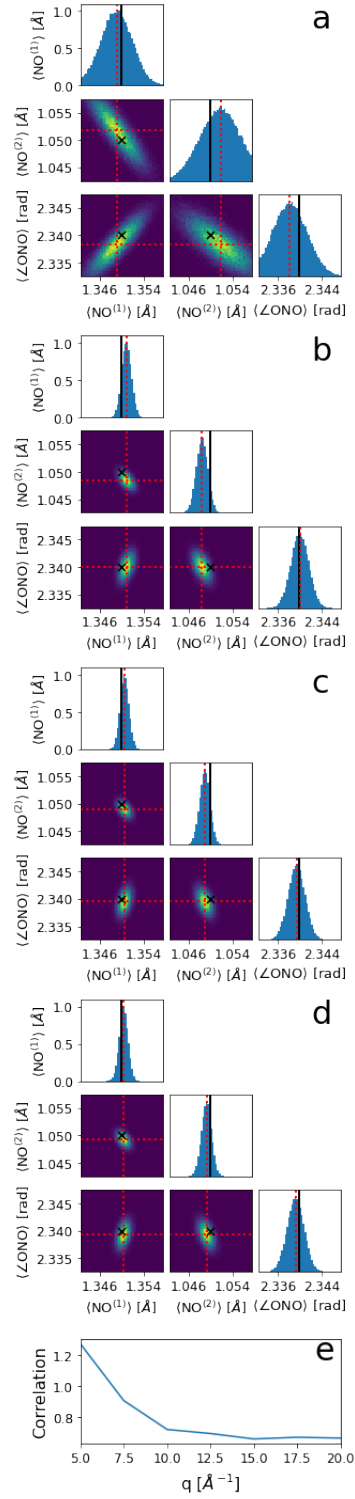


FIG. S9. Varying the  $q$  range affects false correlations in  $P^{(\delta)}(\Theta|C)$ . We show the 1d and 2d projections of the retrieved  $P^{(\delta)}(\Theta|C)$  distribution for varying  $q$  ranges. Panel a has a  $q$  range of  $[0.5, 5] \text{ \AA}^{-1}$ , b is  $[0.5, 10] \text{ \AA}^{-1}$ , c is  $[0.5, 15] \text{ \AA}^{-1}$ , and d is  $[0.5, 20] \text{ \AA}^{-1}$ . The red dashed lines illustrate  $\Theta^*$ , while the black "x" and solid lines indicate the ground truth values. Panel e shows the correlation between all  $\Theta$  parameters as a function of  $q$  range.

## XV. FITTING FOR THE $\mathcal{I}$ COEFFICIENT

Having a precise measurement of  $\mathcal{I}$  is very important in determining the molecular frame angles. Both the pair-wise angles and  $\mathcal{I}$  act as a weighting function to the  $q$  dependent Spherical Bessel functions, shown in Eq. 14. If  $\mathcal{I}$  is not correct, this may lead to a systematic offset of the molecular frame angles as the error in  $\mathcal{I}$  must be absorbed by  $Y_l^{-m_1}(\theta_{\mu\nu}^{(\text{mf})}, \phi_{\mu\nu}^{(\text{mf})})$ . When fitting for  $\mathcal{I}$  one will generally need to know the molecular geometry, often this will be the ground state geometry. Below we describe a few methods to retrieve  $\mathcal{I}$  or circumvent this issue.

Our first method cancels out the factor of  $\mathcal{I}$  by using the ratio of  $C_{lmk}(q)/C_{l'mk}(q)$  for the MHA. This requires one measure multiple anisotropy components. One can also let  $l' = 0$  since the isotropic component is independent of the molecular frame angles and will therefore not introduce any bias. In this method, one does not need to use a simulated geometry to fit for  $\mathcal{I}$ .

The second method involves having multiple datasets, or partitioning the full dataset to fit  $\mathcal{I}$ . The first possible partition is in time, where one uses the  $C_{lmk}(q)$  from a certain point in the alignment. One may find it easiest to look at times before the induced rotation since one must already know the ground state to simulate the ADMs. The second possible partition is to use the  $l = 0$  signal and known  $\Delta\mathbf{r}_{\mu\nu}$  to fit for  $\mathcal{I}$ . One may also collect a second pump-off dataset to fit for  $\mathcal{I}$  or randomly partition a single dataset. Such a secondary dataset can also be used to fit the ADMs if one also induces vibrational dynamics as well.

The last method addresses the case of having few  $C_{lmk}(q)$  anisotropy contributions and a small dataset. This is the case for the  $\text{N}_2\text{O}$  results presented here. One may implement a bootstrapping method that relies on fitting Eq. 14 to a  $C_{lmk}(q)$  for varying  $q$  ranges. One can retrieve the best fit value for  $\mathcal{I}$  and its corresponding error from the resulting distribution of fits.